

The Hawaii Infrared Parallax Program. VI. The Fundamental Properties of 1000+ Ultracool Dwarfs and Planetary-mass Objects Using Optical to Mid-IR SEDs and Comparison to BT-SETTL and ATMO 2020 Model Atmospheres

ANIKET SANGHI ,^{1, 2,*} MICHAEL C. LIU ,² WILLIAM M. BEST ,³ TRENT J. DUPUY ,⁴ ROBERT J. SIVERD ,²
 ZHOUJIAN ZHANG ,⁵ SPENCER A. HURT ,⁶ EUGENE A. MAGNIER ,² KIMBERLY M. ALLER ,² AND NIALL R. DEACON ,⁷

¹Department of Astronomy, California Institute of Technology, 1200 E. California Boulevard, Pasadena, CA 91125, USA

²Institute for Astronomy, University of Hawaii, 2680 Woodlawn Drive, Honolulu, HI 96822, USA

³The University of Texas at Austin, Department of Astronomy, 2515 Speedway, C1400, Austin, TX 78712, USA

⁴Institute for Astronomy, University of Edinburgh, Royal Observatory, Blackford Hill, Edinburgh, EH9 3HJ, UK

⁵University of California, Santa Cruz, 1156 High St. Santa Cruz, CA 95064, USA

⁶Department of Physics and Astronomy, University of Wyoming, Laramie, WY 82071, USA

⁷Max Planck Institute for Astronomy, Konigstuhl 17, D-69117 Heidelberg, Germany

ABSTRACT

We derive the bolometric luminosities (L_{bol}) of 865 field-age and 189 young ultracool dwarfs (spectral types M6–T9, including 40 new discoveries presented here) by directly integrating flux-calibrated optical to mid-IR spectral energy distributions (SEDs). The SEDs consist of low-resolution ($R \sim 150$) near-IR (0.8–2.5 μm) spectra (including new spectra for 97 objects), optical photometry from the Pan-STARRS1 survey, and mid-IR photometry from the CatWISE2020 survey and Spitzer/IRAC. Our L_{bol} calculations benefit from recent advances in parallaxes from *Gaia*, Spitzer, and UKIRT, as well as new parallaxes for 19 objects from CFHT and Pan-STARRS1 presented here. Coupling our L_{bol} measurements with a new uniform age analysis for all objects, we estimate substellar masses, radii, surface gravities, and effective temperatures (T_{eff}) using evolutionary models. We construct empirical relationships for L_{bol} and T_{eff} as functions of spectral type and absolute magnitude, determine bolometric corrections in optical and infrared bandpasses, and study the correlation between evolutionary model-derived surface gravities and near-IR gravity classes. Our sample enables a detailed characterization of BT-SETTL and ATMO 2020 atmospheric model systematics as a function of spectral type and position in the near-IR color-magnitude diagram. We find the greatest discrepancies between atmospheric and evolutionary model-derived T_{eff} (up to 800 K) and radii (up to 2.0 R_{Jup}) at the M/L transition boundary. With 1054 objects, this work constitutes the largest sample to date of ultracool dwarfs with determinations of their fundamental parameters.

Keywords: Fundamental parameters of stars (555); Astrometry (80); Photometry (1234); Brown dwarfs (185); M dwarf stars (982); L dwarfs (894); T dwarfs (1679); Spectral energy distribution (2129); Bolometric correction (173); Stellar evolutionary models (2046); Stellar atmospheres (1584); Exoplanet atmospheres (487)

1. INTRODUCTION

Brown dwarfs are substellar objects more massive than gas-giant planets ($\gtrsim 13 M_{\text{Jup}}$; Spiegel et al. 2011) but less massive than stars ($\lesssim 70 M_{\text{Jup}}$; Dupuy & Liu 2017). All brown dwarfs fuse deuterium (e.g. Saumon et al. 1996) and those between 60–75 M_{Jup} will also burn lithium (Basri 1998). Brown dwarfs cool through their lifetimes, progress-

ing through a wide temperature range spanning the M, L, T and Y spectral types (e.g. Burrows et al. 1997; Kirkpatrick 2005; Cushing et al. 2011). This continuous cooling means that for a given luminosity and effective temperature, and hence spectral type, the age and mass of a brown dwarf are not uniquely determined. Such an observational degeneracy makes it challenging to use colors, magnitudes, and spectral types to determine the physical properties of brown dwarfs, such as mass, age, and radius. However, the luminosities and temperatures for a population of brown dwarfs do characterize their evolutionary history and provide unique information about the star-formation history of our Galaxy (Best

Corresponding author: Aniket Sanghi
 asanghi@caltech.edu

* NSF Graduate Research Fellow.

et al. 2021; Kirkpatrick et al. 2021). Additionally, young brown dwarfs, identified by their unusually red near- to mid-infrared colors as well as lower surface gravities, serve as crucial templates for understanding the atmospheric properties (e.g., clouds) of giant exoplanets given their similar effective temperatures and ages (e.g. Liu et al. 2013; Faherty et al. 2016; Liu et al. 2016). A large, well-defined sample of brown dwarfs with accurate and precise luminosity measurements would enhance our ability to test models of substellar formation, evolution, and atmospheres.

A proven approach to determining the physical properties of ultracool dwarfs ($\gtrsim M6$) is to assemble and integrate broadband spectral energy distributions (SEDs) consisting of flux-calibrated optical, near-infrared, and mid-infrared spectra and/or photometry to obtain bolometric fluxes (e.g. Filippazzo et al. 2015). Given parallax measurements, we can then derive the corresponding bolometric luminosities (L_{bol}). The bolometric luminosities can be used together with age estimates and evolutionary models to compute the masses and radii of ultracool dwarfs. Finally, combining the bolometric luminosities with evolutionary model-derived radii and applying the Stefan-Boltzmann Law enables the calculation of effective temperatures.

This approach should yield less model-dependent results than deriving the bolometric luminosities, effective temperatures, and surface gravities simultaneously from atmospheric model spectra fits, and then obtaining the masses and radii. Bolometric luminosities derived by atmospheric model fits can introduce systematic uncertainties since such measurements are dependent upon the fidelity of the fitting procedures adopted, the sampling of the model grid, and the differing input physics between various atmospheric models (e.g. Stephens et al. 2009; Zhang et al. 2021b). Filippazzo et al. (2015) adopted the SED integration strategy, combining optical, near-infrared, and mid-infrared spectra and photometry to construct spectral energy distributions for 145 field-age and 53 young ultracool dwarfs and thereby derive their fundamental physical properties. The uncertainties in the distances were the largest contributor to the uncertainty in their bolometric luminosities. Thus, high-precision parallax measurements are a necessity for accurate and precise determinations of bolometric luminosities. Similarly, since the uncertainty in age is the dominant contributor to the uncertainty in ultracool dwarf masses, radii, surface gravities, and effective temperatures, well-constrained ages are a necessity for accurate and precise determinations of these physical properties. The limited availability of such measurements has constrained the sample size of objects in previous work.

The first generation of ultracool dwarf parallax programs focused on obtaining measurements for small samples of objects across the spectral type range M, L, and T as they were newly discovered (Dahn et al. 2002; Tinney et al. 2003; Vrba

et al. 2004). With the rapid acceleration in the number of ultracool dwarf discoveries catalyzed by the advent of large digital sky surveys, the latest generation of ultracool parallax programs have focused their efforts on distinct classes of objects and large volume-limited samples. The Hawaii Infrared Parallax Program has observed L/T transition dwarfs (Dupuy & Liu 2012), young ultracool dwarfs (Liu et al. 2016), and ultracool binaries (Dupuy & Liu 2012, 2017) with WIRCam on the Canada–France–Hawaii Telescope (CFHT), and most recently obtained infrared parallax measurements for 348 L and T dwarfs with WFCAM on the United Kingdom Infrared Telescope (Best et al. 2020). Several programs have targeted late-T and Y dwarfs, the coldest objects in the ultracool dwarf temperature sequence (Dupuy & Kraus 2013; Beichman et al. 2014; Tinney et al. 2014; Martin et al. 2018; Kirkpatrick et al. 2019, 2021). Therefore, a large-scale analysis aimed at deriving ultracool dwarf properties by taking advantage of the tremendous advances in precision and availability of trigonometric parallax measurements, particularly for later-type objects, is timely.

Age dating stars and brown dwarfs is a notoriously difficult task, but steady progress has been made over the past decade. The simultaneous study of a large ensemble of stars has proven to be a successful avenue to obtaining new age measurements. The discovery of coeval, kinematically co-moving associations of young stars and brown dwarfs in the solar neighborhood called young moving groups (YMGs) has been instrumental to the effort (e.g. Zuckerman & Song 2004; Gagné et al. 2014c; Aller et al. 2016; Faherty et al. 2016; Liu et al. 2016; Gagné et al. 2018, 2022). Group members generally span a wide range of masses and, thus, can be used to age date each group using lithium depletion boundaries and isochrone fitting (e.g. Bell et al. 2015; Herczeg & Hillenbrand 2015). For the field population of ultracool dwarfs, Dupuy & Liu (2017) empirically determined an age distribution consistent with the Besançon model of the solar neighborhood (Robin et al. 2003) based on cooling ages of 20 ultracool dwarfs in binaries derived from high-precision dynamical mass measurements. In addition, various techniques have been developed geared towards identifying signs of youth in individual objects. Activity-based indicators such as chromospheric H α emission (West et al. 2008; Kiman et al. 2021), coronal X-ray emission (Jackson et al. 2012; Booth et al. 2017), and UV emission (Shkolnik et al. 2011; Rodriguez et al. 2013) are found to be well-correlated with stellar ages. Tracing lithium absorption features in ultracool dwarf spectra and performing a comparison with predictions of lithium-burning timescales from evolutionary models can provide valuable insights into the age of young dwarfs (Kirkpatrick et al. 2008; Binks & Jeffries 2016; Zhang et al. 2022). For mid-M to L dwarfs, there are a number of gravity-sensitive features in the near-infrared such as

Table 1. Comprehensive Reference List for Table of Ultracool Fundamental Properties Data

References
Leggett et al. (1998); Best et al. (2020); Aller et al. (2016); Cribo et al. (2005); Lodieu et al. (2005); Lodieu (2013); Scholz et al. (2001); Dahn et al. (2002); Thackrah et al. (1997); Skrutskie et al. (2006); Liu et al. (2013); EROS Collaboration et al. (1999); Patten et al. (2006); Goldman et al. (2010); Gizis et al. (2013); Mace et al. (2013); Kirkpatrick et al. (2006); Scholz & Meusinger (2002); Goliowski et al. (2004); Birmingham et al. (2013); Scholz et al. (2004); Smart et al. (2018); Wilson et al. (2003); Reid & Walkowicz (2006); Forveille et al. (2004); Seifahrt et al. (2005); Best et al. (2017); Gagné et al. (2014b); Irwin et al. (1991); Liebert et al. (1979); Gizis et al. (2012); Ellis et al. (2005); Reylé et al. (2006); Leggett et al. (2009); Edge et al. (2016); Griffith et al. (2012); Best et al. (2015); Deacon & Hamby (2007); Delfosse et al. (1997); Marocco et al. (2013); Albert et al. (2011); Deacon et al. (2011); Tinney (1993a); Martín et al. (2010); Henry et al. (2004); Gizis et al. (2011a); Shkolnik et al. (2017); Gizis et al. (2011b); Burgasser (2007a); Aller (2016); Schmidt et al. (2015); Becklin & Zuckerman (1988); Luhman et al. (2012); Pinfield et al. (2012); Mugrauer et al. (2006); West et al. (2008); Kirkpatrick et al. (1995); Kirkpatrick et al. (1991); Strauss et al. (1999); Folkes et al. (2012); Scholz et al. (2000); Schneider et al. (2002); Teegarden et al. (2003); Liebert & Burgasser (2007); Best et al. (2013); Luhman (2006); Burgasser et al. (2007); Schneider et al. (2016b); Burgasser (2004); Metchev et al. (2015); Burgasser et al. (2003b); Boeshaar (1976); Tinney (1996); Koen et al. (2017); Luhman et al. (2007); Faherty et al. (2016); Gagné et al. (2014a); Fan et al. (2000); Delfosse et al. (1999); Schmidt et al. (2010); Gagné et al. (2022); Kirkpatrick et al. (2019); Burgasser & McElwain (2006); Bardalez Gagliuffi et al. (2014); Deacon et al. (2017); Burgasser et al. (2008c); Kellogg et al. (2017); Burgasser et al. (2000a); Lodieu et al. (2002); van Leeuwen (2007); Deacon et al. (2012a); Castro & Gizis (2012); Kirkpatrick et al. (2011); Leggett et al. (2002); Cruz et al. (2009); Phan-Bao et al. (2001); Gillon et al. (2016); Lodieu et al. (2014); Kendall et al. (2007); Looper et al. (2007b); Cruz et al. (2003); Best et al. (2018); Faherty et al. (2012); Chambers et al. (2016); Liu et al. (2016); Chiu et al. (2006); Gagné et al. (2015); Bowler et al. (2013); Deacon et al. (2012b); Bowler et al. (2012); Zhang et al. (2009); Liebert et al. (2003); Pineda et al. (2016); Bardalez Gagliuffi et al. (2019); Zhang et al. (2021c); Phan-Bao et al. (2008); Biham et al. (2013); Ruiz et al. (1991); Leggett (1992); Looper et al. (2008); Bouvier et al. (2008); Giampapa & Liebert (1986); Hawkins & Bessell (1988); Henry & Kirkpatrick (1990); Burgasser (2007b); Lucas et al. (2010); Gagné et al. (2017); Miles-Páez et al. (2017); McMahon et al. (2013); Baron et al. (2015); Reid et al. (2008); Knapp et al. (2004); Zhang et al. (2021a); Schneider et al. (2023); Luhman & Sheppard (2014); Leggett et al. (2010); Burgasser et al. (2008a); Muvžić et al. (2012); Castro et al. (2013); Geballe et al. (2002); Burgasser et al. (2004); Dobbie et al. (2002); Best et al. (2021); Deacon et al. (2005); Tinney (1993b); Burgasser et al. (2003a); Leggett et al. (2012); Kirkpatrick et al. (2001); Folkes et al. (2007); Cushing et al. (2011); van Biesbroeck (1961); Schilbach et al. (2009); Metchev et al. (2008); Dahn et al. (2017); Kirkpatrick et al. (2000); Cushing et al. (2004); Basri et al. (2000); Cutri et al. (2003); UKIDSS Consortium (2012); Burgasser et al. (2008b); Bowler et al. (2015); Allers & Liu (2013); Reid & Gilmore (1981); Kirkpatrick et al. (1999); Lépine et al. (2009); Cardoso et al. (2015); Tinney et al. (2003); Scholz et al. (2009); Reid et al. (2006a); Leggett et al. (2000); Martin et al. (1994); Gilmore et al. (1985); Gizis et al. (2015a); Henry et al. (2006); Cruz et al. (2007); Manjavacas et al. (2013); Burgasser et al. (2016); Schneider et al. (2017); Burgasser et al. (2006a); Wilson et al. (2001); Gizis (2002); Hawley et al. (2002); Gizis & Reid (1997); Tinney et al. (1993); Kendall et al. (2003); Kendall et al. (2004); Marocco et al. (2010); Rice et al. (2010); Kellogg et al. (2015); Dupuy & Liu (2012); Giclas et al. (1971); Lawrence et al. (2007); Leggett et al. (2006); Gauza et al. (2019); Burgasser et al. (2000b); Reid & Gizis (2005); Metodieva et al. (2015); Vrba et al. (2004); Kirkpatrick et al. (2014); Rebolo et al. (1998); Cushing et al. (2014); Gomes et al. (2013); Reid et al. (2006b); Zapatero Osorio et al. (2010); Schneider et al. (1991); Gaia Collaboration et al. (2023); Gagné & Faherty (2018); Kirkpatrick et al. (1997b); Weinberger et al. (2016); Siegler et al. (2007); Burgasser et al. (2006b); Schneider et al. (2014); Reid et al. (1995); Kirkpatrick et al. (2008); Dupuy & Kraus (2013); Deacon et al. (2014); Marocco et al. (2015); Valenti & Fischer (2005); Kirkpatrick et al. (1997a); Dupuy et al. (2018); Lépine & Shara (2005); Luhman et al. (2009); Radigan et al. (2008); Faherty et al. (2009); Schneider et al. (2016a); Lodieu et al. (2012); Kirkpatrick et al. (2010); Scholz (2010); Metchev & Hillenbrand (2006); Skrzypek et al. (2016); Dye et al. (2018); Gizis et al. (2015b); McElwain & Burgasser (2006); Smith et al. (2014); Allers et al. (2010); Burgasser et al. (2010a); Birmingham et al. (2010); Sheppard & Cushing (2009); Reid et al. (2000); Geissler et al. (2011); Robert et al. (2016); Bouy et al. (2003); Reylé (2018); Scholz et al. (2005); Scholz et al. (2011); Luhman (2014); Smart et al. (2013); Peña Ramírez et al. (2015); Tinney et al. (2005); Cutri et al. (2021); Kirkpatrick et al. (2016); Burgasser et al. (2010b); Phan-Bao et al. (2006); Salim et al. (2003); Leggett et al. (2007); Lawrence et al. (2012); Burgasser & Splat Development Team (2017); Looper et al. (2007a); Faherty et al. (2013); McMahon et al. (2021); Gizis et al. (2000); Liebert & Gizis (2006); Birmingham et al. (2011); Zhang et al. (2021b); Tinney et al. (2018); Gizis et al. (2001); Kirkpatrick et al. (2012); Gizis et al. (2003); Burgasser et al. (2003c); Tinney et al. (1998); Martin et al. (1999); Hsu et al. (2021); Burgasser et al. (1999); Thompson et al. (2013); Kirkpatrick et al. (2021); Probst & Liebert (1983); Artigau et al. (2006); Reid et al. (2004); Kirkpatrick et al. (1994); Bessell (1991); Reylé & Robin (2004); Marocco et al. (2021); Liu et al. (2011); Tsvetanov et al. (2000); Faherty et al. (2010); Casagrande et al. (2011); Best et al. (AAS Journals, submitted); Hurt et al. (AAS Journals, submitted); <i>The UltracoolSheet</i> (version 2.0.0, in preparation); This Work.

NOTE—References for ultracool dwarf discoveries, spectral types (optical/IR), gravity classifications (optical/IR), parallaxes, SpeX prism spectra, ages, Pan-STARRS 1 *grizy* photometry, 2MASS *JHK_S* photometry, MKO *JHK* photometry, WISE *W1*, *W2*, *W3*, and *W4* photometry, and Spitzer Channel 1 and Channel 2 photometry presented in the Table of Ultracool Fundamental Properties associated with this work (see §1) are included above.

FeH (0.99, 1.20, 1.55 μm), VO (1.06 μm), Na I (1.138 μm), K I (1.169, 1.177, 1.244, 1.253 μm), and the shape of the *H*-band continuum (1.46–1.68 μm) that can be used to uncover low gravity (young) objects (Allers & Liu 2013; Cruz et al. 2018). Similarly, at optical wavelengths, weak Na I (8183, 8195 Å), Cs I (8521, 8943 Å), Rb I doublet lines (7800, 7948 Å), weak pressure-broadened K I wings (7665, 7699 Å), weak FeH (8692 Å), and strong VO (7300–7550 Å and 7850–8000 Å) in early type dwarfs act as spectroscopic signatures of low-gravity (youth) (Martín et al. 1998; Cruz et al. 2009; Kirkpatrick et al. 2010).

The large-scale effort to leverage advances in parallax and age measurements to empirically determine the fundamental properties of ultracool dwarfs has been greatly facilitated by the development of *The UltracoolSheet* (version 2.0.0, in preparation). *The UltracoolSheet* is a catalog of 3000+ ultracool dwarfs and directly imaged exoplanets, including optical to mid-infrared photometry from Pan-STARRS1 (Chambers et al. 2016), 2MASS (Skrutskie et al. 2006), UKIDSS/UHS (Lawrence et al. 2007; Dye et al.

2018), and CatWISE (Eisenhardt et al. 2020; Marocco et al. 2021), absolute astrometry, proper motions, parallaxes, multiplicity (including orbit determinations), and spectroscopic classifications. A major benefit offered by *The UltracoolSheet* for deriving bolometric luminosities is that it not only compiles high-precision parallax values from the latest surveys (e.g., *Gaia DR3*) and literature measurements (e.g. Best et al. 2020; Kirkpatrick et al. 2021), but also compares the various sources to readily make available the most precise measurement available to-date for each listed object. Additionally, it provides photometric distance estimates for objects without parallax measurements. In short, *The UltracoolSheet* is a valuable resource well matched to the goals of this work.

In this paper, we derive the fundamental physical properties of 1054 ultracool dwarfs by directly integrating flux-calibrated SEDs consisting of low-resolution near-infrared SpeX prism spectra and optical and mid-infrared photometry. This work increases the sample of ultracool dwarfs with semi-empirical physical parameter measurements by nearly

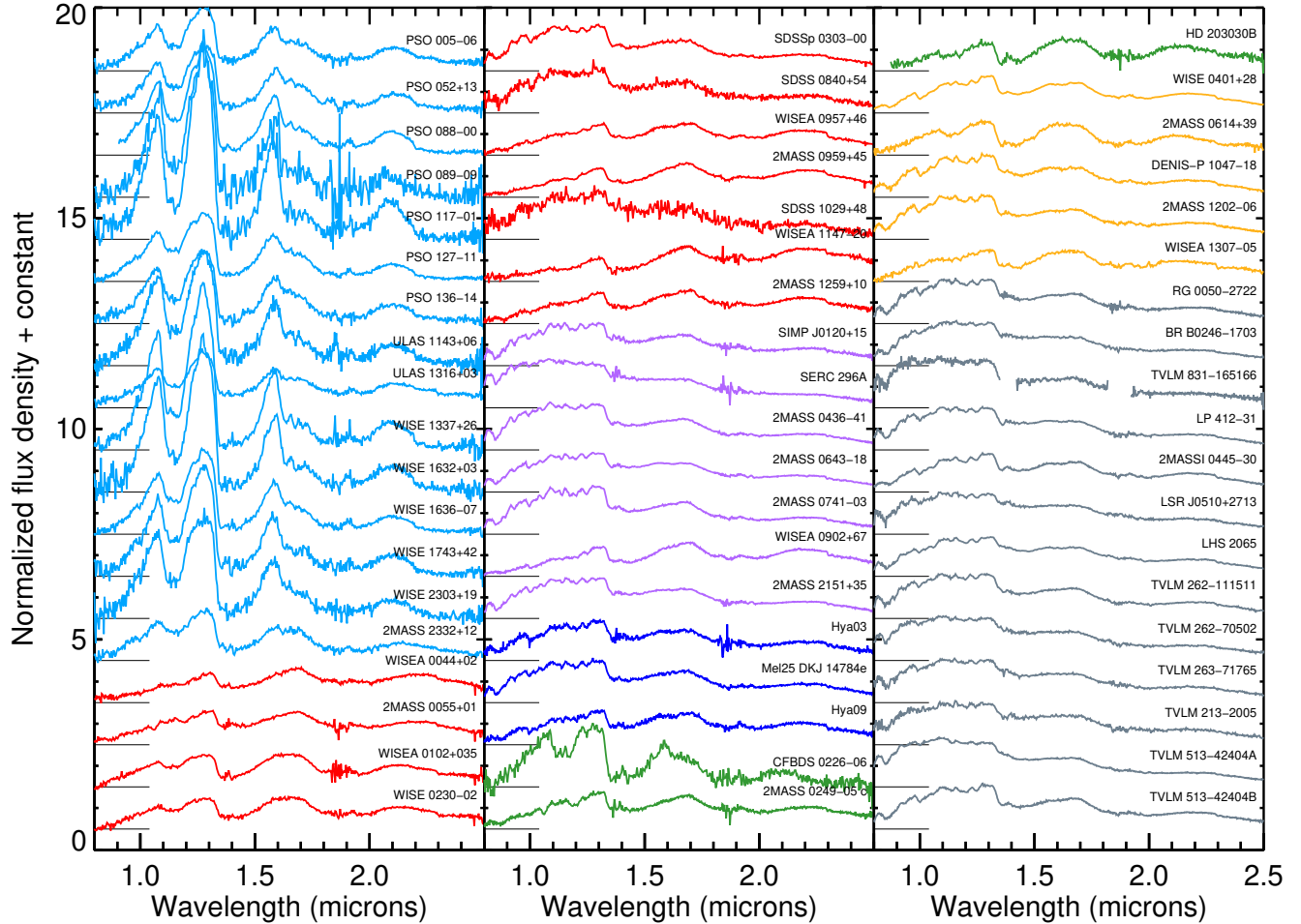


Figure 1. Near-infrared (0.8–2.5 μm) SpeX prism spectra for the 57 known objects presented in Table 2. From top to bottom and left to right, plotting order follows the table order for objects, namely by category (which is colorized in the plot) and then by right ascension. Light blue corresponds to T dwarfs, red corresponds to red L dwarfs, purple corresponds to candidate low-gravity objects, dark blue corresponds to Hyades members, green corresponds to wide substellar/planetary-mass companions, yellow corresponds to solar neighborhood candidates, and gray corresponds to M/L transition dwarfs. The horizontal line to the left of each spectrum shows the zero flux level.

five-fold, and takes advantage of significant growth in parallax data for ultracool dwarfs. Additionally, we construct and analyze empirical relationships for bolometric luminosity and effective temperature as functions of spectral type and absolute magnitude, determine bolometric corrections across the optical to mid-infrared filters, benchmark the near-infrared gravity classifications against evolutionary model-derived surface gravity measurements, and study systematic offsets between fundamental parameters derived with evolutionary (BHAC15 and SM08) and atmospheric (BT-SETTL and ATMO 2020) models. We prepare a Table of Ultracool Fundamental Properties¹ that is a subset of *The UltracoolSheet* (version 2.0.0, in preparation) tied uniquely to this work. It is a comprehensive compilation of the astrometric, photometric, spectroscopic, and age properties of all objects

in our sample. Importantly, it contains the fundamental parameters calculated in this work for all objects in our sample. References for all data used in this work, compiled in the Table of Ultracool Fundamental Properties, are included in Table 1.

This paper is organized as follows. Section 2 details the construction of our ultracool dwarf sample and presents newly discovered objects, new object spectra, and new parallax measurements. Section 3 describes the spectra and photometry used to assemble and flux-calibrate multiwavelength ultracool dwarf spectral energy distributions (SEDs). Section 4 details our procedures to estimate flux in regions where no spectra are available using atmospheric model fitting. Sections 5 and 6 discuss the calculation of bolometric luminosities and assignment of ages for the 1054 ultracool dwarfs in our sample. Section 7 summarizes the techniques used to derive the masses, radii, surface gravities, and effective temperatures for objects in our ultracool dwarf sample. Section

¹ Zenodo Data Publication: <https://doi.org/10.5281/zenodo.8315643>

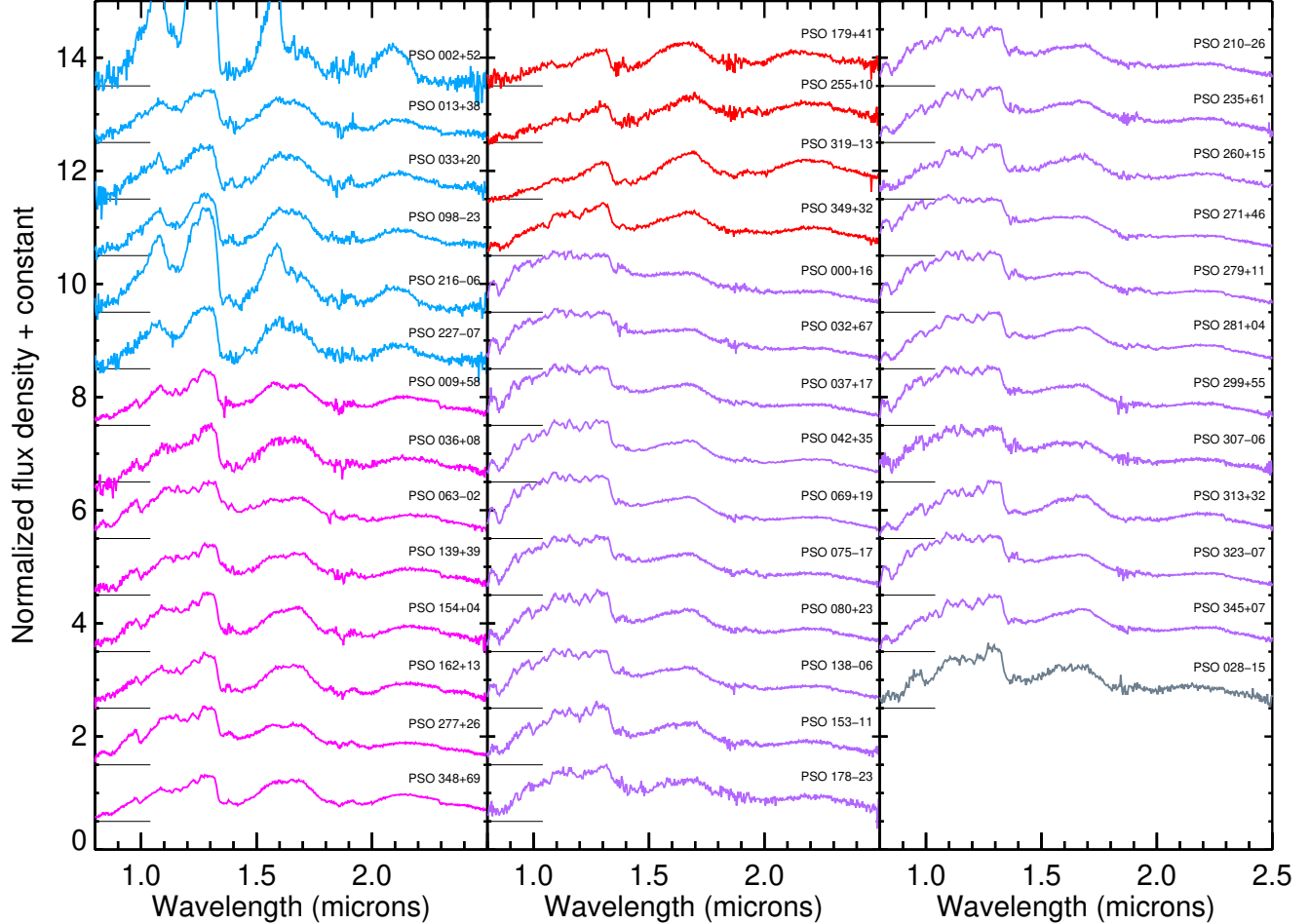


Figure 2. Near-infrared ($0.8\text{--}2.5 \mu\text{m}$) SpeX prism spectra for the 40 new discoveries presented in Table 3. From top to bottom and left to right, plotting order follows the table order for objects, namely by category (which is colorized in the plot) and then by right ascension. Light blue corresponds to T dwarfs, magenta corresponds to L dwarfs, red corresponds to red L dwarfs, purple corresponds to low-gravity objects, and gray corresponds to M/L transitions dwarfs. The horizontal line to the left of each spectrum shows the zero flux level.

8 presents calculations of bolometric corrections, analysis of the relationship between gravity classes and derived surface gravities, and a detailed look at atmospheric model-derived parameters in comparison with evolutionary model-derived parameters. Finally, Section 9 presents our conclusions. Appendix A presents revised absolute magnitude-spectral type relations for young ultracool dwarfs based on all available objects in *The UltracoolSheet*.

2. SAMPLE & ADDITIONAL OBSERVATIONS

2.1. Construction of Ultracool Dwarf Sample

Our sample is constructed using *The UltracoolSheet* (version 2.0.0, in preparation), selecting all objects with parallaxes or photometric distances and SpeX prism spectra readily available to us. We exclude unresolved binaries and multiples, subdwarfs, and members of active star-forming regions (e.g. Taurus, Chamaeleon, Lupus, IC348, etc.). *The UltracoolSheet* columns relevant to the above criteria are `multiple_unresolved_in_this_table`, `flag`, and

`age_category`, respectively. In total, 1054 objects in *The UltracoolSheet* satisfy the above criteria (including the newly discovered ultracool dwarfs discussed below).

2.2. New Objects and Spectra

We obtained low-resolution near-IR ($0.8\text{--}2.5 \mu\text{m}$) spectroscopy for 97 objects in our sample using the NASA Infrared Telescope Facility (IRTF) on the summit of Mauna Kea, Hawaii. We used the facility spectrograph SpeX (Rayner et al. 2003) in prism mode with either the $0.5''$ or $0.8''$ slit, which provided an average spectral resolution ($R \equiv \Delta\lambda/\lambda$) of ≈ 150 or ≈ 100 , respectively. We dithered in an ABBA pattern on the science target to enable sky subtraction during the reduction process. For each epoch, we obtained calibration frames (arcs and flats) and observed an A0 V star contemporaneously for telluric calibration. All spectra were reduced using the Spextool software package (Vacca et al. 2003; Cushing et al. 2004).

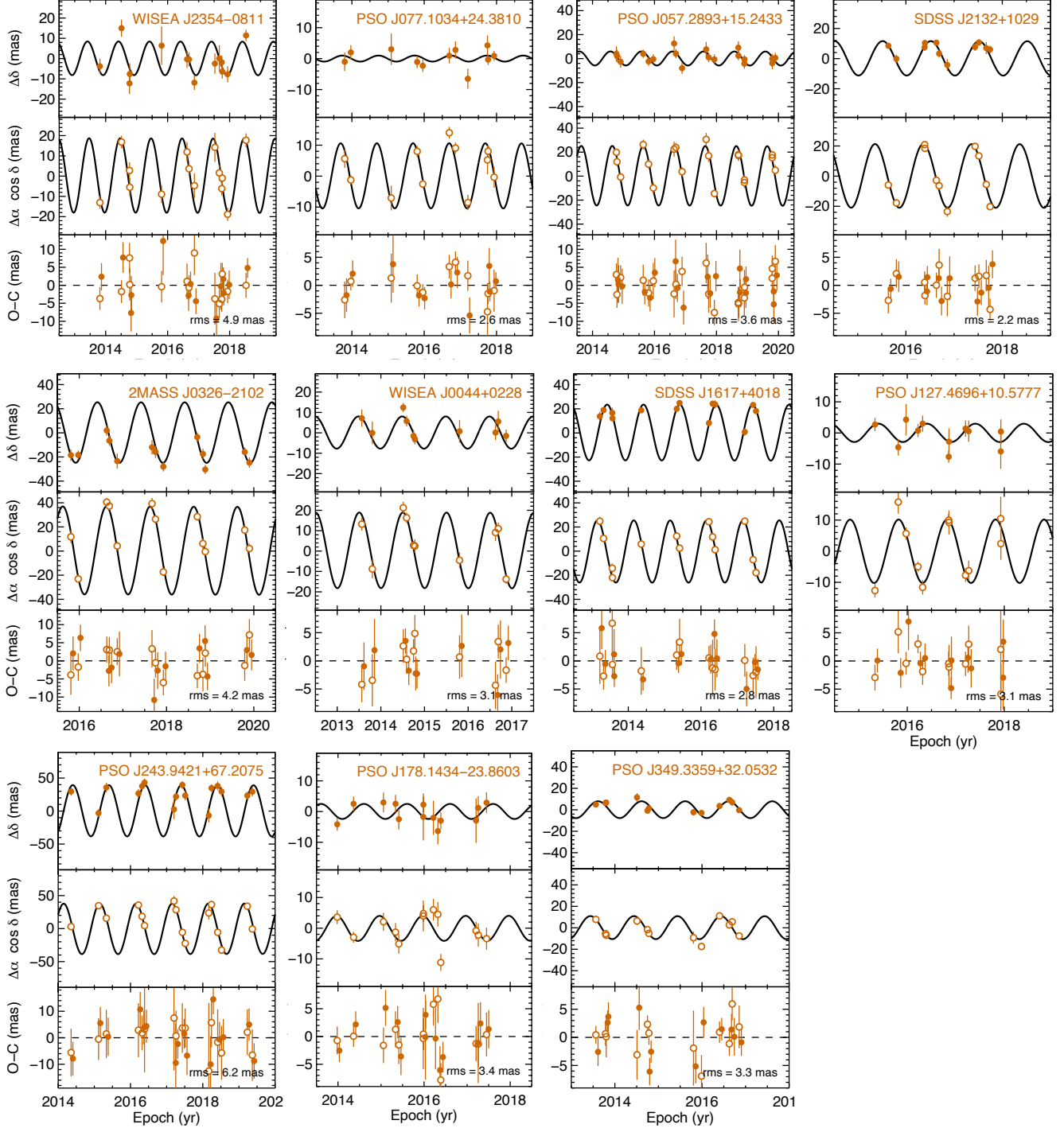


Figure 3. Parallax solutions for 11 objects with new CFHT/WIRCam astrometry. For each object, three panels are shown: Decl. measurements with the proper motion and zero point subtracted (top); R.A. measurements with the proper motion and zero point subtracted (middle); and the residuals of both R.A. (open symbols) and Decl. (solid symbols) plotted with the best-fit parallax and proper motion solution subtracted (bottom). The standard deviation of the residuals of both R.A. and Decl. combined is quoted as the rms in the bottom panel. The top and middle subpanels show the motion expected from the best-fit parallax (solid line). Objects have varying observational time baselines, which is reflected in the varying x-axis ranges.

These spectra were obtained for a variety of programs conducted by us over the past decade, either for (1) spectroscopic characterization of known objects (Figure 1 and Table 2) or (2) discovery of new ultracool dwarfs (Figure 1 and Table 3). For (1), we obtained spectra of known objects that had potential indications of low-gravity spectra from previous work (e.g. Allers & Liu 2013) or objects that could serve as benchmark objects by virtue of being members of known stellar associations (the Hyades and Pleiades) or being wide substellar/planetary-mass companions to stars (e.g. Metchev & Hillenbrand 2006; Dupuy et al. 2018). Finally, as a bad-weather program, we obtained spectra of objects with pre-Gaia parallaxes and with spectral types at the M/L transition. For (2), the discoveries result from various multi-catalog photometric searches relying on the Pan-STARRS 1 optical survey as a staring point, including searches for T dwarfs (e.g. Deacon et al. 2011; Liu et al. 2011), very red (low-gravity) L dwarfs (e.g. Liu et al. 2013), young moving group members (e.g. Aller et al. 2016; Aller 2016), L/T transition dwarfs and objects in the solar neighborhood (e.g. Best et al. 2015). For spectral typing and gravity classification, we use the near-IR classification system described by Allers & Liu (2013) and Aller et al. (2016) for late-M and L dwarfs. For T dwarfs, we follow the near-IR system described by Burgasser et al. (2006b). Among the new discoveries, we find that PSO J080.3940+23.0999 is a new candidate AB Doradus Moving Group member with an 82.5% BANYAN Σ probability (Gagné et al. 2018).

2.3. New Parallaxes

For eleven objects — WISEA J004403.39+022810.6, 2MASS J03264225-2102057, PSO J057.2893+15.2433, PSO J077.1034+24.3810, PSO J127.4696+10.5777, SDSS J161731.65+401859.7, SDSS J213240.36+102949.4, WISEA J235422.31-081129.7, PSO J178.1434-23.8603, PSO J349.3359+32.0532, and PSO J243.9421+67.2075 —

we present new parallax measurements (Figure 3). They are available in the Table of Ultracool Fundamental Properties associated with this paper (see §1). We monitored these objects with the facility infrared camera WIRCam (Puget et al. 2004) on the Canada-France-Hawaii Telescope (CFHT). In the J band, we measured their (x, y) positions and those of many reference stars. Using our custom pipeline (Dupuy & Liu 2012; Dupuy et al. 2015), we reduced these individual measurements into high-precision multi-epoch relative astrometry, with the absolute calibration provided by low-proper-motion 2MASS stars (Cutri et al. 2003). We derived the relative parallax and proper motion for the targets using our standard MCMC approach and then, in order to be consistent with our many previously published CFHT parallaxes, converted to an absolute reference frame using the Besançon galaxy model to simulate the distances of the reference stars (Robin et al. 2003).

We also present new Pan-STARRS 1 (PS1) parallaxes for eight objects in our sample: 2MASS J03001631+2130205, 2MASSW J0309088-194938, SDSSp J032817.38+003257.2, 2MASSW J0355419+225702, 2MASSW J0918382+213406, 2MASS J13120707+3937445, SDSS J151603.03+025928.9, and SDSS J154849.02+172235.4. They are available in the Table of Ultracool Fundamental Properties associated with this paper (see §1). These objects were observed by the PS1 telescope from 2009–2015 as part of the Pan-STARRS 3 π Steradian Survey (Chambers et al. 2016) in the $grizy$ filters. The 3 π Survey was well-suited to parallaxes as every survey region was observed at opposition as well as evening and morning twilight. Astrometric calibration and automated calculation of parallaxes and proper motions are described by Magnier et al. (2020). The resulting astrometry is tied to the Gaia DR1 inertial system, with a correction for the proper motion bias introduced by Galactic rotation and solar motion.

Table 2. IRTF/SpeX Observing Log: Objects from the Literature

Object	UT Date	Slit ('')	<Airmass>	T_{int} (s)	<S/N> ($Y, J, H, H_{\text{blue}}, K, K_{\text{blue}}$)
T dwarfs					
PSO J005.6302-06.8669	2012-01-20	0.8''	1.49	120.0	16, 37, 20, 20, 16, 24
PSO J052.2746+13.3754	2012-09-24	0.8''	1.24	420.0	18, 45, 23, 25, 9, 18
PSO J088.5709-00.1430	2012-09-24	0.8''	1.08	1440.0	34, 103, 33, 46, 11, 35
PSO J089.1751-09.4513	2011-04-20	0.5''	2.10	240.0	7, 18, 3, 5, 1, 3
PSO J117.0600-01.6779	2012-04-20	0.8''	1.16	240.0	15, 28, 6, 12, 2, 10
PSO J127.5648-11.1861	2012-04-20	0.8''	1.24	240.0	30, 66, 30, 34, 11, 27
PSO J136.5380-14.3267	2012-04-20	0.8''	1.35	240.0	17, 34, 15, 17, 6, 13
ULAS J114340.47+061358.9	2015-05-26	0.8''	1.27	1554.1	16, 27, 7, 10, 3, 7

Table 2 *continued*

Table 2 (continued)

Object	UT Date	Slit ('')	<Airmass>	T_{int} (s)	<S/N> ($Y, J, H, H_{\text{blue}}, K, K_{\text{blue}}$)
ULAS J131610.13+031205.5	2012-04-20	0.8''	1.05	240.0	23, 50, 31, 32, 30, 36
WISE J133750.46+263648.6	2012-01-19	0.8''	1.03	120.0	28, 68, 15, 23, 4, 14
WISE J163236.47+032927.3	2012-08-10	0.8''	1.29	60.0	19, 42, 10, 19, 3, 9
WISE J163645.56-074325.1	2012-04-20	0.8''	1.13	240.0	28, 62, 26, 31, 9, 21
WISE J174303.71+421150.0	2012-07-05	0.8''	1.62	240.0	15, 37, 10, 14, 4, 10
WISE J230356.79+191432.9	2012-01-22	0.8''	1.64	120.0	12, 26, 8, 11, 3, 8
2MASS J23322678+1234530	2012-02-01	0.8''	1.95	120.0	14, 31, 18, 16, 18, 20
<hr/>					
Red L Dwarfs					
WISEA J004403.39+022810.6	2012-10-14	0.8''	1.06	1320.0	11, 31, 34, 29, 46, 45
2MASS J00550564+0134365	2012-10-25	0.8''	1.06	840.0	25, 62, 48, 43, 61, 61
WISEA J012020.11+035541.4	2012-10-25	0.8''	1.04	840.0	27, 52, 46, 41, 44, 50
WISE J023038.90-022554.0	2012-10-28	0.8''	1.22	1080.0	15, 34, 31, 28, 34, 37
SDSSp J030321.24-000938.2	2012-11-08	0.8''	1.06	840.0	51, 85, 48, 43, 42, 43
SDSS J084016.42+543002.1	2012-04-30	0.8''	1.34	120.0	12, 20, 12, 11, 14, 14
WISEA J095729.41+462413.5	2012-11-08	0.8''	1.31	840.0	25, 61, 57, 51, 69, 69
2MASS J09593276+4523309	2012-04-20	0.8''	1.18	180.0	25, 68, 67, 58, 86, 87
SDSS J102947.68+483412.2	2012-04-30	0.8''	1.63	120.0	8, 14, 7, 7, 8, 7
WISEA J114724.10-204021.3	2014-01-17	0.8''	1.33	1080.0	9, 28, 37, 32, 46, 48
2MASS J12594167+1001380	2012-01-20	0.8''	1.02	120.0	13, 42, 43, 37, 51, 52
<hr/>					
Candidate Low-Gravity Objects					
SIMP J01205253+1518277	2015-09-25	0.5''	1.01	1075.9	49, 64, 49, 47, 43, 43
SERC 296A	2015-11-24	0.5''	1.94	1912.7	118, 133, 108, 104, 71, 80
2MASS J04362788-4114465	2016-02-03	0.5''	2.06	418.4	102, 117, 83, 76, 65, 71
2MASS J06431685-1843375	2015-01-20	0.5''	1.28	418.4	110, 158, 130, 153, 110, 117
2MASS J07410404-0359495	2016-03-25	0.5''	1.39	836.8	83, 113, 79, 71, 72, 73
WISEA J090258.99+670833.1	2016-02-05	0.5''	1.47	2271.3	24, 52, 62, 50, 75, 75
2MASS J21512797+3547206	2015-08-07	0.5''	1.07	266.9	101, 135, 118, 111, 99, 100
<hr/>					
Hyades Members					
Hya03	2014-11-17	0.8''	1.03	87.6	19, 35, 31, 33, 28, 27
Cl Melotte 25 DKJ 14784e	2016-03-21	0.5''	1.25	1554.1	41, 52, 33, 29, 44, 41
Hya09	2016-02-03	0.5''	1.41	1315.0	12, 25, 20, 17, 28, 28
<hr/>					
Wide Substellar/Planetary-Mass Companions					
CFBDS J022644.65-062522.0	2011-12-02	0.8''	1.13	120.0	9, 20, 8, 9, 3, 5
2MASS J0249-0557 c	2015-09-25	0.5''	1.11	1554.1	20, 35, 33, 28, 38, 37
HD 203030B	2012-07-07	0.5''	1.08	240.0	8, 19, 22, 20, 20, 23
<hr/>					
Solar Neighborhood Candidates					
WISE J040137.21+284951.7	2013-12-11	0.8''	1.04	420.0	117, 261, 242, 234, 189, 198
2MASS J06143818+3950357	2011-10-14	0.8''	1.11	120.0	22, 44, 39, 38, 32, 38
DENIS-P J104731.1-181558	2012-04-30	0.8''	1.38	15.0	49, 98, 65, 58, 62, 63
2MASS J12022564-0629026	2015-05-19	0.8''	1.12	133.4	67, 89, 68, 62, 58, 59
WISEA J130729.56-055815.4	2011-03-31	0.5''	1.18	120.0	23, 53, 48, 45, 45, 48
<hr/>					
M/L Transition Dwarfs					
RG 0050-2722	2014-11-17	0.8''	1.47	107.0	48, 76, 77, 75, 52, 53
BR B0246-1703	2014-01-19	0.8''	1.50	35.0	37, 79, 68, 68, 40, 43

Table 2 continued

Table 2 (continued)

Object	UT Date	Slit ('')	<Airmass>	T_{int} (s)	<S/N> ($Y, J, H, H_{\text{blue}}, K, K_{\text{blue}}$)
TVLM 831-165166	2014-10-15	0.8''	1.07	87.6	20, 26, 23, 24, 15, 16
LP 412-31	2013-11-06	0.8''	1.00	50.0	45, 104, 95, 94, 58, 61
2MASSI J0445538-304820	2016-02-03	0.8''	1.57	418.4	66, 103, 83, 75, 74, 76
LSR J0510+2713	2014-01-19	0.8''	1.42	11.0	24, 55, 52, 52, 28, 30
LHS 2065	2014-01-19	0.8''	1.11	21.0	50, 127, 124, 124, 77, 81
TVLM 262-111511	2014-01-18	0.8''	1.21	105.0	68, 125, 99, 97, 62, 65
TVLM 262-70502	2014-01-18	0.8''	1.22	70.0	46, 85, 71, 71, 42, 44
TVLM 263-71765	2014-01-18	0.8''	1.19	35.0	32, 70, 62, 62, 35, 37
TVLM 213-2005	2014-01-19	0.8''	1.20	35.0	17, 38, 32, 32, 18, 19
TVLM 513-42404A	2014-07-29	0.8''	1.02	836.8	128, 131, 108, 93, 101, 102
TVLM 513-42404B	2014-07-29	0.8''	1.03	1315.0	76, 100, 67, 55, 66, 69

NOTE—The last column gives the median S/N of the spectrum for the standard IR bandpasses and also for two wavelength regions free of methane absorption ($H_{\text{blue}} = 1.49\text{--}1.63 \mu\text{m}$ and $K_{\text{blue}} = 2.03\text{--}2.20 \mu\text{m}$), which are relevant for T-dwarf spectra.

Table 3. IRTF/SpeX Observing Log: New Discoveries

Object	UT Date	Slit ('')	<Airmass>	T_{int} (s)	<S/N> ($Y, J, H, H_{\text{blue}}, K, K_{\text{blue}}$)
T dwarfs					
PSO J002.0878+52.0687	2012-01-22	0.8''	1.52	120.0	12, 32, 9, 13, 3, 11
PSO J013.7740+38.2804	2011-10-14	0.8''	1.13	120.0	16, 36, 23, 23, 15, 21
PSO J033.2936+20.4493	2011-10-14	0.8''	1.11	120.0	11, 24, 20, 21, 16, 21
PSO J098.2822-23.2845	2011-10-14	0.8''	1.37	120.0	17, 36, 23, 23, 18, 21
PSO J216.4707-06.2849	2012-04-20	0.8''	1.12	240.0	18, 45, 18, 22, 6, 14
PSO J227.1576-07.9608	2012-04-20	0.8''	1.18	240.0	12, 23, 15, 15, 7, 12
L Dwarfs					
PSO J009.8334+58.5781	2015-11-28	0.5''	1.33	836.8	27, 56, 42, 39, 48, 53
PSO J036.9069+08.5025	2012-01-20	0.8''	1.16	120.0	9, 31, 23, 21, 19, 21
PSO J063.1519-02.8904	2012-01-22	0.8''	1.08	120.0	40, 79, 53, 47, 46, 49
PSO J139.5493+39.0380	2012-01-19	0.8''	1.08	120.0	20, 50, 40, 38, 34, 37
PSO J154.9622+04.8279	2012-01-19	0.8''	1.09	120.0	22, 52, 35, 33, 29, 32
PSO J162.0614+13.9756	2012-01-19	0.8''	1.01	120.0	27, 59, 46, 45, 36, 39
PSO J277.3873+26.0116	2015-07-15	0.8''	1.01	207.6	41, 69, 57, 54, 47, 49
PSO J348.5125+69.6598	2015-12-08	0.5''	1.55	1793.2	50, 87, 76, 69, 86, 92
Red L Dwarfs					
PSO J179.2489+41.5121	2014-01-17	0.8''	1.08	1080.0	10, 25, 28, 25, 29, 33
PSO J255.0913+10.3263	2013-09-23	0.8''	1.59	240.0	7, 20, 19, 16, 30, 31
PSO J319.7576-13.0982	2013-09-22	0.8''	1.38	240.0	11, 38, 40, 33, 52, 54
PSO J349.3359+32.0532	2012-10-14	0.8''	1.03	2280.0	25, 53, 38, 34, 41, 40
Low-Gravity Objects					
PSO J000.2794+16.6237	2015-11-03	0.5''	1.26	418.4	58, 60, 42, 41, 34, 34
PSO J032.2211+67.4179	2015-12-24	0.5''	1.48	2032.3	65, 75, 56, 51, 47, 49
PSO J037.4616+17.2761	2015-09-30	0.5''	1.05	537.9	35, 52, 53, 49, 43, 43
PSO J042.8405+35.3726	2013-09-23	0.5''	1.08	120.0	73, 132, 93, 86, 77, 77
PSO J069.4987+19.6346	2015-01-21	0.5''	1.29	629.2	83, 111, 93, 89, 77, 74
PSO J075.4182-17.8327	2015-11-02	0.5''	1.32	418.4	47, 58, 41, 38, 38, 38

Table 3 *continued*

Table 3 (*continued*)

Object	UT Date	Slit ('')	$\langle \text{Airmass} \rangle$	$T_{\text{int}} (\text{s})$	$\langle S/N \rangle (Y, J, H, H_{\text{blue}}, K, K_{\text{blue}})$
PSO J080.3940+23.0999	2015-10-14	0.5''	1.03	207.6	42, 61, 51, 47, 42, 42
PSO J138.1887-06.9862	2015-12-24	0.5''	1.17	418.4	55, 73, 58, 54, 52, 52
PSO J153.7969-11.3631	2015-05-20	0.5''	1.28	2510.4	28, 39, 26, 23, 23, 24
PSO J178.1434-23.8603	2013-04-04	0.8''	1.39	2400.0	22, 39, 22, 20, 22, 22
PSO J210.6211-26.9300	2016-05-29	0.5''	1.47	1554.1	44, 54, 40, 36, 37, 37
PSO J235.3149+61.5071	2015-07-06	0.5''	1.34	1434.5	43, 59, 47, 42, 40, 41
PSO J260.1789+15.3091	2013-04-19	0.5''	1.01	180.0	24, 50, 32, 28, 36, 34
PSO J271.8353+46.9326	2014-08-01	0.5''	1.17	836.8	72, 127, 89, 83, 68, 78
PSO J279.6187+11.6036	2015-09-25	0.5''	1.02	418.4	87, 111, 87, 78, 75, 79
PSO J281.4296+04.2296	2015-07-15	0.8''	1.07	207.6	77, 107, 88, 81, 75, 75
PSO J299.5032+55.0722	2015-09-25	0.5''	1.23	537.9	55, 73, 57, 52, 47, 50
PSO J307.7981-06.6854	2015-07-04	0.5''	1.14	1075.9	19, 29, 26, 24, 22, 22
PSO J313.1067+32.9117	2015-12-08	0.5''	1.44	2032.3	36, 57, 41, 34, 43, 44
PSO J323.4300-07.5353	2015-08-07	0.5''	1.17	266.9	91, 108, 88, 83, 71, 72
PSO J345.2949+07.7665	2015-07-04	0.5''	1.06	1315.0	43, 70, 68, 62, 53, 55
M Dwarfs					
PSO J028.0715-15.5717	2012-10-15	0.8''	1.28	2520.0	13, 30, 17, 16, 14, 14

NOTE—The last column gives the median S/N of the spectrum for the standard IR bandpasses and also for two wavelength regions free of methane absorption ($H_{\text{blue}} = 1.49\text{--}1.63 \mu\text{m}$ and $K_{\text{blue}} = 2.03\text{--}2.20 \mu\text{m}$).

3. ULTRACOOL DWARF SPECTRAL ENERGY DISTRIBUTIONS

The central goal of the following analysis is to construct and directly integrate the spectral energy distributions of ultracool dwarfs to obtain their bolometric fluxes. Combining this calculated quantity with a distance measurement yields the bolometric luminosity. This then enables the derivation of other fundamental parameters such as masses, radii, effective temperatures, and surface gravities using evolutionary models. In this section, we discuss the spectra used in this work and our spectral flux-calibration procedures.

3.1. SpeX Prism Spectra

Since most ultracool dwarfs have faint apparent magnitudes, SpeX is often used in its low-resolution ($R \sim 75\text{--}200$) prism mode to acquire $0.8\text{--}2.5 \mu\text{m}$ spectra using one of the three different slit sizes — $0''.3 \times 15''.0$, $0''.5 \times 15''.0$, and $0''.8 \times 15''.0$. This wavelength range is sensitive to several well-known absorption features in ultracool dwarf spectra, e.g., CH₄, H₂O, FeH, and VO. SpeX prism spectra are ideal for SED measurements as its broad wavelength coverage captures the NIR region in a single contiguous spectrum thereby minimizing systematic uncertainties associated with combining multiple spectra from differing spectral orders or instruments. Filippazzo et al. (2015) find that bolometric luminosities derived from spectral integration are relatively independent of the spectral resolution. Thus, the accuracy of our results will not be hindered by the use of low-resolution spectra.

The large majority of spectra in our study were obtained from the SpeX prism Library (Burgasser 2014). A comprehensive list of references for our object spectra is provided in the Table of Ultracool Fundamental Properties associated with this paper (see §1). Flux measurements made at the wavelength extremes of the spectra generally have low S/N and can be unreliable. To mitigate this, we apply cuts to the spectra on the blue end at $0.85 \mu\text{m}$ and on the red end at $2.45 \mu\text{m}$. The values are chosen to avoid exclusion of wavelengths included in the filter transmission profiles of the PS1 *y* band on the blue end and the UKIDSS *K*-band on the red end.

3.2. Absolute Flux Calibration of SpeX Prism Spectra

To derive the bolometric flux from SED integration, we need to first calibrate each object's SpeX spectrum to its observed photometry. We begin with the highest available signal-to-noise ratio (S/N) SpeX spectrum of each object ($f_{\lambda, \text{obs}}$) and the photometry with similar wavelength coverage (PS1 *y*, 2MASS *JHK_S*, MKO *JHK*, and UKIDSS *JHK*). Each photometric point is converted to a flux density measurement ($f_{\lambda, \text{phot}}$) using the corresponding filter's zero point flux density. For several objects, we find that photometric measurements for some filters have formal uncertainties below the instrumental noise floor (PS1: Magnier et al. 2020). To avoid underestimating the uncertainties associated with flux calibration of the spectra, we adopt a uniform noise floor of 0.01 mag for all photometric measurements.

Next, we synthesize photometry from the SpeX spectrum of the object for all the filters discussed previously. The filter transmission profile T_{λ} is retrieved from the SVO Filter

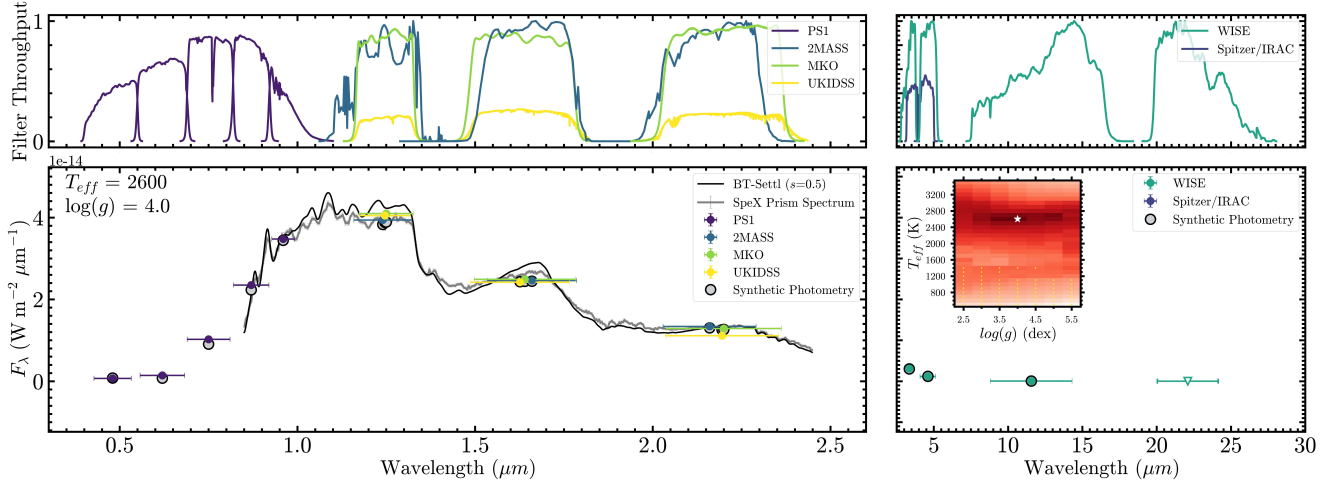


Figure 4. Example flux-calibrated SpeX prism spectrum generated in this work. *Top:* Filter transmission profiles for the PS1, 2MASS, MKO, UKIDSS, WISE, and Spitzer/IRAC filters. *Bottom:* Flux-calibrated SpeX spectrum (slit size = 0.5'') of 2MASSI J0335020+234235 in gray with the corresponding photometry in the same colors as the filter transmission profiles, if available. Photometry marked with triangles represent upper limits. The gray points represent model synthesized photometry. The black curve corresponds to the best-fit atmospheric model. The inset figure shows the χ^2 surface for the atmospheric model fits to the SpeX spectrum in T_{eff} - $\log g$ space. The white star marks the location of the model-fit with the smallest χ^2 . Yellow plus signs mark the T_{eff} - $\log g$ values at which ATMO 2020 model spectra were preferred over the BT-SETTL model spectra based on their lower χ^2 .

Profile Service² and the SpeX spectrum is interpolated using cubic spline interpolation and mapped to the wavelength grid of the transmission profile. We then calculate the synthetic photometry $f_{\lambda,\text{syn}}$ using,

$$f_{\lambda,\text{syn}} = \frac{\int f_{\lambda,\text{obs}} T_\lambda d\lambda}{\int T_\lambda d\lambda}, \quad (1)$$

where the limits of the integration are λ_{\min} and λ_{\max} of the wavelength grid of the filter transmission profile.

Combining the photometric flux densities and the synthetic flux densities derived previously, we can compute a scale factor k_i corresponding to each filter (i) as,

$$k_i = \left(\frac{f_{\lambda,\text{phot}}}{f_{\lambda,\text{syn}}} \right)_i, \quad (2)$$

$$\delta k_i = \left(\frac{\delta f_{\lambda,\text{phot}}}{f_{\lambda,\text{syn}}} \right)_i, \quad (3)$$

where δk_i is the associated uncertainty. We note here that since the synthetic flux density is an integration over the spectrum's many wavelength points corresponding to the filter transmission profile, its uncertainty can be neglected in comparison to the uncertainty in the photometric flux density. We derive the scale factor k for the calibration of the SpeX spectrum by obtaining the weighted average of the individual scale factors k_i . A 1% uncertainty floor is adopted for the weighted average scale factor k to avoid downweighting the photometric noise floor applied earlier. Finally, the calibrated spectrum $f_{\lambda,\text{cal}}$ (Figure 4) is found as $f_{\lambda,\text{cal}} = f_{\lambda,\text{obs}} \cdot k$.

4. ATMOSPHERIC MODEL FITTING

One of the challenges associated with deriving the bolometric luminosity by SED integration is the lack of optical and mid-infrared (MIR) spectra for most known ultracool dwarfs. However, optical and MIR photometry is well-measured for many of these objects by the Pan-STARRS1 and WISE surveys, respectively. In a few cases, individual objects also have MIR photometry from Spitzer/IRAC Channels 1 and 2 (Fazio et al. 2004). We fit the SpeX prism spectrum and the optical and/or MIR photometry with synthetic atmospheric grids produced by the BT-SETTL (CIFIST2011/2015; Allard et al. 2012; Baraffe et al. 2015) and ATMO 2020 (Phillips et al. 2020) models (Figure 5). Directly integrating the area under the best-fit atmospheric model spectrum in wavelength regions not covered by the SpeX prism spectrum then yields the associated optical and MIR contributions to the bolometric luminosity.

BT-SETTL (CIFIST2011/2015)³ incorporates the role of clouds and dust in its atmospheres, and thus resulting spectra, by self-consistently modeling their formation and sedimentation (Allard et al. 2012) and accounting for the condensation of nearly 200 liquid and solid species in the atmospheric equation of state. This makes BT-SETTL appropriate for late-M and L dwarfs, which have cloudy photospheres. Additionally, it includes linelists for several important molecules such as H₂O, CO₂, CaH, FeH, CrH, and TiH. Each model is calculated at solar metallicity ($Z = 0$ dex),

² <http://svo2.cab.inta-csic.es/theory/fps/index.php>

³ <http://svo2.cab.inta-csic.es/theory/newov2/index.php?models=bt-settl-cifist>

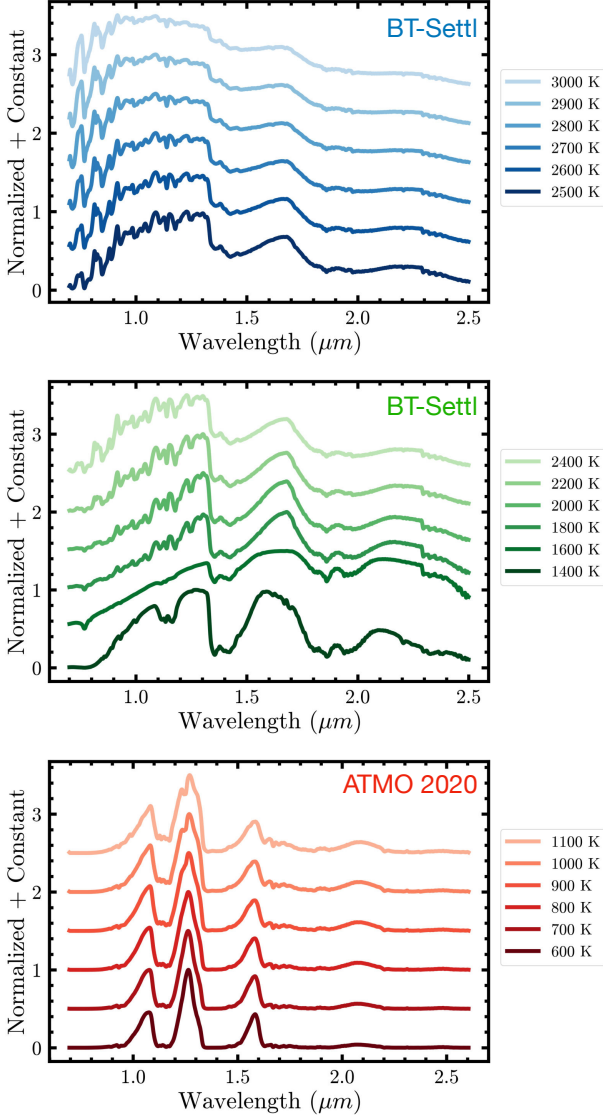


Figure 5. Normalized and vertically offset $\log g = 5.0$ dex BT-SETTL and ATMO 2020 model atmospheric spectra, degraded to the wavelength-dependent resolution of the 0.3'' SpeX prism slit. This sequence spans the effective temperature range from 3000 K to 600 K and approximately corresponds to the ultracool dwarf spectral types M (top), L (middle), and T (bottom).

as defined by Caffau et al. (2011). To ensure a uniformly spaced grid for subsequent uncertainty analysis (Section 5), we omit the 50 K interval model spectra. Given that all our objects have spectral types $\geq M6$, we only consider model spectra up to a temperature of 3500 K to reduce computation time (the grid extends to 7000 K). Thus, the final BT-SETTL grid adopted in our fitting procedure spans effective temperatures (T_{eff}) of 1200–3500 K in steps of 100 K and surface gravities ($\log g$) of 2.5–5.5 dex in steps of 0.5 dex.

ATMO 2020 is one of the latest cloudless atmospheric model grid geared towards T and Y spectral type ultracool

dwarfs (Phillips et al. 2020). It brings numerous improvements to the evolutionary and spectroscopic modeling of this coldest subset of brown dwarfs. ATMO 2020 makes use of the new hydrogen and helium equation of state from Chabrier et al. (2019) in its interior structure model. It includes updated line lists for the most prominent molecular opacity sources such CH_4 and NH_3 from the ExoMol group (Tennyson & Yurchenko 2018) and significantly more transitions required to accurately model the atmospheres of brown dwarfs. Furthermore, ATMO 2020 provides a more detailed and careful treatment of the Na and K resonant lines, which play an important role in shaping the visible and red-optical spectra of ultracool dwarfs. Similar to BT-SETTL, each grid point in the model is calculated at solar metallicity ($Z = 0$ dex). In this work, we make use of the weak non-equilibrium chemistry model set (NEQ Weak). Numerous observations have highlighted the importance of non-equilibrium chemistry in the spectra of cool brown dwarfs due to vertical mixing in their atmospheres (e.g. Noll et al. 1997; Saumon et al. 2000; Geballe et al. 2009; Leggett et al. 2015). Phillips et al. (2020) model non-equilibrium chemistry by consistently coupling the relaxation scheme of Tsai et al. (2018) to their 1D atmosphere code ATMO while considering the non-equilibrium abundances of H_2O , CO, CO_2 , CH_4 , N_2 , and NH_3 . Similar to the approach with BT-SETTL, to ensure a uniformly spaced rectangular grid for subsequent uncertainty analysis (Section 5), we omit the 50 K interval model spectra. The final ATMO 2020 grid in our fitting procedure spans T_{eff} of 500–1800 K in steps of 100 K and $\log g$ of 2.5–5.5 dex in steps of 0.5 dex. We note that the NEQ Weak ATMO 2020 grid does not provide a spectrum for the $T_{\text{eff}} = 1100$ K and $\log g = 3.5$ dex grid point due to lack of convergence in the model generation. As a substitute, we use an interpolated model spectrum at this grid point (Mark Phillips; private communication). We refer the reader to Section 2 of Lueber et al. (2023) for a summary of brown dwarf atmospheric model grids not used in this work.

We begin by converting the PS1 optical (excluding y band since it is included in the wavelength range of the SpeX prism spectra) and WISE and Spitzer/IRAC MIR photometry to flux density measurements using the zero points for the corresponding filters. Model spectra are typically provided at high spectral resolution and are first degraded to the non-linear spectral resolution of the SpeX prism data ($R \sim 75$ –200) corresponding to the three different slit sizes of the SpeX spectrograph (Hurt et al., AAS Journals, submitted). Such a resolution degradation is, however, not required for fitting the optical and/or MIR photometry. Keeping this in mind, we apply the following method to each model spectrum.

First, we map the degraded model spectra to the wavelength grid of the SpeX prism data using cubic spline interpolation. Second, we synthesize the PS1 $griz$, WISE W1,

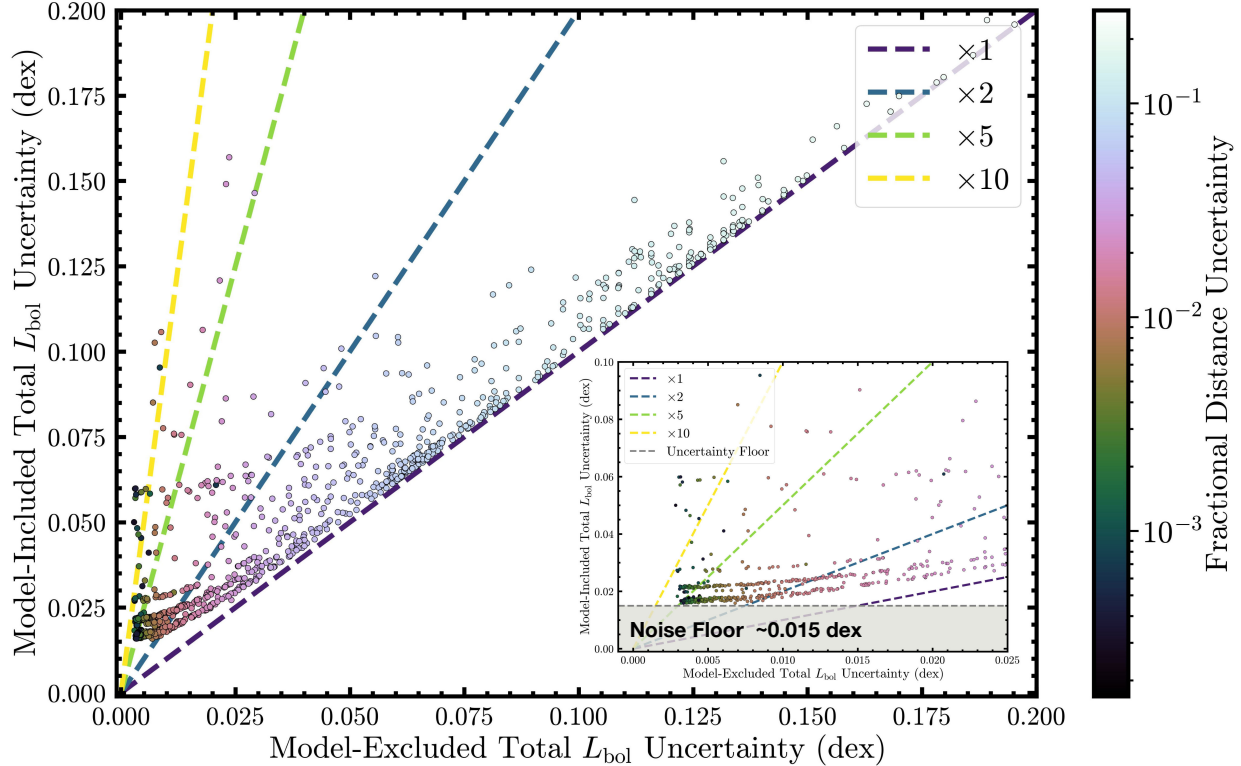


Figure 6. Summary of the bolometric luminosity uncertainty analysis in this work. The model-included total uncertainty (scale factor uncertainty + spectral data points uncertainties + model-contributed uncertainty + distance uncertainty) is plotted on the y-axis against the model-excluded total uncertainty (scale factor uncertainty + spectral data points uncertainties + distance uncertainty). Each point represents one of the 1054 objects in our sample and is colored based on the fractional uncertainty in the distance measurement for that object (color bar at right). Four dashed lines of slopes 1, 2, 5, and 10 plot differing multiplicative relations between the model-included total uncertainty and the model-excluded total uncertainty. The inset figure zooms in near the tail end of the points close to the origin. A noise floor of ≈ 0.015 dex is identified and marked with a dashed gray line. The model-contributed uncertainty component dominates for low fractional distance uncertainty objects, thereby limiting the gains possible with our high precision parallaxes.

W2, *W3*, and *W4*, and Spitzer/IRAC Channel 1 and Channel 2 photometric flux densities using the full resolution model spectra, following Equation 1. Third, we determine the scale factor k_{fit} for a given model spectrum that would minimize the combined χ^2 of the degraded model spectrum and the synthesized photometry fit to the observed SED. k_{fit} is given by

$$k_{\text{fit}} = \frac{\sum(f_i F_{k,i} / \sigma_{f,i})}{\sum(f_i^2 / \sigma_{f,i}^2)}, \quad (4)$$

where f_i represent the individual flux-calibrated SpeX prism flux densities or the individual PS1/WISE/IRAC bandpass photometric flux densities, $F_{k,i}$ represents the model spectrum or the synthesized PS1/WISE/IRAC photometry, and $\sigma_{f,i}$ represent the uncertainty in the observed SpeX spectrum or the PS1/WISE/IRAC photometry. To mitigate telluric contamination due to low atmospheric transmission in the water bands, we exclude spectral data points in the 1.355–1.415 μm and the 1.830–1.930 μm wavelength ranges from the above fitting procedure. Additionally, to avoid biasing the model fits, we exclude any spectral data points with unphysical S/N < -3 . This process is repeated for all available model spec-

tra and the model spectrum that yields the smallest χ^2 value is chosen as the best-fit model spectrum. Figure 4 shows an example flux-calibrated SED with the best-fit atmospheric model spectrum overlaid, as well as the associated χ^2 surface obtained from the fitting procedures.

5. BOLOMETRIC LUMINOSITIES

Given a flux-calibrated spectrum and best-fit atmospheric model spectrum, we computed the bolometric flux of each object by integration of the SED. We take care to correctly treat correlated and uncorrelated uncertainty contributions to the calculated bolometric flux.

5.1. Calculation and Uncertainty Analysis

We integrate the area under the SpeX spectrum to obtain the NIR contribution to the bolometric flux. The sum of the optical and MIR contribution is obtained by integrating the full resolution best-fit model spectrum at wavelengths outside those of the SpeX spectrum. The full wavelength range of our SED integration is ≈ 0.1 –2000 μm . Adding the two components, we obtain a bolometric flux measurement

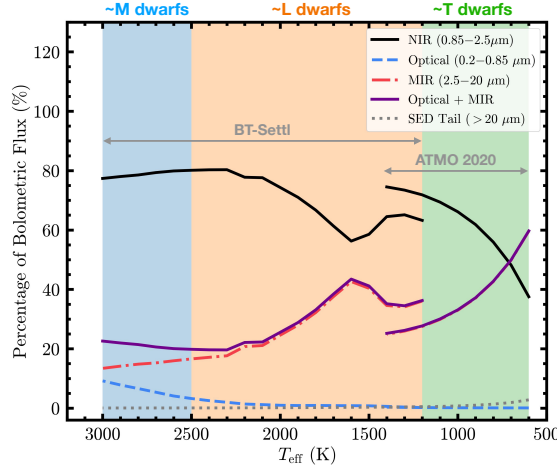


Figure 7. Percentage of bolometric flux contained in different wavelength regions as a function of effective temperature, computed by integrating BT-SETTL (1200–3000 K) and ATMO 2020 (600–1400 K) model spectra with $\log g = 4.0\text{--}5.5$. The shaded background areas roughly mark the temperature range corresponding to M, L, and T dwarfs. The NIR contribution dominates for the vast majority of spectral types. The SED tail flux ($20\text{--}2000 \mu\text{m}$) is a very small percentage of the bolometric flux across all spectral types. The MIR contribution is most important for objects cooler than $\sim 1800 \text{ K}$.

(f_{bol}). The uncertainty in f_{bol} is a combination of the uncertainty from the NIR contribution and the uncertainty from the summed optical and MIR contributions to the bolometric flux.

The uncertainty in the NIR flux contribution is defined as the calibration uncertainty and consists of the uncertainty in the scale factor k_{fit} for the entire SpeX spectrum and the measurement uncertainties for each individual spectral data point. We note that it only comes from the NIR contribution since we use the zero uncertainty model spectrum to estimate the optical and MIR contributions. The calibration uncertainty is determined using Monte Carlo techniques. We generate 10^4 different SpeX spectra by drawing the scaling factor and the value for each spectral data point from their corresponding posterior distributions. Each generated spectrum is integrated as described previously to obtain the NIR flux contribution. The standard deviation of these measurements yields the calibration uncertainty.

The uncertainty in the MIR and optical flux contribution is defined as the model-contributed uncertainty (σ_{mod}), which arises because the atmospheric model fit to the SpeX spectrum and optical/MIR photometry is not perfect. To calculate the model-contributed uncertainty, we re-compute the sum of the optical and MIR flux contributions to the bolometric flux using the four model spectra adjacent on the model grid in T_{eff} and $\log g$ values to the best-fit model spectrum. The standard deviation of this set of values gives the model-

contributed uncertainty (Cushing et al. 2008; Stephens et al. 2009).

The total uncertainty in the bolometric flux (δf_{bol}) is then obtained as the quadrature sum of the calibration and model-contributed uncertainty. Given a bolometric flux $f_{\text{bol}} \pm \delta f_{\text{bol}}$ and distance measurement $d \pm \delta d$, we can obtain the bolometric luminosity L_{bol} and the associated uncertainty δL_{bol} of the object as follows,

$$L_{\text{bol}} = f_{\text{bol}} \cdot 4\pi d^2, \quad (5)$$

$$\frac{\delta L_{\text{bol}}}{L_{\text{bol}}} = \sqrt{\left(\frac{\delta f_{\text{bol}}}{f_{\text{bol}}}\right)^2 + \left(2 \cdot \frac{\delta d}{d}\right)^2}. \quad (6)$$

For 839 objects in our sample, the distance is given by a parallax measurement. For the remaining 215 objects, we use photometric distances computed using absolute magnitude-spectral type relations for 2MASS JK_S , MKO JK , and WISE $W2$ bands. We use the polynomials from Dupuy & Liu (2012) for field objects with 2MASS JK_S , MKO JK , and ALLWISE $W2$ photometry; Feeser et al. (2022) for field objects with CatWISE $W2$ photometry; or this work (Appendix A) for young objects with 2MASS JK_S , MKO JK , and ALLWISE/CatWISE $W2$ photometry. The luminosities are reported as $\log(L_{\text{bol}}/L_\odot)$ where $L_\odot = 3.828 \times 10^{26} \text{ W}$ (Mamajek et al. 2015).

We examine the effect of the model-contributed uncertainty on the total uncertainty in our L_{bol} measurements by comparing this total L_{bol} uncertainty against the total L_{bol} uncertainty computed assuming zero model-contributed uncertainty. This is presented in Figure 6, where we have the defined the former quantity as the model-included total uncertainty and the latter quantity as the model-excluded total uncertainty. We find that the model-included total uncertainty is significantly larger than the model-excluded total uncertainty for low fractional distance uncertainty objects. A reduction in the fractional distance uncertainty from high precision parallax programs should have significantly lowered the total uncertainty in the bolometric luminosity (as seen for the $\sigma_{\text{mod}} = 0$ assumption case), but a non-zero σ_{mod} component results in an uncertainty floor at ≈ 0.015 dex. Thus, the central limiting factor for these cases is the presence of the model-contributed uncertainty. Obtaining high S/N spectra of ultracool dwarfs in the optical and MIR wavelengths will be crucial to lowering the identified noise floor.

5.2. Quality and Reliability of Atmospheric Model Fits

In this work, we estimate the flux contribution from the optical ($0.20\text{--}0.85 \mu\text{m}$) and MIR ($2.5\text{--}2000.0 \mu\text{m}$) wavelengths using atmospheric model spectra. Thus, it is important to characterize the quality and reliability of atmospheric model spectrum fits to the objects' NIR SpeX prism spectra and associated PS1 optical and WISE/Spitzer MIR photometry.

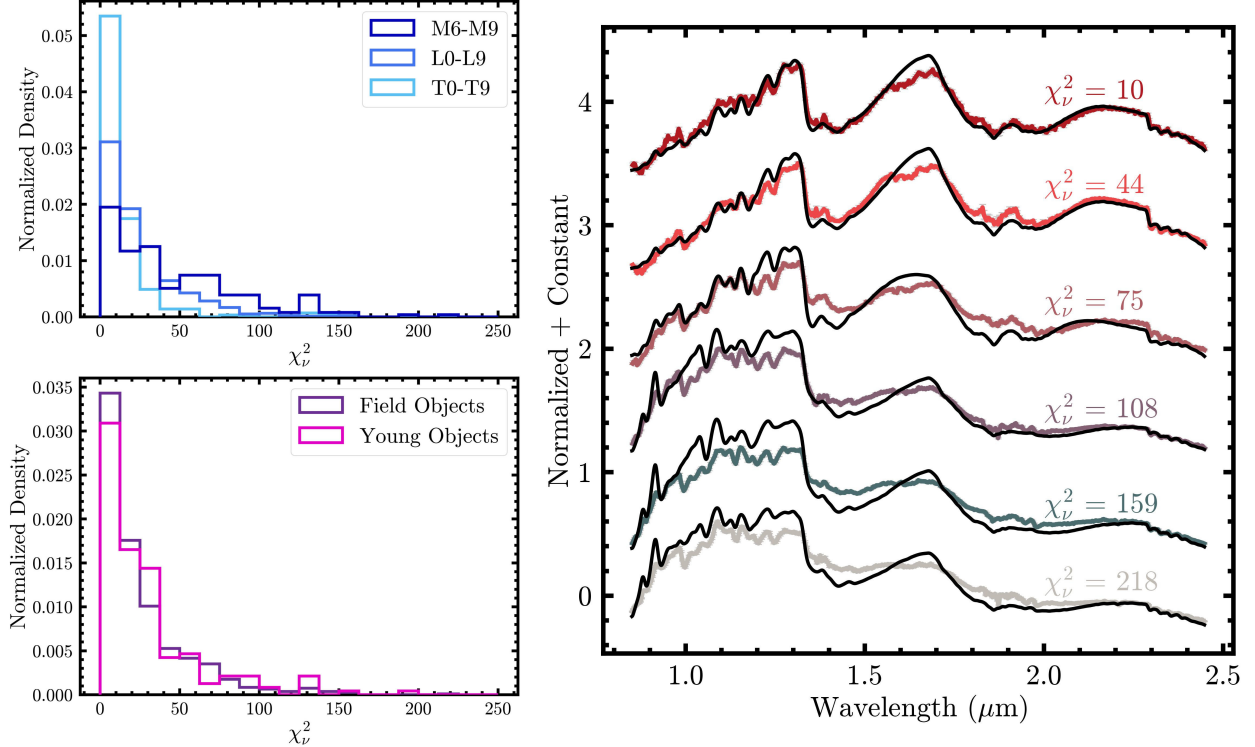


Figure 8. *Left:* Normalized distributions of the best-fit χ^2_ν values from the model atmosphere fitting for different spectral types (top) and different youth categories (bottom). Young moving group members and low gravity sources are designated as young objects. The bin size is 12.5. Both distributions are skewed significantly towards smaller χ^2_ν values, indicating good quality model fits for the vast majority of objects in the sample. Model fits to T dwarfs are better than those to L dwarfs, which are in turn better than those to M dwarfs. Field objects yield slightly better fits than young objects. We flag objects with $\chi^2_\nu > 50$ in the Table of Ultracool Fundamental Properties (see §5.2). *Right:* Example SpeX prism spectra and the corresponding best-fit model spectra for six objects in the sample with gradually increasing χ^2_ν values. The S/N of the spectra are similar (≈ 70 –100). This is a visual demonstration of the quality of the fits for different χ^2_ν values in the distribution.

The NIR flux contribution to an object’s bolometric flux is obtained by directly integrating the observed SpeX prism spectrum across a wavelength range of ≈ 0.85 – $2.5 \mu\text{m}$. To gauge the percentage of flux missing after this step, we plot the average percentage of the bolometric flux contained in three defined regions — the optical region (0.20 – $0.85 \mu\text{m}$), the MIR region (2.5 – $20.0 \mu\text{m}$), and the SED tail (20.0 – $2000.0 \mu\text{m}$) — as a function of effective temperature in Figure 7. These values are obtained by integrating the BT-SETTL and ATMO 2020 model spectra for each temperature in the defined region. We average flux percentage values computed across 4.0 – $5.5 \text{ dex log } g$ spectra (most typical range of surface gravities for ultracool dwarfs) at a fixed temperature. It is observed that the SED tail contribution to the bolometric flux is negligible (<4%) across all spectral types and does not affect our luminosity calculations. This quantity is important to check since the longest wavelength WISE photometry ($W4$) point that constrains our fits lies near $20 \mu\text{m}$. The MIR flux contribution to the bolometric flux is between ≈ 14 – 17% for M dwarfs, ≈ 16 – 45% for L dwarfs, and ≈ 25 – 60% for T dwarfs. The optical flux contribution is only significant for M dwarfs (≈ 3 – 10%). Thus, while the

NIR contribution dominates for the majority of objects, the MIR contribution does comprise a significant percentage of the bolometric flux, especially for the cooler $\gtrsim L5$ ultracool dwarfs. These are the objects for which the model fits must be examined in greater detail.

We use the reduced chi-square χ^2_ν as our figure of merit to quantify the goodness of our atmospheric model spectrum fit to the observed SED (SpeX spectrum + optical and MIR photometry). Figure 8 presents the distribution of our best-fit χ^2_ν values for different spectral classes and youth categories. The distributions are significantly skewed towards smaller χ^2_ν indicating good model fits to the data. The model fits have better (lower) χ^2_ν values for T dwarfs, followed by L and M dwarfs respectively. This is reassuring given that good quality model fits to the SEDs of the cooler ultracool dwarfs in our sample are important for accurate estimation of a significant percentage of their total bolometric flux. The distributions for field and young (young moving group members/low gravity sources) objects are roughly similar with slightly better (lower) χ^2_ν values for field objects. Figure 8 provides examples of atmospheric model spectra fits to the observed

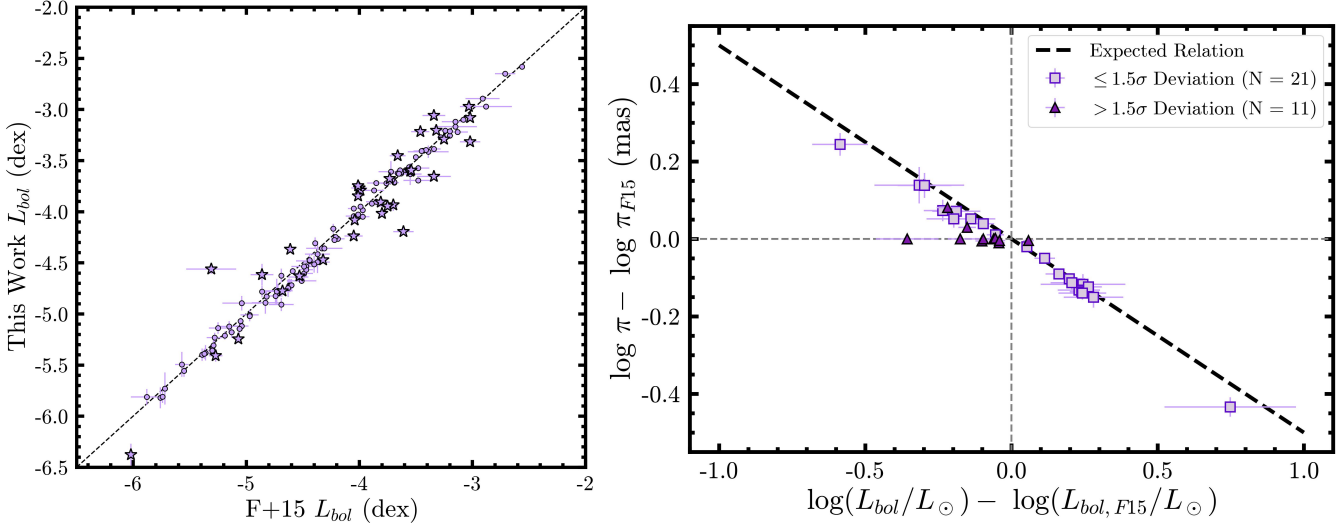


Figure 9. *Left:* Comparison of bolometric luminosities calculated in this work with those in Filippazzo et al. (2015) for objects common to the two samples. The dashed black line represents a 1:1 relation. Objects with disagreements ($>2\sigma$ discrepancy) in the two values are marked with a black-bordered star. *Right:* Logarithmic difference in parallax measurements used in the bolometric luminosity calculation vs logarithmic difference in bolometric luminosity measurements between this work and Filippazzo et al. (2015) for the *discrepant objects* in the left panel. The two gray dashed lines correspond to zero luminosity and parallax difference. The black dashed line corresponds to the expected relation between $\Delta \log \pi$ and $\Delta \log (L_{\text{bol}}/L_{\odot})$. Objects marked with a square correspond to the discrepant objects whose luminosity difference is consistent with the theoretically expected parallax difference within 1.5σ . Objects marked with a triangle correspond to the discrepant objects whose luminosity difference is *not* consistent with the theoretically expected parallax difference within 1.5σ . Observed differences in bolometric luminosity can thus be explained by changes in parallax measurements for the majority of discrepant objects.

SpeX prism spectra for six objects in our sample at different χ^2_{ν} values.

Based on the shape of the χ^2_{ν} distributions and visual inspection of the atmospheric model fits, we flag objects with χ^2_{ν} values greater than 50 in our Table of Ultracool Fundamental Properties (see §1) to indicate possibly lower reliability than the other fits. A total of 171 objects ($\sim 16\%$ of the sample) are flagged: 80 M dwarfs (39% of M dwarfs in our sample), 83 L dwarfs (13.4% of the L dwarfs in our sample), and 8 T dwarfs (3.5% of the T dwarfs in our sample). For these objects, the relatively poorer quality of the model spectrum fit may have impacted the estimated optical and MIR flux contribution, and hence the calculated bolometric luminosity. We note that the discrepancy is likely to be small for the majority of objects in this subset since the MIR contribution to the bolometric flux is significant, compared to the NIR contribution, primarily for \gtrsim L5 dwarfs (only 13 objects in the flagged subset).

5.3. Comparison with Filippazzo et al. (2015)

Figure 9 compares our L_{bol} values with those in Filippazzo et al. (2015) for objects common to the two samples ($N = 130$) and characterizes measurement differences as a function of the difference in parallaxes used in the calculations. We find that our results are consistent ($<2\sigma$ difference) with Filippazzo et al. (2015) for the majority of objects ($N = 98$). $>2\sigma$ discrepancy in the bolometric lu-

minosity is observed for 32 objects (Figure 9, left panel). The logarithmic difference in bolometric luminosity ($\Delta \log [L_{\text{bol}}/L_{\odot}]$) is related to the logarithmic difference in parallax ($\Delta \log \pi$) as $\Delta \log (L_{\text{bol}}/L_{\odot}) = -2 \cdot \Delta \log \pi$. We can use this scaling relationship to determine if the source of the discrepancy in bolometric luminosity is a revised parallax measurement. The differences in parallax measurements between our work and Filippazzo et al. (2015) can explain the differences in bolometric luminosity measurements (within 1.5σ) for 21 of the 32 discrepant objects (Figure 9, right panel). For the 11 discrepant objects (2MASSI J0825196+211552, 2MASSI J1546291-332511, 2MASSW J1506544+132106, 2MASSW J1515008+484742, DENIS-P J142527.97-365023.4, LHS 1604, LHS 2924, LP 412-31, SDSS J000013.54+255418.6, UGPS J072227.51-054031.2, and Wolf 359) where the difference in parallax measurements is not consistent with the theoretical scaling relation within 1.5σ , the minor differences observed in L_{bol} values may be attributed to our use of atmospheric models to evaluate the optical and MIR flux contributions to the bolometric flux in contrast to the use of the object’s optical and (in some cases) MIR spectra (combined with linear interpolation across SED gaps), as in Filippazzo et al. (2015). A complete list of the 32 discrepant objects is provided in Table 4. Overall, our work increases the sample size of L_{bol} measurements by a factor of ~ 5 (Figure 10).

Table 4. Objects with $>2\sigma$ Disagreement between This Work’s and Filippazzo et al. (2015)’s Bolometric Luminosity Measurements

UCS Name	F+15 Name	π	π (F+15)	$\log(L_{bol}/L_\odot)$	$\log(L_{bol}/L_\odot)$ (F+15)
		(mas)	(mas)	(dex)	(dex)
2MASS J00332386-1521309	0033-1521	43.50 ± 0.80	24.8 ± 2.5	-4.20 ± 0.03	-3.61 ± 0.09
2MASS J00345157+0523050	0034+0523	118.80 ± 2.70	105.4 ± 7.5	-5.41 ± 0.06	-5.27 ± 0.06
2MASS J03231002-4631237	0323-4631	23.40 ± 0.70	17.0 ± 3.0	-3.66 ± 0.03	-3.34 ± 0.15
2MASS J06085283-2753583	0608-2753	22.62 ± 0.16	32.0 ± 3.6	-3.06 ± 0.02	-3.34 ± 0.10
2MASS J09490860-1545485	0949-1545	42.20 ± 2.70	55.3 ± 6.6	-4.62 ± 0.10	-4.86 ± 0.10
2MASS J13595510-4034582	1359-4034	47.35 ± 0.20	64.2 ± 5.5	-3.77 ± 0.02	-4.0 ± 0.07
2MASSI J0439010-235308	0439-2353	80.70 ± 0.40	110.4 ± 4.0	-4.37 ± 0.03	-4.61 ± 0.03
2MASSI J0445538-304820	0445-3048	61.94 ± 0.15	78.5 ± 4.9	-3.79 ± 0.02	-3.99 ± 0.05
2MASSI J08251964-211552*	0825+2115	92.60 ± 0.80	93.8 ± 1.0	-4.63 ± 0.02	-4.53 ± 0.01
2MASSI J0835425-081923	0835-0819	138.31 ± 0.21	117.3 ± 11.2	-4.24 ± 0.02	-4.05 ± 0.08
2MASSI J0847287-153237	0847-1532	57.51 ± 0.21	76.5 ± 3.5	-3.75 ± 0.02	-4.01 ± 0.04
2MASSI J1546291-332511*	1546-3325	88.00 ± 1.90	88.0 ± 1.9	-5.25 ± 0.04	-5.07 ± 0.02
2MASSI J2104149-103736	2104-1037	58.02 ± 0.27	53.0 ± 1.71	-3.91 ± 0.02	-3.81 ± 0.03
2MASSW J1155395-372735	1155-3727	84.73 ± 0.15	104.4 ± 4.7	-3.85 ± 0.02	-4.01 ± 0.04
2MASSW J1506544+132106*	1506+1321	85.43 ± 0.19	70.92 ± 2.5	-4.02 ± 0.02	-3.8 ± 0.03
2MASSW J1515008+484742*	1515+4847	101.96 ± 0.26	95.24 ± 2.0	-4.47 ± 0.02	-4.32 ± 0.02
2MASSW J1552591+294849	1552+2948	48.90 ± 0.16	47.7 ± 0.9	-3.60 ± 0.02	-3.55 ± 0.02
2MASSW J2208136+292121	2208+2921	25.10 ± 1.60	21.2 ± 0.7	-3.93 ± 0.06	-3.7 ± 0.03
BR B0246-1703	0246-1651	44.62 ± 0.13	61.6 ± 5.4	-3.22 ± 0.02	-3.46 ± 0.08
DENIS-P J0751164-253043	0751-2530	56.42 ± 0.12	59.15 ± 0.84	-3.68 ± 0.02	-3.73 ± 0.01
DENIS-P J142527.97-365023.4*	1425-3650	84.40 ± 0.30	86.45 ± 0.83	-4.08 ± 0.02	-4.04 ± 0.01
ESO 207-61	0707-4900	41.69 ± 0.11	54.1 ± 4.5	-3.45 ± 0.02	-3.66 ± 0.07
G 196-3B	1004+5022	46.20 ± 0.50	41.0 ± 4.1	-3.95 ± 0.02	-3.75 ± 0.09
LHS 1604*	0351-0052	68.12 ± 0.07	68.1 ± 1.9	-3.08 ± 0.02	-3.02 ± 0.02
LHS 2924*	1428+3310	91.16 ± 0.10	90.8 ± 1.3	-3.60 ± 0.02	-3.54 ± 0.01
LHS 3003	1456-2809	141.79 ± 0.06	159.2 ± 5.1	-3.21 ± 0.02	-3.32 ± 0.03
LP 412-31*	0320+1854	68.27 ± 0.08	68.9 ± 0.6	-3.29 ± 0.02	-3.25 ± 0.01
SDSS J000013.54+255418.6*	0000+2554	70.80 ± 1.90	70.8 ± 1.9	-4.78 ± 0.04	-4.68 ± 0.02
TVLM 831-161058	0251+0047	28.16 ± 0.18	20.5 ± 2.2	-3.32 ± 0.02	-3.02 ± 0.09
UGPS J072227.51-054031.2*	0722-0540	242.80 ± 2.40	242.8 ± 2.4	-6.38 ± 0.11	-6.02 ± 0.02
WISEPA J164715.59+563208.2	1647+5632	42.70 ± 2.10	116.0 ± 29.0	-4.56 ± 0.05	-5.31 ± 0.22
Wolf 359*	1056+0700	415.18 ± 0.07	419.1 ± 2.1	-2.97 ± 0.02	-3.03 ± 0.00

NOTE—For objects marked with an asterisk (*), the difference in parallax measurements is not consistent with the theoretical $\Delta \log(L_{bol}/L_\odot) = -2 \cdot \Delta \log \pi$ scaling relation within 1.5σ . For the remaining objects, the difference in parallax measurements is consistent with the theoretical scaling relation within 1.5σ . See §5.3 for more details.

5.4. Polynomial Relations

We derive empirical relationships between the bolometric luminosity and spectral type/absolute magnitude for field and young objects by performing inverse variance-weighted polynomial fits to the data. The polynomial fit is carried out for increasing orders and a lack-of-fit test (F -test) is conducted for the best-fit coefficients at each order to determine if a higher-order fit is necessary to explain the data. We reject the null-hypothesis (higher-order fit required) for $p > 0.05$. A root-mean-square (rms) value is determined to quantitatively characterize the scatter about the best-fit relation. We note here that the F -test does not always yield a definitive answer for the order of the polynomial based on the $p > 0.05$ rejection criterion. For such cases, we adopt the lowest order after which p does not change significantly (factor of $\sim 5-10$) as the best-fit polynomial and validate it by visual inspection.

Figure 11 summarizes our L_{bol} measurements as a function of spectral type and presents the corresponding sixth-order polynomial relation (Table 5). For M dwarfs ($SpT = 6 - 9.5$), young objects show considerable scatter from the relation, as was observed by Filippazzo et al. (2015). However, for later types, young objects do not scatter significantly different than the field-age objects, an observation not previously confirmed given the small sample size of ultracool dwarf measurements available. While the relation does not exhibit significant differences compared to Filippazzo et al. (2015), our larger sample size enables a robust determination of the rms scatter in the polynomial relation.

Figures 12 and 13 summarize our L_{bol} measurements as a function of absolute magnitude in the MKO JHK , PS1 zy , and WISE $W1$ and $W2$ bands. The full set of polynomial relations (including those for 2MASS JHK_S) are presented

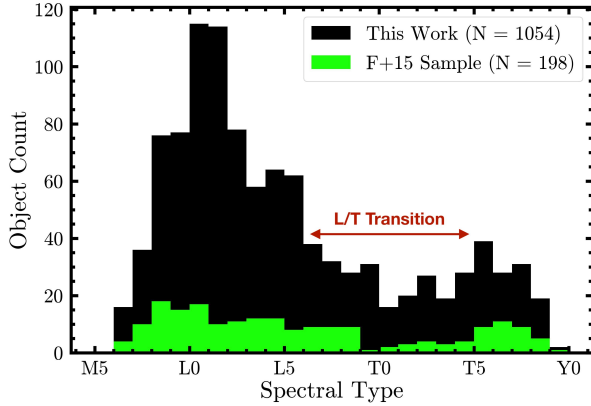


Figure 10. A comparison of the number of SED-integrated L_{bol} measurements available as a function of spectral type (SpT) before (Filippazzo et al. 2015) and after this work. The bin size is 1 SpT. We increase the sample size of L_{bol} values by a factor of ~ 5 and contribute a significant number of measurements in the L/T transition region.

in Table 5. We find that the MKO H -band polynomial relation is the most reliable choice for L_{bol} determinations using absolute magnitudes, based on its linearity, low rms scatter about the fit, and insensitivity to age and spectral type information.

6. AGES

In order to compute properties of ultracool dwarfs from evolutionary models, we must first estimate ages for all the objects. There is no single definitive method for doing this, so we employ multiple methods, making best use of the objects’ available measurements and previous assessments in the literature. We follow a tiered approach to assigning ages, with the following priority order:

1. *Membership in a stellar association or moving group:* The BANYAN Σ algorithm (Gagné et al. 2018) provides a means for uniform probability assessment of objects’ memberships in stellar associations or young moving groups (YMGs) within 150 pc based on kinematics (UVW) and position (XYZ), including handling objects that are missing parallax and/or radial velocity (RV) measurements. We process our entire sample using this algorithm, using the highest S/N astrometry for each object as compiled in *The Ultracool-Sheet*. An object is designated as a YMG member if the BANYAN Σ membership probability is $\geq 90\%$ and then assigned the corresponding YMG age tabulated in Gagné et al. (2018), assuming a normal age distribution for ages originating from Bell et al. (2015) and a uniform age distribution for all other ages. (We note that BANYAN Σ is a probabilistic assessment based on an assumed spatial-kinematic model of the solar neighborhood, and individual objects of interest might benefit from greater scrutiny using additional methods.)

In order to retain information about objects that might be members, especially with the addition of missing measurements (typically RVs), we assign potential membership for objects with probabilities of 80–90% and tag these with a “?” suffix (e.g. “ABDMG?” indicates potential membership in the AB Dor moving group). This suffix is also used for objects whose BANYAN Σ analysis was done with a photometric distance rather than a parallactic one. Finally, for objects where the BANYAN Σ calculation was done with the full 6-d information, we append a “!” suffix (e.g., “ABDMG!”) to indicate the greater robustness of this membership assignment as compared to most objects, where only 5-d information is available since RV measurements are much less common than astrometry and proper motions. In total, 61 objects are designated as YMG members based on the $\geq 90\%$ probability + parallactic distance criterion (for 22 out of these 61 objects, the full 6-d information is available). 30 additional objects are designated as potential YMG members based on the 80–90% probability criterion. 3 objects with a $\geq 90\%$ BANYAN Σ probability are also designated as potential YMG members based on the use of a photometric distance.

2. *Companionship to a star:* For ultracool companions with spectral types L6 and later, we use the literature compilation of ages for the primary stars (Kirkpatrick et al. 2001; Seifahrt et al. 2005; Valenti & Fischer 2005; Reid & Walkowicz 2006; Luhman et al. 2007; Burgasser et al. 2010b; Deacon et al. 2012b,a; Pinfield et al. 2012; Deacon et al. 2014, 2017; Miles-Páez et al. 2017; Gauza et al. 2019; Zhang et al. 2020, 2021a,c). For 7 companions in our sample, *The UltracoolSheet* does not yet include the literature host star ages, so these objects are not included in the evolutionary model analysis that follows. In total, 78 objects are assigned ages based on the age of the primary star.
3. *Spectroscopic gravity:* Spectroscopic signatures of low-gravity in either optical (e.g. Cruz et al. 2009) or near-IR (e.g. Allers & Liu 2013) spectra indicate that an object is young enough ($\lesssim 300$ Myr) such that its radius is inflated compared to older (higher-gravity) field objects. We use the set of objects with low-gravity spectra that reside in young moving groups and stellar associations (as determined above with BANYAN Σ) to examine the age range corresponding to the different gravity classes. We find objects with VL-G near-IR spectra (18 objects) are present in regions with ages of 10–150 Myr (bounded by the TW Hya Association

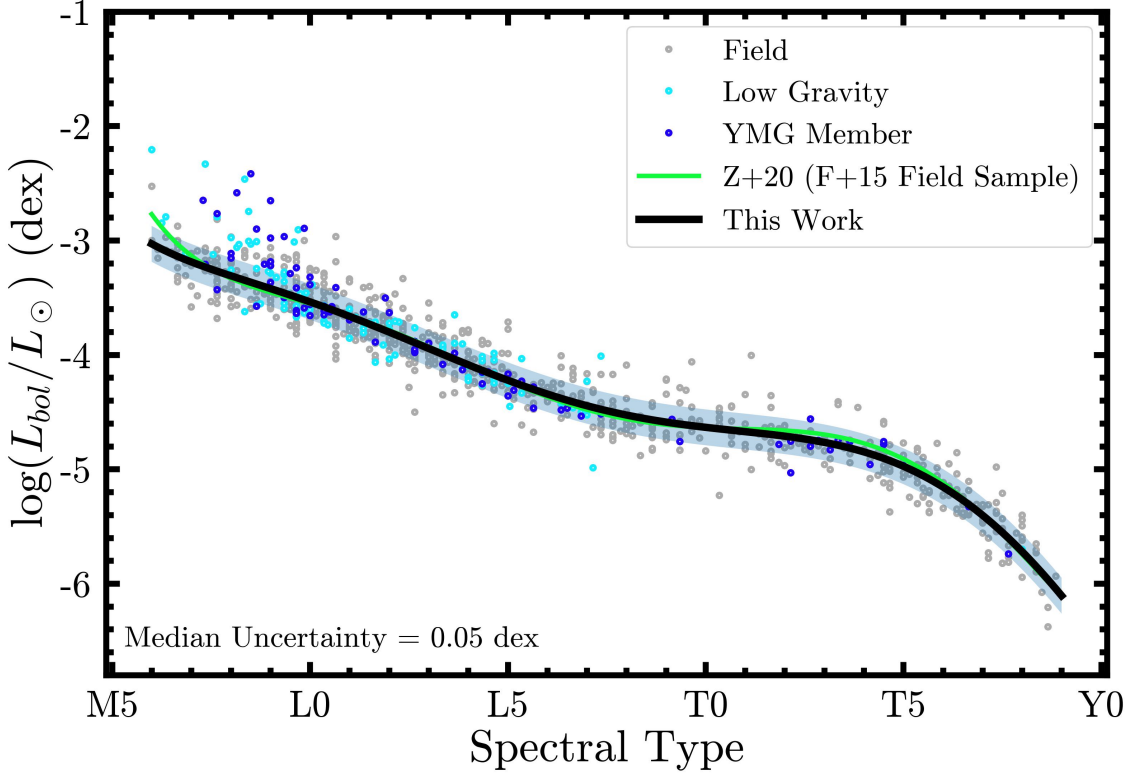


Figure 11. Bolometric luminosities derived for our sample of 1054 ultracool dwarfs as a function of their spectral type (SpT). Field objects, low gravity ultracool dwarfs, and young moving group members are marked by gray, cyan, and blue points respectively. Random scatter in the x direction with amplitude 0.3 SpT is applied to avoid overlapping points. Due to the large number of points, uncertainties in individual measurements are not shown for figure readability. The black line is the best sixth-order weighted polynomial fit to the data and the shaded blue region represents the rms scatter about the fit. The polynomial relation from Zhang et al. (2020, Z+20) derived using bolometric luminosities of 198 field-age ultracool dwarfs from Filippazzo et al. (2015, F+15) is plotted as a green solid line for comparison.

and the AB Dor moving group⁴) while objects with INT-G near-IR spectra (42 objects) span a range of 20–250 Myr (bounded by the β Pic moving group and the cooling age for the INT-G binary system LP 349-25 [Dupuy & Liu 2017]). We assume uniformly distributed age values within each range. Each gravity class does not correspond to a unique age range, as a given moving group may have sources with both gravity classes (e.g. Aller et al. 2016). For objects with optical gravity classifications, we treat the β classification (8 objects) as equivalent to INT-G and the δ (1 object) and γ (13 objects) classifications as equivalent to VL-G. For cases where the optical and near-IR gravity classes are both young but do not agree, or the optical gravity class is uncertain, we adopt an age range that encompasses both gravity classifications: 10–250 Myr for $\beta+$ VL-G (2 objects), $\gamma+$ INT-G

(3 objects), and $\beta+\gamma$ (1 object), except for the few objects with $\beta+$ FLD-G (4 objects) where we assume 20–250 Myr. For objects with low-gravity spectral signatures but no formal gravity class in the literature (designated as low g), we adopt a uniform distribution of 10–300 Myr (1 object). Finally for objects with FLD-G gravity (148 objects), we assume the same field-age distribution from Dupuy & Liu (2017) described below but with an elevated lower bound of 300 Myr.

4. *Field age:* For all remaining objects, i.e., those lacking evidence of youth or ages based on group membership or companionship (634 objects), we assign an age drawn from the distribution of Dupuy & Liu (2017, hereafter DL17). The DL17 age distribution was empirically determined based on high precision dynamical mass measurements of 10 ultracool dwarf binaries and is found to be consistent with the Besançon model of the solar neighborhood (Robin et al. 2003). The Besançon model predicts a field age distribution skewed towards younger ages since dynamical heating preferentially excites older objects out of the mid-plane of the Galaxy. According to DL17 age distribu-

⁴ Younger sources in star-forming regions, e.g., Taurus and Upper Sco, also show VL-G spectra (e.g. Zhang et al. 2018) but since our sample does not include such regions, we take 10 Myr as the lower age bound for this gravity class.

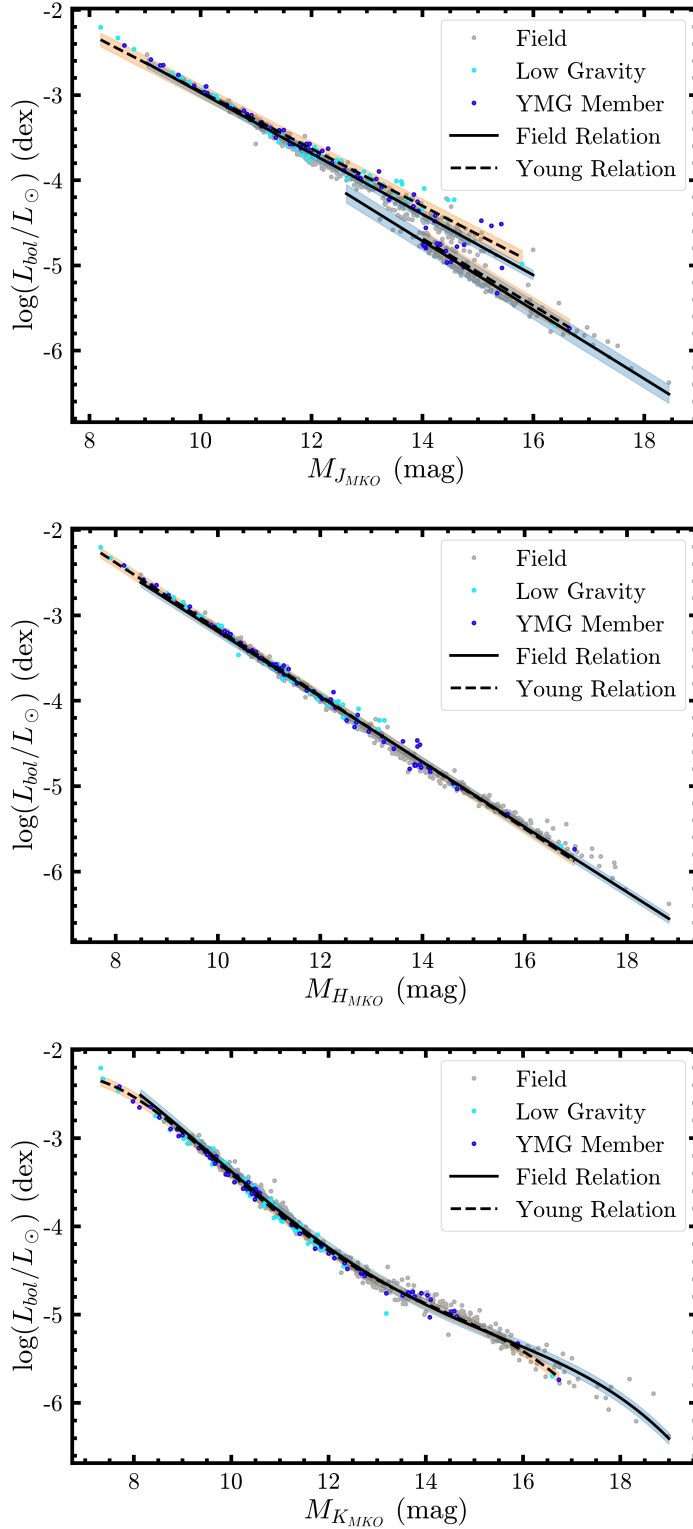


Figure 12. Bolometric luminosity vs absolute magnitude in the MKO JHK bands. Symbols are the same as in Figure 11. The black solid and dashed lines are the best-fit polynomial relations for the field and young objects, respectively. The shaded blue and orange regions represent the rms scatter about the field and young object fits, respectively.

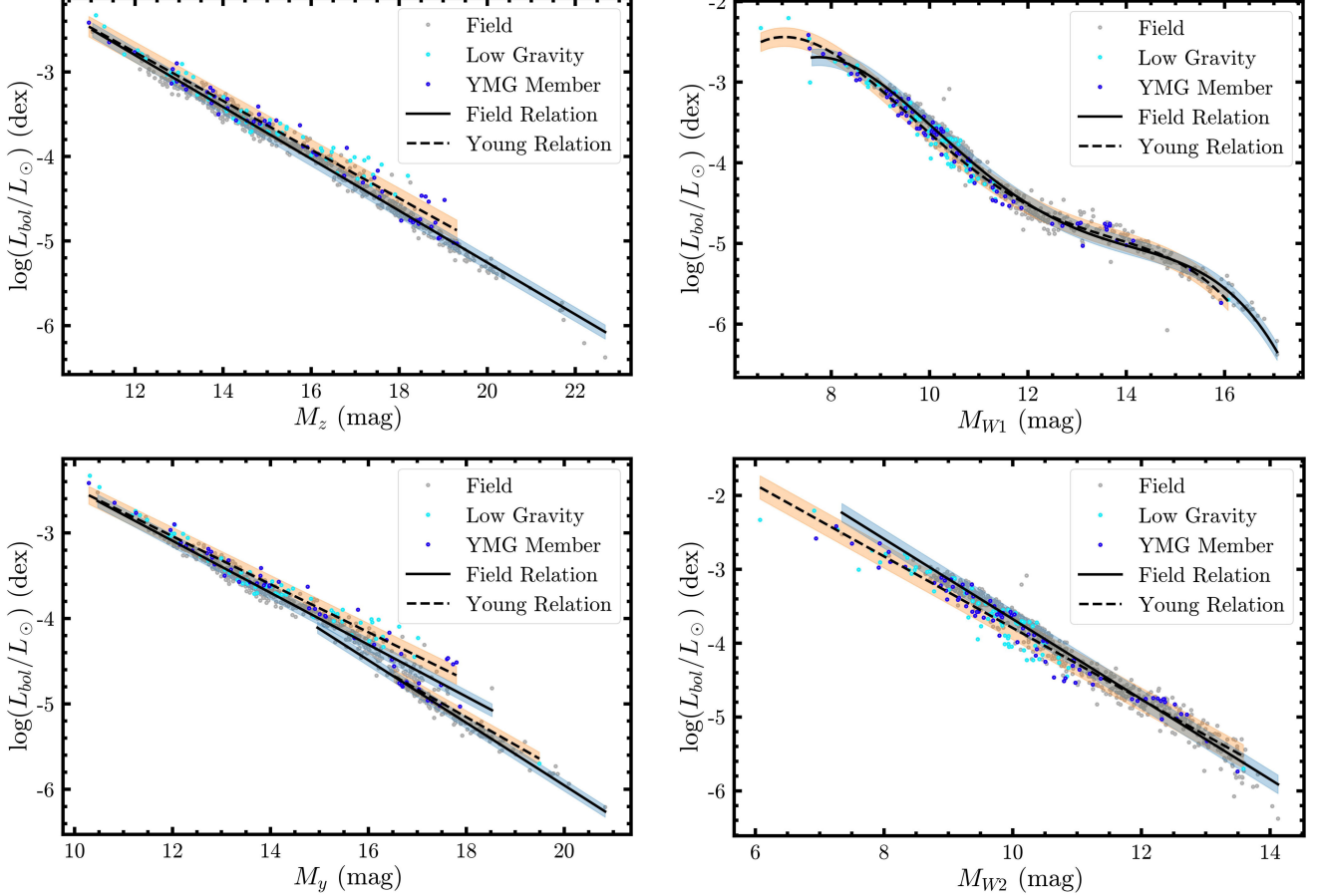


Figure 13. Same as Figure 12 for PS1 zy and WISE $W1$ and $W2$ bands.

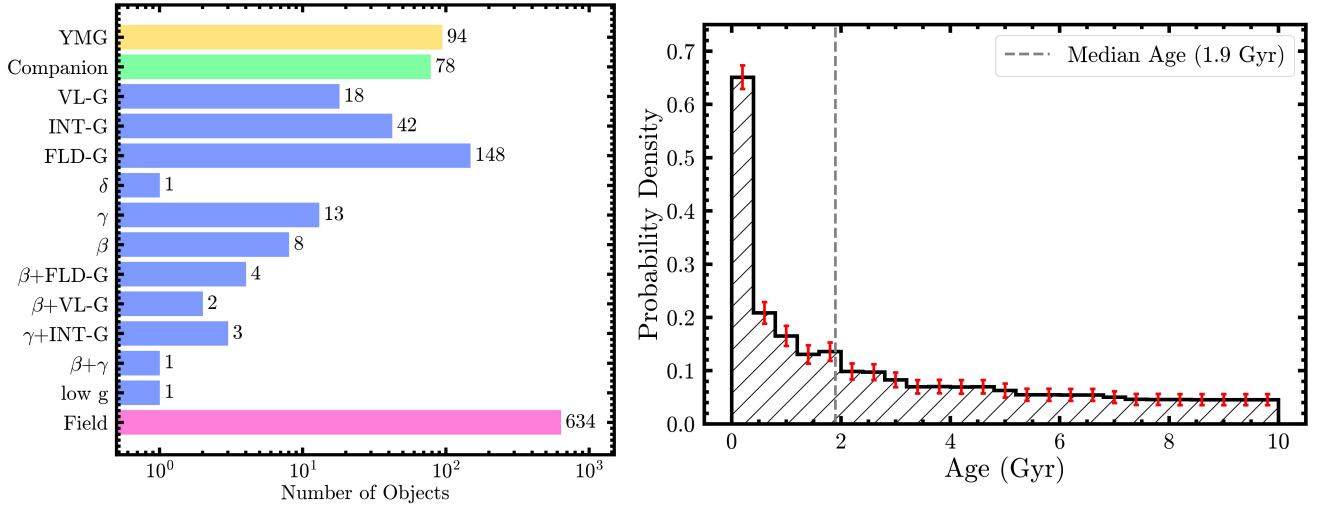


Figure 14. Age properties of the ultracool dwarf sample. *Left:* Number of objects in the sample in each age category as described in §6. The corresponding count is listed to the right of each bar. *Right:* Mean age distribution of objects in the sample based on Monte Carlo simulations. The bin size is 0.4 Gyr. Uncertainty in the density for each bin is marked with a red errorbar. The median age for the sample is 1.9 Gyr.

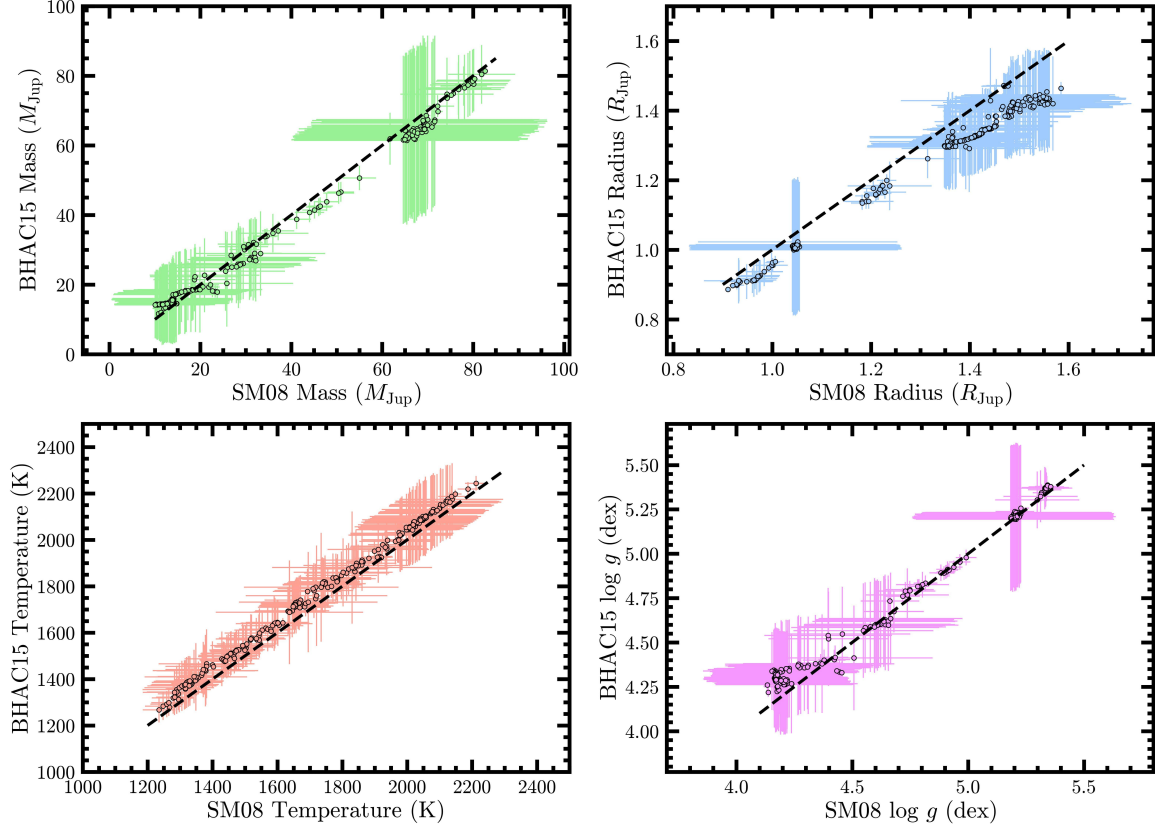


Figure 15. Comparison of masses, radii, effective temperatures, and surface gravities derived with BHAC15 and SM08 evolutionary models. The dashed black line in each panel represents a 1:1 relation between the compared parameters. While the parameters obtained are statistically consistent, we find that BHAC15 generally predicts higher temperatures and smaller radii than SM08.

tion, the ages are uniformly distributed in the following Besançon model bins, where each bin contains a fraction of the total population as follows: 8.1% for 0.01–0.15 Gyr, 20.0% for 0.15–1 Gyr, 16.1% for 1–2 Gyr, 11.9% for 2–3 Gyr, 16.6% for 3–5 Gyr, 12.9% for 5–7 Gyr, and 14.4% for 7–10 Gyr. We adopt this as an age probability density function for each field object.

The number of ages obtained with each method is summarized in the left panel of Figure 14. We derive the age distribution of our ultracool dwarf sample using Monte Carlo simulations. 10^5 ages are drawn for each object from their assigned age distributions. We construct a sample age distribution spanning 0–10 Gyr with a bin size of 0.4 Gyr from the drawn ages of all objects in each trial. The mean age distribution is derived by averaging the density values across the 10^5 sample age distributions in each bin. Uncertainty in the density value of each bin is obtained using the standard deviation. The right panel of Figure 14 shows the mean age distribution with uncertainties. The median age of the sample is 1.9 Gyr.

7. EVOLUTIONARY MODEL-DERIVED PARAMETERS

In this section, we use the bolometric luminosities (Section 5) derived for all objects in our sample along with their age estimates (Section 6) as inputs to the [Saumon & Marley \(2008, SM08\)](#) hybrid and [Baraffe et al. \(2015, BHAC15\)](#) evolutionary model grids to estimate their masses, radii, surface gravities, and effective temperatures. Ultracool dwarfs in our sample span a wide range of luminosities and thus, in some cases, are too bright for the SM08 models ($\log(L_{\text{bol}}/L_{\odot}) \gtrsim -3$) or too faint for the BHAC15 models ($\log(L_{\text{bol}}/L_{\odot}) \lesssim -4.5$). We use each evolutionary model grid in its respective non-overlapping luminosity-age space. In the region of model overlap, we derive the fundamental properties with both sets of models.

7.1. Bayesian Rejection Sampling

To estimate ultracool dwarf masses, radii, and surface gravities by interpolation of evolutionary model grids, we implement the Bayesian rejection sampling method described in [Dupuy & Liu \(2017\)](#). The first step is to randomly draw 10^6 $\log L_{\text{bol},\text{model}}$ samples from a uniform distribution spanning the bolometric luminosity range of the evolutionary model grid. The second step involves randomly sampling the object's age distribution, calculating χ^2 values for the sampled ages, and computing a probability for each sample. The ex-

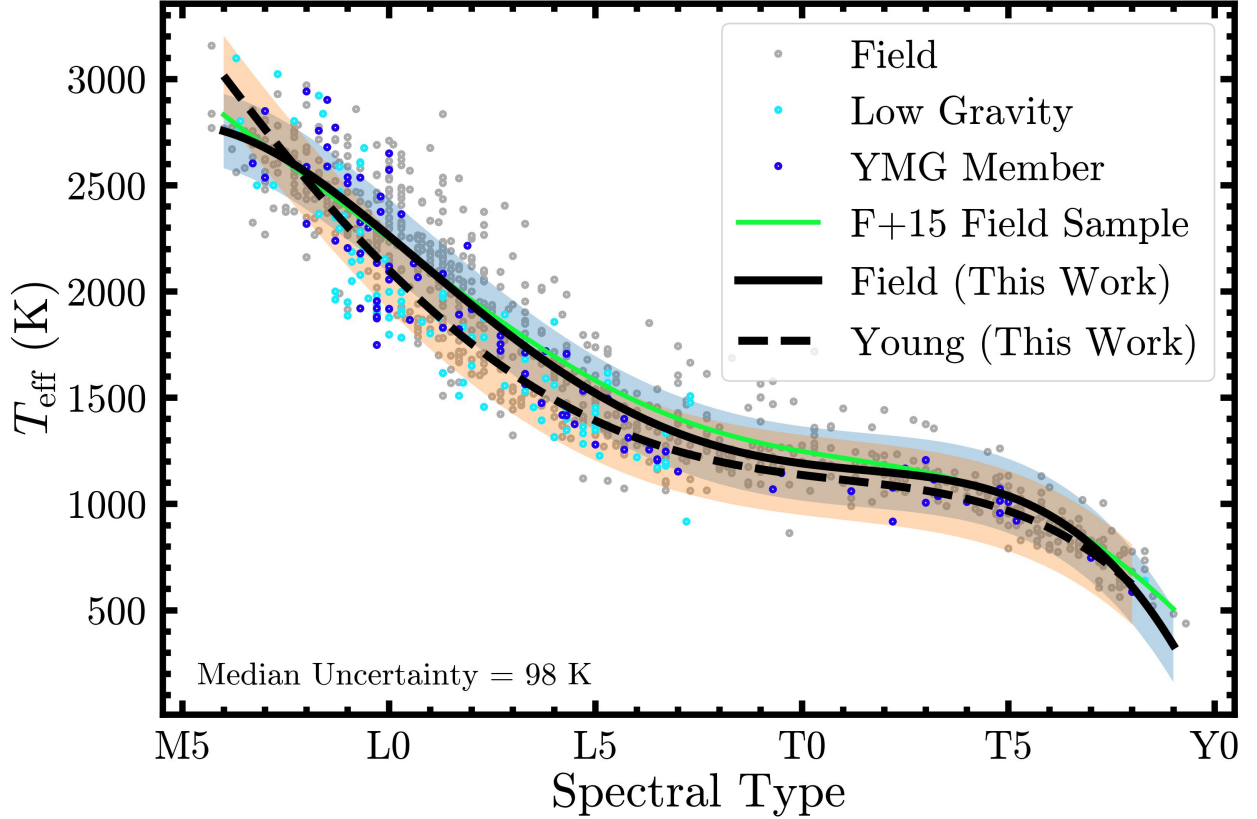


Figure 16. Effective temperatures derived for our sample of 1054 ultracool dwarfs as a function of their spectral type (SpT). Symbols are the same as in Figure 11. Random scatter in the x direction with amplitude 0.3 SpT is applied to avoid overlapping points. The black solid and dashed lines are the weighted best-fit polynomial relations for field and young objects, respectively. The shaded blue and orange regions represent the rms scatter about the field and young object fits, respectively. The field polynomial relation from Filippazzo et al. (2015, F+15) is plotted as a green solid line for comparison.

act implementation of this step depends on the adopted age distribution.

Normal Age Distribution: $10^6 \log t_{\text{model}}$ samples are randomly drawn from a uniform distribution spanning the age range of the evolutionary model grid. We compute χ^2 for each sample,

$$\chi^2 = \frac{(\log L_{\text{bol},\text{model}} - \log L_{\text{bol}})^2}{\sigma_{\log L_{\text{bol}}}^2} + \frac{(\log t_{\text{model}} - \log t)^2}{\sigma_{\log t}^2}, \quad (7)$$

where $\log L_{\text{bol}} \pm \sigma_{\log L_{\text{bol}}}$ is the bolometric luminosity measurement and $\log t \pm \sigma_{\log t}$ is the age measurement for the object. The χ^2 for each sample is converted to a probability p , normalizing by the sample with the minimum χ^2 , as follows,

$$p = \exp \left[-\frac{1}{2} (\chi^2 - \chi_{\min}^2) \right]. \quad (8)$$

Uniform Age Distribution: $10^6 \log t_{\text{range}}$ samples are randomly drawn from a uniform distribution spanning the intersection of the quoted age range and the evolutionary model grid age range. We compute the χ^2 for each sample, in this

case, as follows,

$$\chi^2 = \frac{(\log L_{\text{bol},\text{model}} - \log L_{\text{bol}})^2}{\sigma_{L_{\text{bol}}}^2}. \quad (9)$$

The χ^2 for each sample is converted to a probability p , normalizing by the sample with the minimum χ^2 using Equation 8.

DL17 Age Distribution: $10^6 \log t_{\text{DL17}}$ samples are randomly drawn from a uniform distribution spanning the intersection of the DL17 age range and the evolutionary model grid age range. In each case, the χ^2 for each sample (Equation 9) is converted to a probability p_* , normalizing by the sample with the minimum χ^2 using Equation 8. We then compute the likelihood of drawing the sampled age from the DL17 distribution (truncated at 300 Myr) for field-age (FLD-G) objects $p_{\text{DL17}} = p(\log t_{\text{DL17}} | \text{DL17})$. The final probability for each sample, normalized by the sample with the highest probability, is,

$$p = \frac{p_* \cdot p_{\text{DL17}}}{\max(p_* \cdot p_{\text{DL17}})} \quad (10)$$

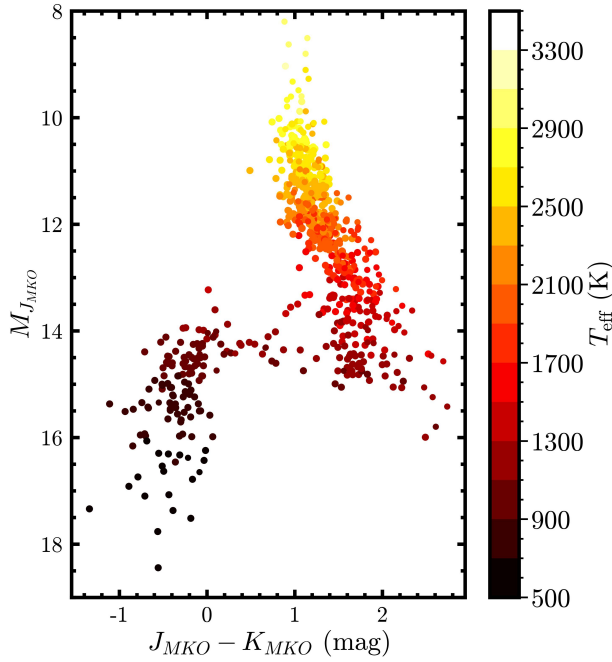


Figure 17. MKO M_J vs $J - K$ color-magnitude diagram for ultracool dwarfs in our sample with individual points colored by their derived effective temperatures. Spectral blends and overluminous objects have been excluded. Due to the large number of points, uncertainties in individual measurements are not shown for figure readability. The median uncertainty in $M_{J_{\text{MKO}}}$ is 0.06 mag and in $J - K$ is 0.05 mag.

The third step is to randomly draw 10^6 uniform variates (u) distributed in the range from 0 to 1 and reject any samples where $p < u$. The fourth and final step is to linearly interpolate the evolutionary models at each accepted luminosity-age point to calculate the corresponding mass (log M), radius (log R), and surface gravity (log g). The final mass/radius/gravity measurement and uncertainty are obtained as the median and standard deviation of all the sample’s mass/radius/gravity values. Our measurements are summarized in the Table of Ultracool Fundamental Properties associated with this paper (see §1). A total of 243 sources’ parameters were estimated using both BHAC15 and SM08, 339 sources’ parameters were estimated using only BHAC15, and 464 sources’ parameters were estimated using only SM08.

The choice of a given model, SM08 or BHAC15, for the adopted measurements is based on the following conditions. BHAC15 is used if the 1σ lower limit of the measured bolometric luminosity is greater than the luminosity on the lowest mass luminosity-age model track interpolated at the 1σ lower limit of the measured age (or lower limit of the quoted age range). SM08 is used if the 1σ upper limit of the measured bolometric luminosity is less than the luminosity on the highest mass luminosity-age model track interpolated at the 1σ upper limit of the measured age (or upper limit of the

quoted age range). When both conditions are satisfied, calculations are made using both evolutionary models. In the Table of Ultracool Fundamental Properties associated with this paper (see §1), we present the lower uncertainty measurement in such cases. Figure 15 presents a comparison of the fundamental parameters derived between BHAC15 and SM08. While the parameters obtained with BHAC15 and SM08 are statistically consistent, we find that BHAC15 generally predicts higher temperatures (by ≈ 50 K) and smaller radii (by $\approx 0.06 R_{\text{Jup}}$) than SM08.

This method significantly differs from the process implemented in Filippazzo et al. (2015). To estimate an object’s radius (which is used to derive effective temperature) and mass, Filippazzo et al. (2015) determine a parameter range for each source spanning the minimum and maximum values of all evolutionary model predictions given an object’s bolometric luminosity and age. They quote the average of the minimum and maximum value as the final radius/mass and half the radius/mass range as the uncertainty in Table 9. However, this method does not take into account the shape of the underlying radius/mass distribution when estimating the object’s properties. Except for the case of a uniform distribution, the average parameter value does not correspond to the distribution’s true expectation value. This is further complicated by the use of parameter estimates from several sets of evolutionary models to construct a single range in Filippazzo et al. (2015). Our Bayesian rejection sampling technique addresses the limitations of the above method by deriving each object’s underlying radius and mass distribution independently for each of the two evolutionary model sets in this work. The median value computed from the parameter’s cumulative distribution function is then quoted as our final value.

7.2. Effective Temperature

Effective temperatures are calculated using the evolutionary model-inferred radius R and SED-integrated bolometric luminosity measurement L_{bol} using the Stefan-Boltzmann Law,

$$T_{\text{eff}} = \left(\frac{L_{\text{bol}}}{4\pi R^2 \sigma_{\text{SB}}} \right)^{\frac{1}{4}}, \quad (11)$$

where σ_{SB} is the Stefan-Boltzmann constant. Figure 16 presents the calculated effective temperatures as a function of spectral type along with our best-fit polynomial relations for field and young (low gravity and YMG member) objects separately (Table 5). Our field relation is in good agreement with the corresponding field polynomial relation derived in Filippazzo et al. (2015). Figure 17 demonstrates the temperature evolution of ultracool dwarfs as a MKO NIR color-magnitude diagram for objects in our sample with derived fundamental parameters.

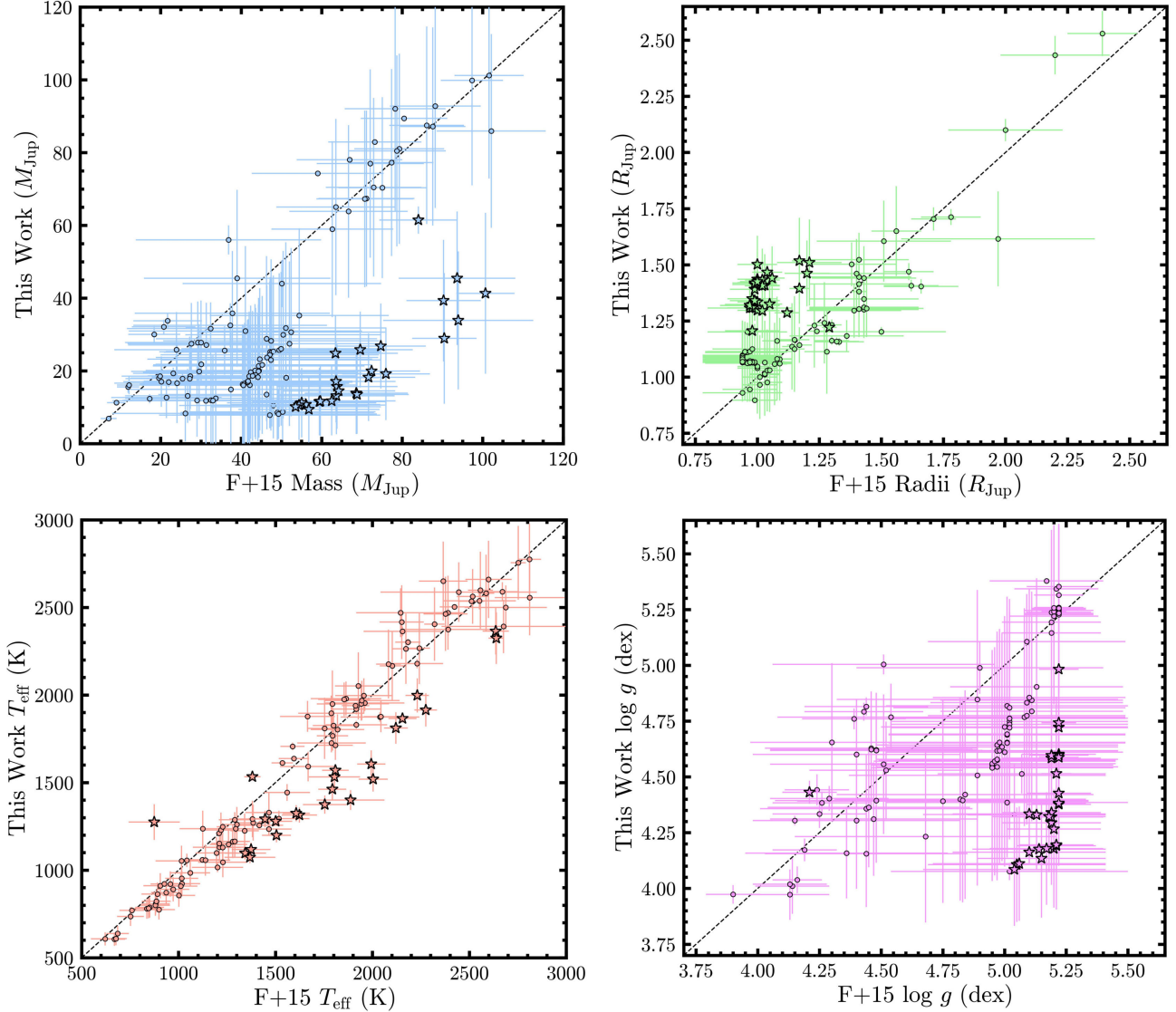


Figure 18. Comparison of mass, radius, effective temperature, and surface gravity derived in this work with those in Filippazzo et al. (2015, F+15) for objects common to the two samples. The dashed black line in each panel represents a 1:1 relation between the compared parameters. The parameters obtained are statistically consistent for the large majority of objects. Objects with disagreements ($>2\sigma$ discrepancy) in the estimated values are prominently marked with a black-bordered star.

7.3. Comparison with Filippazzo et al. (2015)

Figure 18 compares the masses, radii, effective temperatures, and surface gravities calculated in this work with those in Filippazzo et al. (2015). We find that our results are consistent ($<2\sigma$ difference) with Filippazzo et al. (2015) for the majority of objects ($N = 91$). $>2\sigma$ discrepancy in at least one of the above fundamental properties is observed for 37 objects (Figure 18). A complete list of the above objects is provided in Table 6.

The primary reason for the observed disagreements is a revision in the age distribution adopted for the objects. For field (FLD-G) objects, Filippazzo et al. (2015) adopt a uniform age distribution in the range 0.5–10.0 Gyr. We adopt

the (truncated) DL17 age distribution which skews towards younger ages: the greatest probability density in this age distribution lies in the 0.15–1 Gyr bin and the median age is ~ 2.5 Gyr. Consequently, our derived radii for these objects are generally larger, and our derived masses, temperatures, and gravities are generally smaller. This is the case for 22 out of the 37 discrepant objects. For 11 objects assigned a field age (0.5–10 Gyr) in Filippazzo et al. (2015), there have been updates to their YMG membership or spectroscopic gravity class. In this work, 2MASS J06244595-4521548, 2MASSW J0030300-145033, 2MASSI J0451009-340214, and DENIS-P J1058.7-1548 are designated as Argus members; 2MASSI J1010148-040649 is designated as a Carina-Near member; and LHS 3003 is designated as an

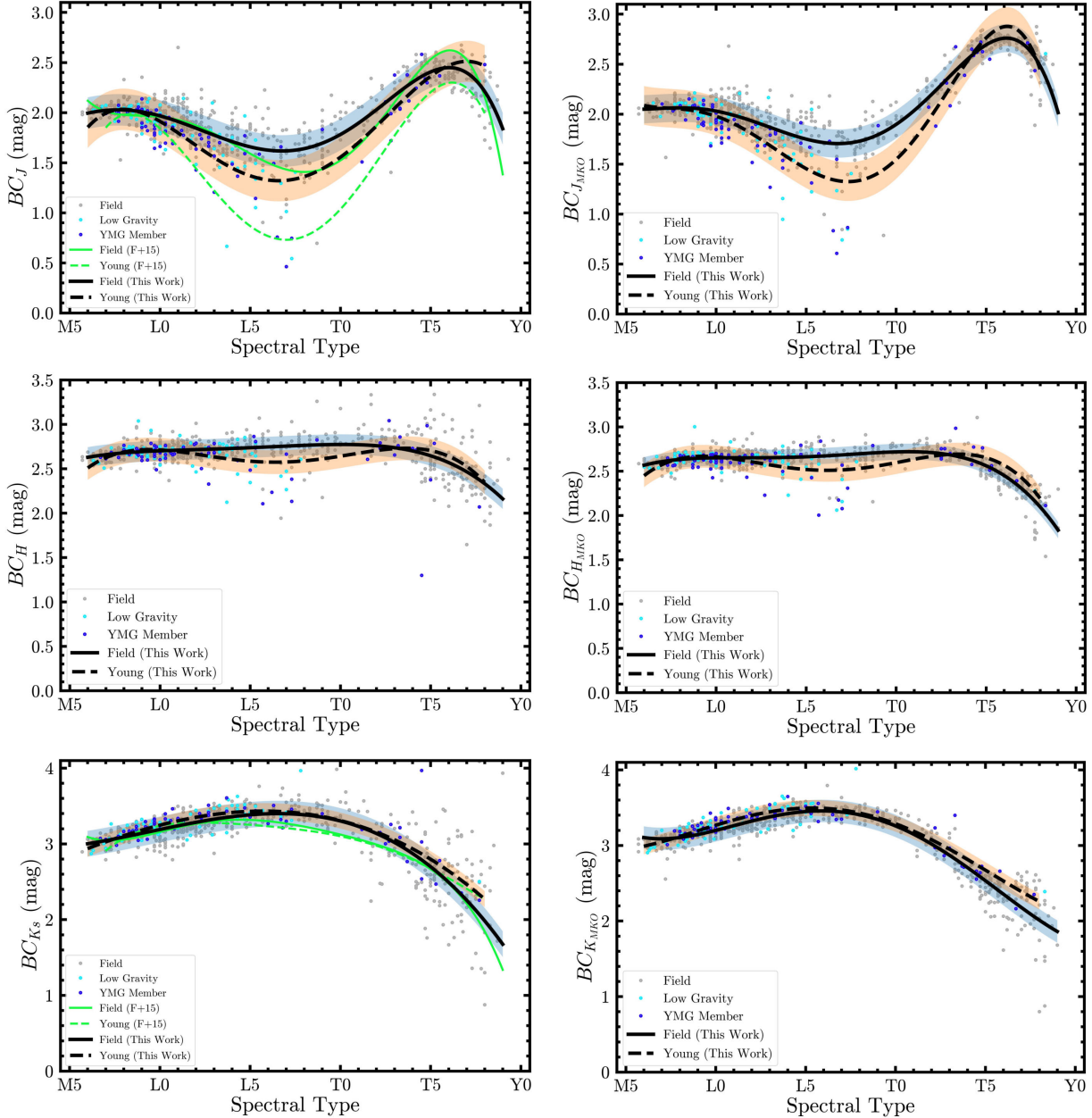


Figure 19. Bolometric corrections in the 2MASS and MKO near-IR bands for ultracool dwarfs in our sample as a function of spectral type (SpT). Random scatter in the x direction with amplitude 0.3 SpT is applied to avoid overlapping points. Symbols are the same as in Figure 11. Due to the large number of points, uncertainties in individual measurements are not shown for figure readability. The median uncertainty of measurements in each panel presented is 0.1 mag. The black solid and dashed lines are the best-fit polynomial relations for field and young objects, respectively. The blue and orange shaded regions are the rms scatter about the field and young object relations, respectively. The field and young object relations from Filippazzo et al. (2015) are plotted as green solid and dashed lines, respectively, for comparison.

AB Doradus member based on results from BANYAN Σ , 2MASS J13595510-4034582, DENIS-P J0652197-253450, and LHS 132 are assigned a β optical gravity classification, and 2MASSI J2057540-025230 and Teegarden’s Star are assigned an INT-G NIR gravity classification. Consequently, our derived masses, temperatures, and gravities for these objects are generally smaller, and our derived radii are gener-

ally larger. For 2 objects, 2MASS J03264225-2102057 and 2MASSW J2244316+204343, the YMG membership (AB Doradus) does not change but the source of our adopted ages differ. Filippazzo et al. (2015) use an age range of 50–120 Myr from Malo et al. (2013), whereas we use an older age of 149^{+51}_{-19} Myr from Bell et al. (2015). Consequently, our derived radii for these objects are generally smaller, and our

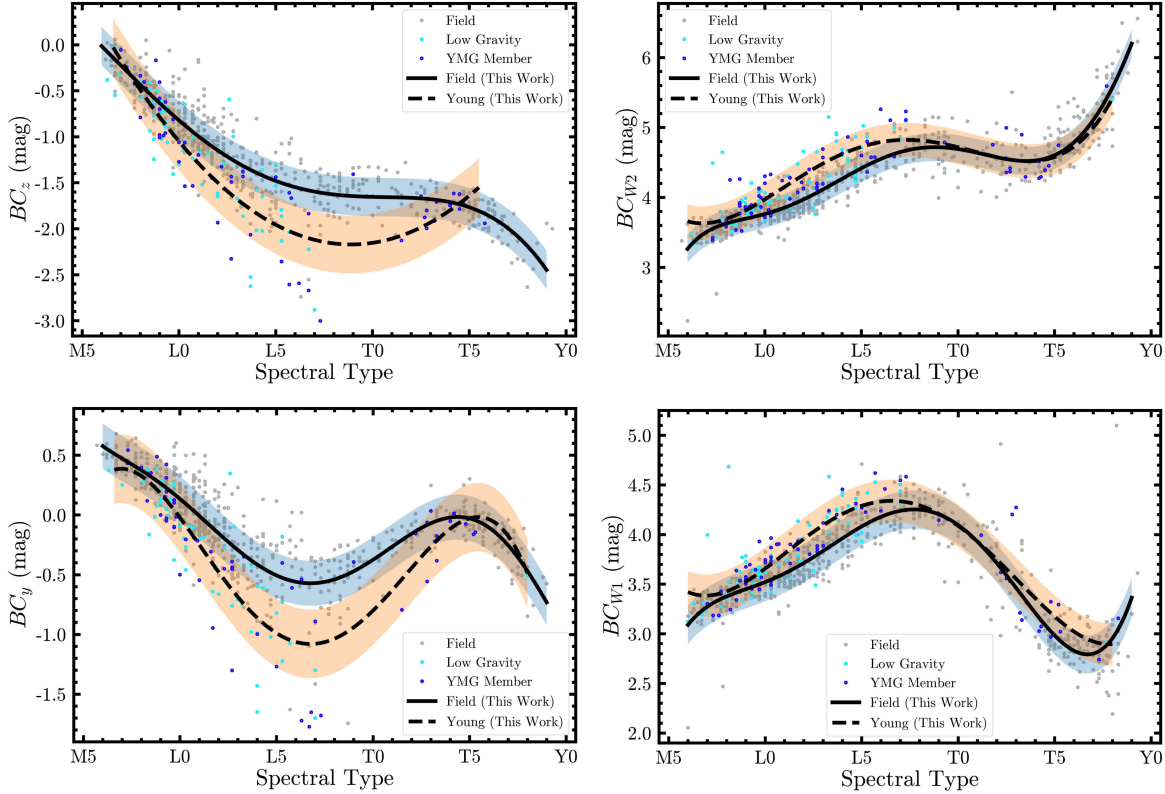


Figure 20. Bolometric corrections in the PS1 optical and WISE mid-infrared bands for ultracool dwarfs in our sample as a function of spectral type (SpT). Figure elements are same as in Figure 19. The median uncertainty of measurements in each panel presented is 0.1 mag.

derived masses, temperatures, and gravities for these objects are generally larger.

Two objects remain to be accounted for: 2MASSW J2208136+292121 and 2MASS J00332386-1521309. 2MASSW J2208136+292121 meets the consistency threshold for mass, radius, and gravity. We derive a lower effective temperature that is marginally inconsistent at the 2.1σ level. The age range adopted for this object is the same between Filippazzo et al. (2015) and this work. 2MASS J00332386-1521309 meets the consistency threshold for mass, radius, and gravity. The effective temperature is inconsistent at the 2.8σ level. Filippazzo et al. (2015) adopt an age range 100–150 Myr whereas we adopt a truncated DL17 age distribution (lower bound of 300 Myr) based on its FLD-G classification. This corresponds to an older age assignment compared to Filippazzo et al. (2015). However, our temperature estimate is lower than that of Filippazzo et al. (2015), not higher as it would be expected. These two disagreements arise because of the difference in bolometric luminosity measurements (due to changes in parallax measurement). Both objects can be found in Table 4. We measure lower bolometric luminosities for 2MASSW J2208136+292121 and 2MASS J00332386-1521309, which explain the lower effective temperatures derived for both objects.

More generally, the differences observed between our evolutionary model-derived parameter estimates and those in Filippazzo et al. (2015) may also be a result of the different estimation methods employed, as described in §7.1.

8. DISCUSSION

8.1. Bolometric Corrections

We calculate bolometric corrections spanning the optical to MIR filters for both field and young (low gravity and young moving group members) objects and determine empirical relationships as a function of spectral type following the process described in Section 5. For our calculations, we use $M_{bol,\odot} = 4.74$. We note here that the *F*-test does not always yield a definitive answer for the order of the polynomial based on the $p > 0.05$ rejection criterion. For such cases, we adopt the lowest order after which p does not change significantly (factor of $\sim 5\text{--}10$) as the best-fit polynomial, which is then validated by visual inspection. Figure 19 presents our bolometric corrections for the 2MASS and MKO NIR filters as a function of spectral type. Figure 20 presents our bolometric corrections for the PS1 z and y optical filters and the WISE W_1 and W_2 MIR filters as a function of spectral type. The derived polynomial relations are presented in Table 5.

Next, we discuss some key observations. First, based on the rms about the fit, the NIR relations generally show less

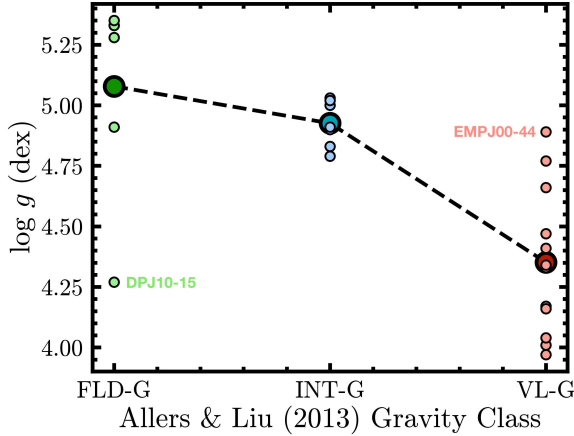


Figure 21. Evolutionary model-derived surface gravity distribution for different near-infrared gravity classifications. The smaller size markers represent individual object measurements and the larger size markers represent the mean surface gravity for a given gravity classification. DENIS-P J1058.7-1548 (DPJ10-15) and EROS-MP J0032-4405 (EMPJ00-44) are significant outliers. The median uncertainty of surface gravity measurements presented here is 0.04 dex. The black dashed line connects the mean surface gravities and serves as a visual aid to identify the trend. While individual groups exhibit varying levels of dispersion in their $\log g$ values, the index-based NIR gravity classification scheme accurately groups objects with systematic differences in their evolutionary model-derived surface gravities.

scatter than the optical and MIR relations and thus are preferable for bolometric magnitude calculations. Second, within the NIR relations, the bolometric corrections generally show smaller rms in the MKO filters than the 2MASS filters, likely due to the higher precision MKO photometry for T-dwarfs in the sample. Finally, we find that both the 2MASS K_S and MKO K -band bolometric corrections are relatively insensitive to the age of the ultracool dwarf and are thus most appropriate for cases when no age information is available.

We find a few significant differences in the 2MASS J and K_S polynomial relations on comparison with [Filippazzo et al. \(2015\)](#). Our field relation in the 2MASS J band predicts a higher bolometric correction (by $\approx 0.1 - 0.3$ mag) in the spectral range \sim L5–T2. The change can be attributed to the larger number of L/T transition objects in our work compared to [Filippazzo et al. \(2015\)](#). This enables a better constraint on the polynomial relation. The difference in the young object relations in the 2MASS J band is even more striking. Our best-fit polynomial predicts a bolometric correction up to ≈ 0.7 mag higher than that in [Filippazzo et al. \(2015\)](#) across spectral types \sim L2–T6. A careful comparison of Figure 12 in [Filippazzo et al. \(2015\)](#) with the top left panel of Figure 19 leads us to conclude that the larger number of young L2–L5 dwarfs with bolometric corrections > 1.5 mag serves to anchor our fit and is responsible for the differing solutions. However, in our measurements, we observe that the

bolometric corrections of young objects in the spectral range L5–L7 steeply drop to ≈ 1 mag, a feature not reproduced in our best-fit relation. This is also the case for our MKO J band young object relation. Our results suggest that a more appropriate empirical relationship may lie between the solutions found in [Filippazzo et al. \(2015\)](#) and this work or by adopting the direct averages as a function of spectral type. We note that the key to determining this will be adding more young objects in the range L7–T2, where, presently, there is a noticeable gap in our measurements. Until then, caution should be exercised in using the 2MASS and MKO J band young object relations at the L/T transition. The 2MASS K_S and MKO K -band young relations are more tightly constrained and are the recommended alternatives. Finally, in the 2MASS K_S band, we observe slight discrepancies between the field relations, within the calculated rms scatter, in the spectral range L5–T2. This can be similarly explained by the larger number of L/T transition object measurements in this work. The [Filippazzo et al. \(2015\)](#) 2MASS K_S band field relation diverges for T9 dwarfs compared to the one in this work and is likely an edge effect due to the small number of T9 objects in our sample.

8.2. Evolutionary Model-Derived Surface Gravity vs Ultracool Dwarf NIR Gravity Classifications

[Allers & Liu \(2013\)](#) defined a set of near-infrared gravity-sensitive indices based on FeH, VO, K I, Na I, and H-band continuum shape and created a gravity classification scheme consisting of three classes: FLD-G, INT-G, and VL-G. Here, we examine the empirical distribution of the evolutionary model-derived surface gravity of ultracool dwarfs as a function of their NIR gravity classifications. For an accurate analysis, we exclude ultracool dwarfs with spectra < 50 S/N in any of the following six bandpasses: $YJHK$ and two blue-half regions in the H and K bands (provided in the Table of Ultracool Fundamental Properties associated with this paper; see §1). We take care to only include low gravity objects for which the ages were determined based on the ages of their host stars or their membership to a YMG, independent of their NIR gravity classification. This was done to avoid circular logic in the analysis, since the assigned ages directly impact the estimation of surface gravities in our evolutionary model interpolation procedures. This results in 6 FLD-G, 7 INT-G, and 12 VL-G objects with evolutionary model-derived parameters from this work. These objects are plotted in Figure 21. We observe varying levels of scatter in the evolutionary model-derived surface gravity values for each gravity class — lowest for INT-G, followed by FLD-G, and highest for VL-G. The FLD-G outlier at $\log g = 4.27$ dex is DENIS-P J1058.7-1548, and the VL-G outlier at $\log g = 4.89$ dex is EROS-MP J0032-4405. DENIS-P J1058.7-1548 is a candidate Argus member (95% BANYAN- Σ prob-

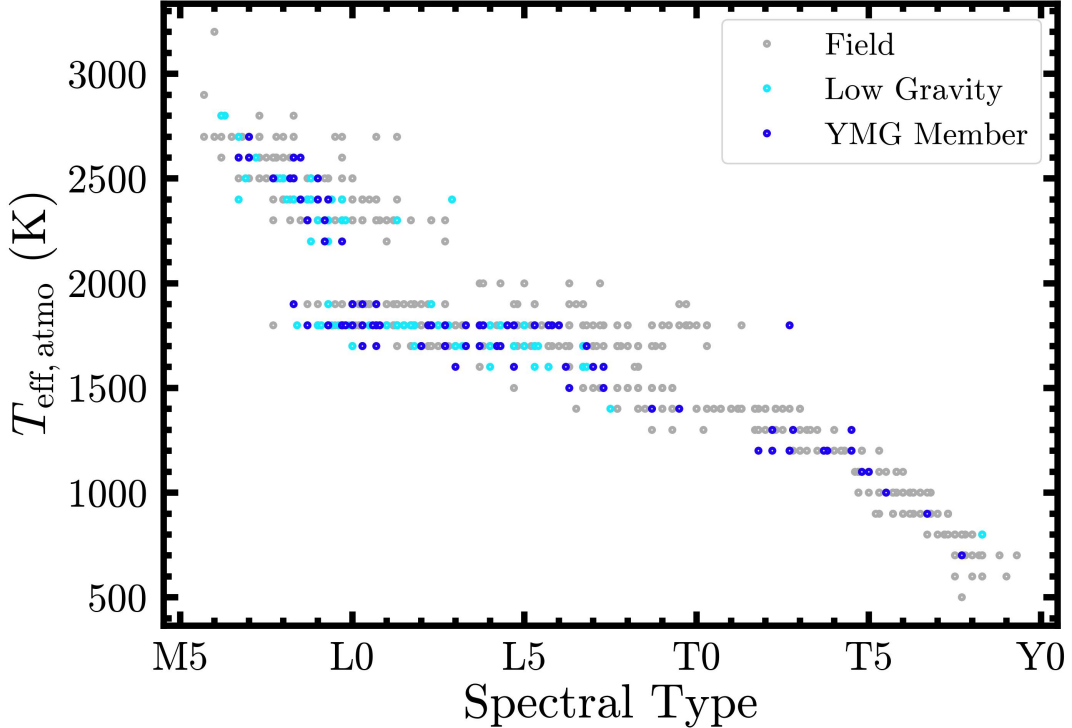


Figure 22. Atmospheric model-derived effective temperatures for objects in our sample as a function of spectral type. The symbols are similar to those described in Figure 16. A pile-up of objects at ≈ 1800 K creates two gaps at higher and lower effective temperatures.

ability) and was thus assigned an age of 45 ± 5 Myr. Such a young age is uncharacteristic for a FLD-G object and would explain the large discrepancy in $\log g$ from the FLD-G mean value. A comparison of DENIS-P J1058.7-1548's spectrum with L-dwarf FLD-G standards does not reveal any discrepancies that could suggest a gravity misclassification and thus it is probable that the YMG assignment is incorrect. EROS-MP J0032-4405 is an AB Doradus (AB Dor) Moving Group member. The INT-G classification is characteristic of AB Dor members (all 7 INT-G objects in our analysis are AB Dor members). Given that the derived surface gravity for this object is consistent with the mean surface gravity in the INT-G class, it may be possible that INT-G is a more suitable gravity classification for the object. However, the object also possesses an optical gravity classification of γ (Cruz et al. 2009), reducing the probability that a NIR gravity misclassification has occurred. We investigated the possibility that this object is a spectral blend using the spectral indices of Burgasser et al. (2010a) and Bardalez Gagliuffi et al. (2014), but found that none of the criteria for binarity were met. The relatively higher scatter in the FLD-G and VL-G classes may be an edge case artifact due to the limited number of classification groups and possibly highlights the need to add new gravity classes. This can be more reliably determined with a similar analysis consisting of a larger sample of objects. The primary factor limiting the sample size in this work is the lack of high S/N spectra (indicative of reliability of the

index-based gravity classification) across all the six wavelength regions defined previously. Nevertheless, the mean surface gravities exhibit a trend consistent with the gravity classification scheme — objects with a FLD-G classification, on average, have higher surface gravities than those with an INT-G classification which, in turn, have higher surface gravities, on average, than objects with a VL-G classification.

8.3. Differences between Atmospheric Model-derived and Evolutionary Model-derived Parameters

Numerous works in the past have documented discrepant $\log g$, T_{eff} , and thus radii values between those derived by fitting atmospheric models to substellar SEDs and those derived by interpolating evolutionary models (e.g. Liu et al. 2008; Dupuy et al. 2009; Bowler et al. 2010; Barman et al. 2011; Marley et al. 2012; Dupuy & Kraus 2013; Liu et al. 2013; Zhang et al. 2021c; Carter et al. 2022). Here, we take advantage of our large sample to study the noted differences as a function of spectral type and in the near-infrared color-magnitude diagram for ultracool dwarf effective temperatures, radii, and surface gravities.

8.3.1. Effective Temperature

First, we investigate the atmospheric model-derived effective temperatures ($T_{\text{eff,atmo}}$) vs spectral type relation and then systematically characterize the differences with evolutionary model-derived effective temperatures ($T_{\text{eff,evo}}$).

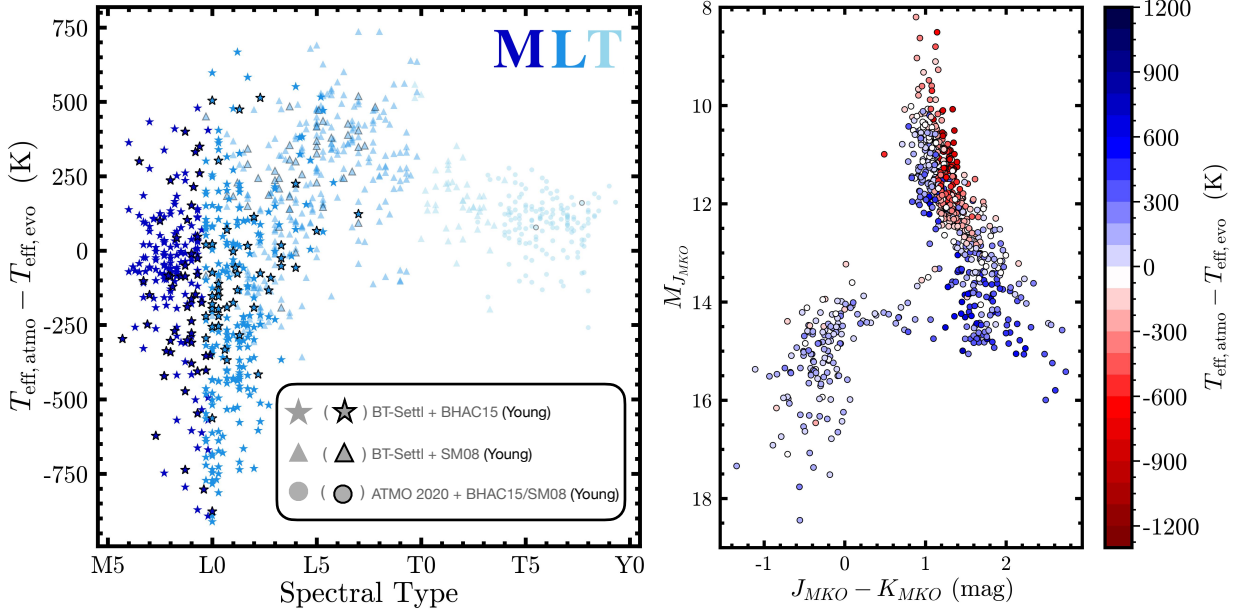


Figure 23. *Left:* Difference between the atmospheric model-derived effective temperatures and the evolutionary model-derived effective temperatures (ΔT_{eff}) as a function of spectral type (SpT). Random scatter in the x direction with amplitude 0.3 SpT is applied to avoid overlapping points. Objects are colored based on their spectral type where the darkest shade corresponds to M-dwarfs, the intermediate shade corresponds to L-dwarfs, and the lightest shade corresponds to T-dwarfs. Objects using the atmospheric-evolutionary model pairings of BT-SETTL—BHAC15, BT-SETTL—SM08, and ATMO 2020—BHAC15/SM08 are marked with a star, triangle, and circle respectively. BT-SETTL—BHAC15 objects are presented with a higher color opacity than BT-SETTL—SM08 and ATMO 2020—BHAC15/SM08 objects to emphasize the greater reliability of ΔT_{eff} trends for the former (self-consistently computed models). Symbols with black outlines mark young objects based on signatures of low surface gravity. *Right:* MKO M_J vs $J - K$ color-magnitude diagram for ultracool dwarfs in our sample with each object colored by its corresponding ΔT_{eff} value. Due to the large number of points, uncertainties in individual measurements are not shown for figure readability. The median uncertainty in $M_{J_{\text{MKO}}}$ is 0.06 mag and in $J - K$ is 0.05 mag.

Figure 22 shows $T_{\text{eff,atmo}}$ as a function of spectral type. A pile-up of objects in the temperature range ≈ 1700 - 1900 K is observed. This pile-up carves out gaps in the temperature sequence at ≈ 2000 - 2200 K and, less prominently, ≈ 1500 - 1600 K. Figure 23 investigates the effects of these features in greater detail by presenting the difference in $T_{\text{eff,atmo}}$ and $T_{\text{eff,evo}}$ measurements as a function of spectral type. A comparison between self-consistently computed atmospheric and evolutionary models is the most accurate choice for such an analysis. However, the availability of models only allows such a comparison for objects where we simultaneously employed the BT-SETTL and BHAC15 models (BT-SETTL—BHAC15). We find that late-M and early L-dwarfs ($\sim M6$ -L2) primarily constitute our sample for this analysis (Figure 23). Given that we do not observe a significant difference in the temperatures derived with BHAC15 vs SM08 (median difference ≈ 50 K; Figure 15), we are also able to perform plausible comparisons for the BT-SETTL—SM08 and ATMO 2020—BHAC15/SM08 pairings. $\sim L3$ -T2 dwarfs primarily form the sample for the former and $> T2$ dwarfs form the sample for the latter.

1. BT-SETTL—BHAC15 objects: In Figure 23, we find that BT-SETTL generally underestimates the effective

temperature compared to the BHAC15 evolutionary model, with the largest discrepancy (up to ≈ 800 K) at the M/L transition boundary. This discrepancy reflects the ≈ 1800 K pile-up of M/L transition objects in Figure 22 and the ≈ 2000 - 2200 K gap in the temperature sequence. Since cloud opacity increases as the effective temperature decreases across the M/L transition ultracool dwarfs, an underestimated effective temperature highlights that BT-SETTL does not incorporate sufficient dust in its ≈ 2000 - 2200 K models. Our results are in agreement with Hurt et al. (AAS Journals, submitted), where a ≈ 1800 K pile-up of objects was also identified in an analysis of the BT-SETTL model fitting results for 89 late-M and L benchmark dwarfs. They find that M/L transition objects are poorly fit by the BT-SETTL atmospheric models, which consistently overestimate the J and H band flux. By including an extinction component that follows the interstellar medium (ISM) reddening law, Hurt et al. (AAS Journals, submitted) find a significant improvement in the fits, similarly suggesting a lack of dust opacity in the BT-SETTL models in this regime.

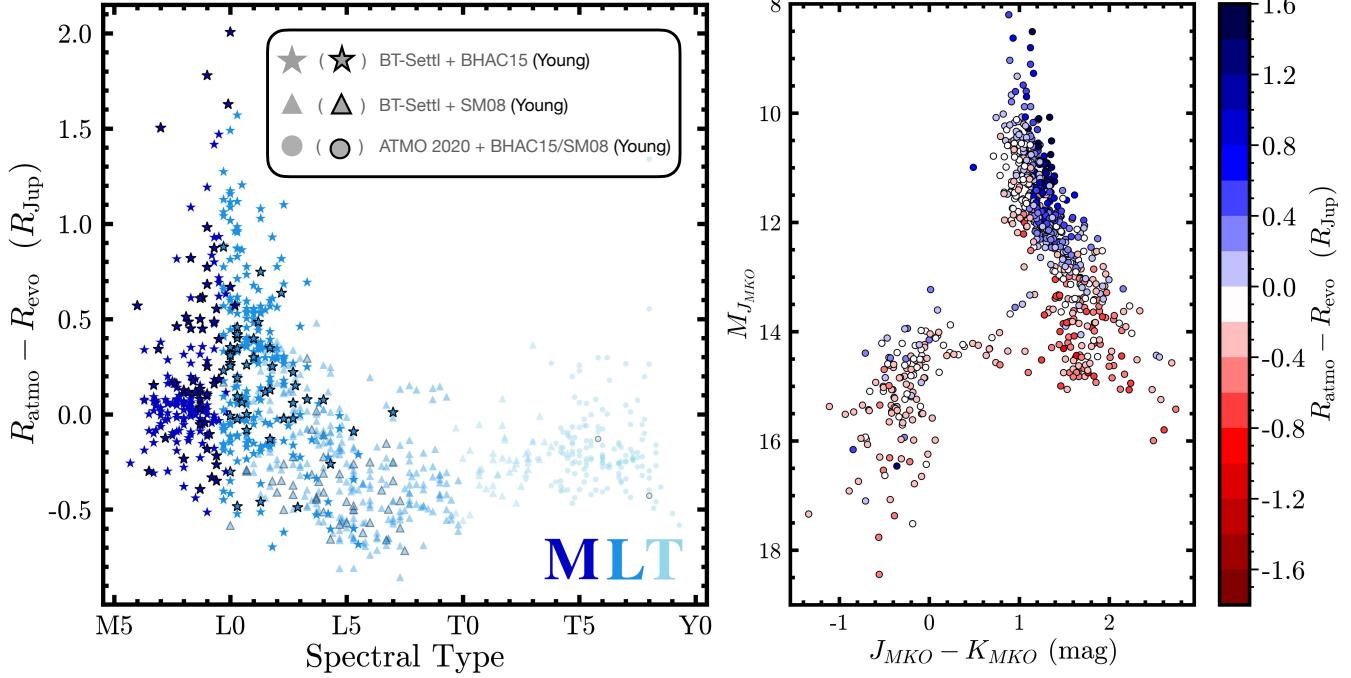


Figure 24. Same as Figure 23 but for difference between atmospheric and evolutionary model-derived radius measurements.

2. BT-SETTL-SM08 objects: In Figure 23, BT-SETTL generally yields consistent results with the SM08 evolutionary model for spectral types \sim L3–L5 but tends to overestimate the effective temperatures of late-L dwarfs. This discrepancy reflects the \approx 1800 K pile-up of late-L dwarfs in Figure 22 and possibly the less prominent \approx 1500–1600 K gap in the temperature sequence. Since cloud opacity increases from early-L to late-L dwarfs, an overestimated effective temperature for late-L dwarfs may mean that BT-SETTL over-predicts dust opacity in its \approx 1700–1800 K models.
3. ATMO 2020–BHAC15/SM08 objects: In Figure 23, we observe that ATMO 2020 tends to generally overestimate temperatures at a level of 100–200 K. This may indicate possible incompleteness in incorporating cloud-free opacity sources in the atmospheres of T-dwarfs.

It is important to note that a significant number of objects discussed in the second and third categories are located at the L/T transition. This is a relatively less understood phase of brown dwarf evolution. Since the comparison is not being conducted for self-consistently computed models, the discrepancies seen could be attributed to reasons outside the scope of our investigation. As such, one should be cautious in definitively interpreting BT-SETTL-SM08 and ATMO 2020–BHAC15/SM08 object results. Combining SED-integrated bolometric luminosities with direct radius measurements of ultracool dwarfs would allow strictly empirical tests of the systematics in both atmospheric and evo-

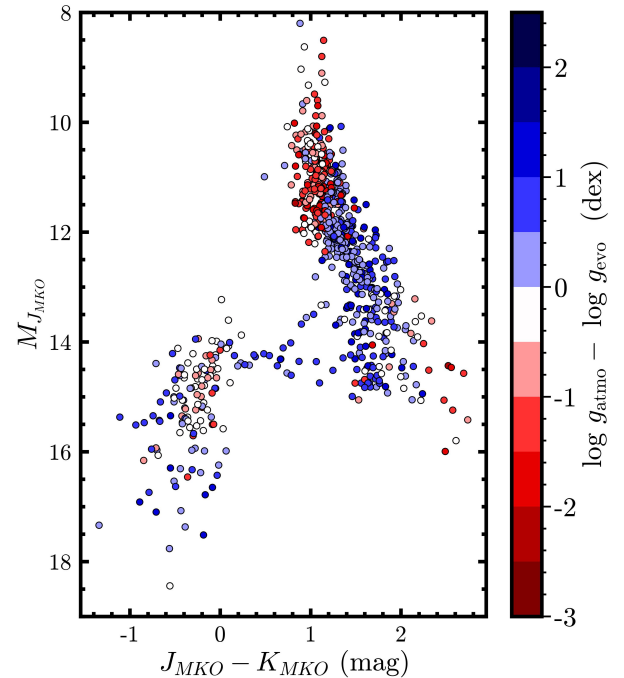


Figure 25. Same as right panel of Figure 23 but for difference between atmospheric and evolutionary model-derived surface gravity measurements.

lutionary models. A summary of our results is presented as a MKO M_J vs $J - K$ color-magnitude diagram in the right panel of Figure 23.

8.3.2. Radius and Surface Gravity

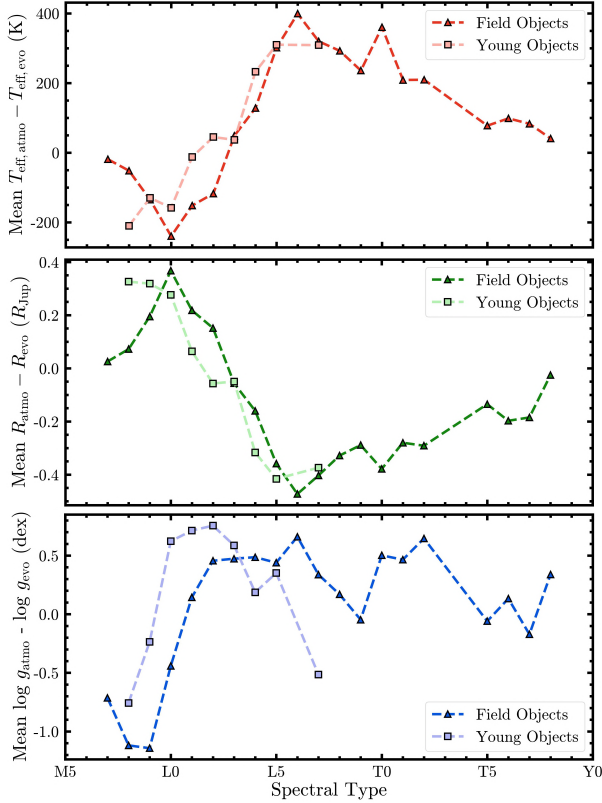


Figure 26. Average difference between the atmospheric and evolutionary model-derived effective temperatures (top), radii (middle), and surface gravities (bottom) as a function of spectral type for field (triangles) and young (squares) objects. Spectral types with <10 field objects (M6, T4, T9) and <5 young objects (M6, M7, L6, $\geq L8$) in our sample have been skipped. There was no significant difference between the mean and the median parameter difference distributions as a function of spectral type. Such systematic offsets may be adopted when combining fundamental parameter estimates obtained with the two methods.

Here, we note the observed differences between atmospheric and evolutionary model-derived radii and surface gravities for our sample of ultracool dwarfs. The analysis is conducted similar to §8.3.1.

The atmospheric model-derived radius R_{atmo} is obtained from the scale factor Ω of the best-fit model spectrum as,

$$R_{\text{atmo}} = \sqrt{\Omega \cdot d^2}, \quad (12)$$

where d is the object's distance. Figure 24 shows the difference between the two sets of radii measurements as a function of spectral type. For BT-SETTL—BHAC15 objects, which lie at the M/L transition boundary, radius is significantly overestimated by BT-SETTL (up to $1.5 R_{\text{Jup}}$). For BT-SETTL—SM08 and ATMO 2020—BHAC15/SM08 objects ($\gtrsim L3$), atmospheric models underestimate the radius by ≈ 0.1 – $0.7 R_{\text{Jup}}$, with maximum discrepancy in the late-L spectral types. A summary of these results is presented as a MKO M_J vs $J - K$ color-magnitude diagram in the right

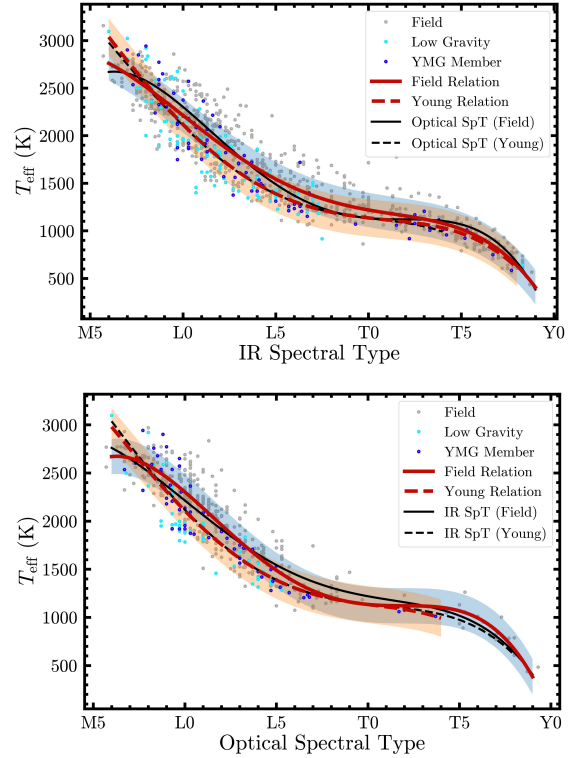


Figure 27. Effective temperatures derived for objects in our sample as a function of infrared (top) and optical (bottom) spectral types (SpTs). Random scatter in the x direction with amplitude 0.3 SpT is applied to avoid overlapping points. The figure elements are similar to those described in Figure 16. In each panel, the best-fit polynomial relation for field and young objects from the other panel is presented as a dashed line of the same color as in the other panel.

panel of Figure 24. Finally, Figure 25 presents the trend in $\log g$ differences as a MKO M_J vs $J - K$ color-magnitude diagram. Atmospheric models underestimate the gravities of bluer M/L transition dwarfs by up to 2 dex but overestimate the gravities of redder M/L transition dwarfs by ≈ 0.5 dex. No systematic trend is observed for later type objects in the color-magnitude diagram.

8.4. Characterization of Systematic Offsets

The significant discrepancies observed in the fundamental parameters obtained from evolutionary and atmospheric models raise questions about the reliability of either method to accurately estimate ultracool dwarf fundamental parameters. Past work on this topic has indicated that atmospheric models are more likely to be the source of the discrepancy: they are sensitive to boundary conditions unlike evolutionary models, involve many uncertain parameters in the modeling inputs and prescriptions, and often yield unphysical parameter estimates (e.g., Chabrier et al. 2000; Dupuy et al. 2009, 2010; Liu et al. 2010; Barman et al. 2011; Dupuy & Liu 2017). It has been suggested that a systematic offset may ex-

ist between atmospheric and evolutionary model-derived parameters. Previously, the characterization of such systematic offsets has been limited to small samples of objects. Here, we take advantage of our large sample size to derive the average systematic offset in effective temperature, radius, and surface gravity as a function of spectral type for field and young objects. We compute the mean of the differences between atmospheric and evolutionary model-derived parameter values ($\Delta P = P_{\text{atmo}} - P_{\text{evo}}$, where P is the relevant fundamental parameter) for each spectral type. We skip spectral types with <10 field objects (M6, T4, T9) and spectral types with <5 young objects (M6, M7, L6, \geq L8) in our sample. Figure 26 presents our results. The average systematic offsets are as large as 400 K in effective temperature, $0.4 R_{\text{Jup}}$ in radius, and 1.2 dex in $\log g$. Larger systematic offsets are generally found near the M/L and L/T transition regions. Such systematic offsets might be adopted when combining fundamental parameter estimates obtained with the two methods.

8.5. Optical and Near-Infrared Spectral Type- T_{eff} Sequences and Comparison

We present T_{eff} sequences as a function of optical and IR spectral types in Figure 27 and the corresponding best-fit polynomial relations for field and young objects in Table 5. Nearly two times as many objects have IR spectral types in our sample as optical spectral types. We observe that the T_{eff} sequence has a marginally lower rms about the best-fit as a function of IR spectral type, for field objects, compared to optical spectral types. While the relations for both spectral classifications are consistent, the optical spectral type is observed to predict slightly lower temperatures in the L/T transition for field objects compared to the IR spectral type and marginally higher temperatures for late-T field-age objects. We conclude that both spectral-typing schemes are good indicators of T_{eff} across the complete ultracool dwarf spectral sequence, given the availability of age information.

9. CONCLUSION

In this work, we performed a uniform calculation of the fundamental physical properties of 1054 ultracool dwarfs using the most precise photometry and astrometry available to date from *The UltracoolSheet* (version 2.0.0, in preparation). Our results are summarized below:

1. We obtained new low-resolution near-IR spectroscopy for 97 objects in our sample using NASA/IRTF. These spectra were collected for the spectroscopic characterization of known objects (57 potential low-gravity sources, benchmark objects, and wide companions) or the discovery of new ultracool dwarfs (40 objects). Additionally, we obtained new parallaxes for 19 objects using CFHT/WIRCam (11 sources) and Pan-STARRS 1 (8 sources).

2. We have derived the bolometric luminosities (L_{bol}) of 865 field-age and 189 young ultracool dwarfs by assembling and directly integrating flux-calibrated optical to mid-IR SEDs consisting of low-resolution ($R \sim 150$) near-IR (0.85–2.5 μm) NASA/IRTF SpeX prism spectra, optical photometry from the Pan-STARRS1 survey, and mid-IR photometry from the CatWISE2020 survey and Spitzer/IRAC. Flux contributions from the optical (0.2–0.85 μm) and mid-IR (2.5–2000.0 μm) wavelengths were estimated using the best-fit BT-SETTL or ATMO 2020 atmospheric model spectrum to the SED.
3. A careful treatment of uncertainties revealed the presence of a noise floor in our L_{bol} measurements at the ≈ 0.015 dex level due to the use of atmospheric models to estimate flux contribution from wavelengths outside our SpeX spectra. This highlighted that high precision parallaxes must be paired with improved spectral coverage in the optical and mid-IR wavelengths to further drive the uncertainty in L_{bol} lower. Overall, the median uncertainty in our L_{bol} measurements was 0.05 dex.
4. Using the derived L_{bol} values and a new uniform age analysis for all objects in our sample, combined with the BHAC15 and SM08 evolutionary models, we estimated ultracool dwarf masses, radii, and surface gravities by employing Bayesian rejection sampling. Our L_{bol} measurements and evolutionary model-derived radii enabled the determination of semi-empirical effective temperatures (T_{eff}), with a median uncertainty of 98 K.
5. We showed that our L_{bol} measurements and evolutionary model-derived fundamental parameter estimates are largely consistent with those from Filippenazzo et al. (2015), for objects common to the two samples ($N = 130$). For a small subset of these objects, revisions to their parallaxes and age distributions primarily contributed to the discrepancies observed in their L_{bol} measurements and the evolutionary model-derived fundamental parameter estimates, respectively.
6. Our large sample enabled us to establish empirical relationships for L_{bol} as a function of absolute magnitude, and L_{bol} , T_{eff} , and bolometric correction in various photometric bands as a function of spectral type, for both field-age and young objects. Based on the low rms scatter about the fit and relative insensitivity to age, we recommended the use of the MKO H -band polynomial relation for L_{bol} calculations from absolute magnitude. Further, we found that the 2MASS K_S -band or MKO K -band polynomial relations are

- the preferred choice for bolometric correction calculations from spectral type.
7. We performed a comparison between the evolutionary model-derived surface gravities and near-infrared gravity classifications of ultracool dwarfs for a carefully constructed sample of young moving group members and companion objects. While the surface gravity measurements exhibited scatter in each of the three categories (FLD-G , INT-G , and VL-G), we observed a systematic difference in the mean surface gravities between the three gravity classes.
 8. A detailed characterization of atmospheric model systematics as a function of spectral type and in the near-infrared color magnitude diagram, based on comparisons with evolutionary model-derived values, revealed significantly large discrepancies in the effective temperatures (up to 800 K), radii (up to $2.0 R_{\text{Jup}}$), and surface gravities (up to 2 dex) of M/L transition dwarfs. Our results suggested that BT-SETTL lacks sufficient dust opacity in its models, in this regime. Based on this comparative analysis, we provided average systematic offsets between atmospheric and evolutionary model-derived T_{eff} , radii, and $\log g$ as a function of spectral type for field and young objects. These systematic offsets might be adopted when combining fundamental parameter estimates obtained with the two methods.

The large-scale compilation of ultracool dwarf fundamental physical parameters presented in this work represents a factor of ~ 5 increase in the sample size of such semi-empirical measurements compared to previous work. Determining the ages of ultracool dwarf binaries (e.g. Dupuy et al. 2023), calculating the radii of candidate transiting planets (e.g. Tamburo et al. 2022), and constructing luminosity distributions to constrain the substellar initial mass function (e.g. Kirkpatrick et al. 2021) are just a few of the many exciting applications of this work as we continue to explore the fascinating diversity of substellar objects and companions.

ACKNOWLEDGMENTS

The authors would like to thank the anonymous referee for many helpful comments which improved the manuscript. We also thank Aaron Meisner and Adam Schneider for helpful discussions on cross-matching ALLWISE sources with CatWISE2020 sources. This work has benefitted from *The UltracoolSheet*, maintained by Will Best, Trent Dupuy, Michael Liu, Aniket Sanghi, Rob Siverd, and Zhoujian Zhang, and developed from compilations by Dupuy & Liu (2012), Dupuy & Kraus (2013), Liu et al. (2016), Best et al. (2018), Best et al. (2020), and Schneider et al. (2023). The data presented herein were obtained at the W. M. Keck Observatory, which is operated as a scientific partnership among the

California Institute of Technology, the University of California, and the National Aeronautics and Space Administration (NASA). The Observatory was made possible by the generous financial support of the W. M. Keck Foundation. The authors wish to recognize and acknowledge the very significant cultural role and reverence that the summit of Maunakea has always had within the indigenous Hawaiian community. We are most fortunate to have the opportunity to conduct observations from this mountain.

A. Sanghi acknowledges support from Research Experience for Undergraduate program at the Institute for Astronomy, University of Hawaii-Manoa funded through National Science Foundation (NSF) grant #2050710. A. Sanghi would like to thank the Institute for Astronomy for their hospitality during the course of this project. This research was funded in part by the Gordon and Betty Moore Foundation through grant GBMF8550 to M. Liu. W.M.J. Best acknowledges support from grant HST-GO-15238 provided by STScI and AURA. T. Dupuy acknowledges support from UKRI STFC AGP grant ST/W001209/1. For the purpose of open access, the author has applied a Creative Commons Attribution (CC BY) licence to any Author Accepted Manuscript version arising from this submission.

This publication makes use of data products from: the *Two Micron All Sky Survey* (2MASS), which is a joint project of the University of Massachusetts and the Infrared Processing and Analysis Center/California Institute of Technology, funded by the National Aeronautics and Space Administration and the National Science Foundation; the UKIRT Infrared Deep Sky Survey (UKIDSS) project, which is defined in Lawrence et al. (2007), uses the UKIRT Wide Field Camera (WFCAM: Casali et al. 2007) and a photometric system described in Hewett et al. (2006), and the pipeline and science archives described in Irwin (2008) and Hambly et al. (2008); the *Wide-field Infrared Survey Explorer* (WISE), which is a joint project of the University of California, Los Angeles, and the Jet Propulsion Laboratory/California Institute of Technology, funded by the National Aeronautics and Space Administration; the SIMBAD database, Aladin, and Vizier, operated at CDS, Strasbourg, France; the SpeX prism Spectral Libraries, maintained by Adam Burgasser; the NASA/IPAC Infrared Science Archive, which is operated by the Jet Propulsion Laboratory, California Institute of Technology, under contract with the National Aeronautics and Space Administration; the Spanish Virtual Observatory (<https://svo.cab.inta-csic.es>) project funded by MCIN/AEI/10.13039/501100011033/ through grant PID2020-112949GB-I00.

Additional Software/Resources: ASTROPY (Astropy Collaboration et al. 2013, 2018; The Astropy Collaboration et al. 2022), MATPLOTLIB (Hunter 2007), NUMPY (Harris et al. 2020), SCIPY (Virtanen et al. 2020), PANDAS (Reback et al.

2022) and the NASA Astrophysics Data System (ADS). The data presented in this work are made publicly available at <https://doi.org/10.5281/zenodo.8315643>. The scripts associ-

ated with the methods in this work are made publicly available at [https://github.com/cosmiccoder/HIPPVI-Code](https://github.com/cosmicoder/HIPPVI-Code).

Table 5. Polynomial Relations

$P(x)^a$	x^b	rms	c_0	c_1	c_2	c_3	c_4	c_5	c_6
$L_{\text{bol, FLD}}$	$6.0 \leq \text{SpT} \leq 29.0$	0.157 dex	$2.38575339e+00$	$-2.34765187e+00$	$4.10403429e-01$	$-3.75870300e-02$	$1.79418353e-03$	$-4.22643837e-05$	$3.85072198e-07$
$T_{\text{eff, FLD}}$	$6.0 \leq \text{SpT} \leq 29.0$	174.686 K	$1.5870384e+03$	$5.52980543e+02$	$-7.99773680e+01$	$3.71753828e+00$	$-5.75357642e-02$
$T_{\text{eff, YNG}}$	$6.0 \leq \text{SpT} \leq 28.0$	188.424 K	$4.56313932e+03$	$-2.28258451e+02$	$-1.11940923e+01$	$1.17847855e+00$	$-2.38265571e-02$
$T_{\text{eff, FLD}}$	$6.0 \leq \text{Optical SpT} \leq 29.0$	183.423 K	$2.8921204e+02$	$9.22014212e+02$	$-1.15315067e+02$	$5.08274865e+00$	$-7.58233882e-02$
$T_{\text{eff, YNG}}$	$6.0 \leq \text{Optical SpT} \leq 24.0$	191.954 K	$4.07702266e+03$	$-8.43172747e+01$	$-2.63589282e+01$	$1.85751341e+00$	$-3.48367787e-02$
$T_{\text{eff, FLD}}$	$6.0 \leq \text{IR SpT} \leq 29.0$	180.226 K	$2.44117451e+03$	$2.80510088e+02$	$-5.16856405e+01$	$2.34129573e+00$	$-4.05522698e-02$
$T_{\text{eff, YNG}}$	$6.0 \leq \text{IR SpT} \leq 28.0$	195.565 K	$4.47499244e+03$	$-1.87857056e+02$	$-1.60621537e+01$	$1.40051083e+00$	$-2.72611817e-02$
$BC_z \text{ FLD}$	$6.0 \leq \text{SpT} \leq 29.0$	0.208 mag	$8.82748312e-01$	$-3.28812471e-02$	$-3.01625334e-02$	$2.00785031e-03$	$-3.67327336e-05$
$BC_y \text{ FLD}$	$6.0 \leq \text{SpT} \leq 29.0$	0.189 mag	$4.78290771e+00$	$-2.0507405e+00$	$4.09934609e-01$	$-4.22427931e-02$	$2.21923901e-03$	$-5.63234268e-05$	$5.46529690e-07$
$BC_J \text{ FLD}$	$6.0 \leq \text{SpT} \leq 29.0$	0.157 mag	$1.83270671e+00$	$-1.00428444e-01$	$4.91437247e-02$	$-6.23850138e-03$	$2.91250402e-04$	$-4.4978717e-06$...
$EC_{JMKO} \text{ FLD}$	$6.0 \leq \text{SpT} \leq 29.0$	0.141 mag	$3.34867561e+00$	$-7.05942778e-01$	$1.41154739e-01$	$-1.27017514e-02$	$5.03938151e-04$	$-7.12860970e-06$...
$BC_H \text{ FLD}$	$6.0 \leq \text{SpT} \leq 29.0$	0.114 mag	$2.06836504e+00$	$1.78079042e-01$	$-1.90813876e-02$	$9.23336345e-04$	$-1.63236829e-05$
$BC_{HMKO} \text{ FLD}$	$6.0 \leq \text{SpT} \leq 29.0$	0.091 mag	$1.60830399e+00$	$3.16405418e-01$	$-3.511960013e-02$	$1.68671698e-03$	$-2.89674748e-05$
$BC_{Ks} \text{ FLD}$	$6.0 \leq \text{SpT} \leq 29.0$	0.169 mag	$2.96143878e+00$	$-3.73942004e-02$	$9.29897400e-03$	$-3.28966542e-04$
$BC_{KMKO} \text{ FLD}$	$6.0 \leq \text{SpT} \leq 29.0$	0.148 mag	$4.56079546e+00$	$-5.30973644e-01$	$6.31017198e-02$	$-2.75558092e-03$	$3.72518239e-05$
$BC_{W1} \text{ FLD}$	$6.0 \leq \text{SpT} \leq 29.0$	0.193 mag	$-5.362285544e+00$	$3.60059733e+00$	$-5.96094136e-01$	$4.92274677e-02$	$-2.05225834e-03$	$3.99592136e-05$	$-2.7443149e-07$
$BC_{W2} \text{ FLD}$	$6.0 \leq \text{SpT} \leq 29.0$	0.198 mag	$-1.07410524e+01$	$6.19843221e+00$	$-1.07147549e+00$	$9.35831952e-02$	$-4.27523017e-03$	$9.68864595e-05$	$-8.55309439e-07$
$BC_z \text{ YNG}$	$6.6 \leq \text{SpT} \leq 25.5$	0.314 mag	$2.88963400e+00$	$-5.35800318e-01$	$1.41810437e-02$
$BC_y \text{ YNG}$	$6.6 \leq \text{SpT} \leq 28.0$	0.287 mag	$-5.21677358e+00$	$2.03998815e+00$	$-2.47492191e-01$	$1.12619606e-02$	$-1.71769287e-04$
$BC_J \text{ YNG}$	$6.0 \leq \text{SpT} \leq 28.0$	0.206 mag	$-2.92269209e+00$	$1.62463279e+00$	$-1.80923490e-01$	$7.81791312e-03$	$-1.13687590e-04$
$BC_{JMKO} \text{ YNG}$	$6.0 \leq \text{SpT} \leq 28.0$	0.193 mag	$5.27987592e+00$	$-1.54348126e+00$	$2.82107387e-01$	$-2.39608174e-02$	$9.14238336e-04$	$-1.25936127e-05$...
$BC_H \text{ YNG}$	$6.0 \leq \text{SpT} \leq 28.0$	0.134 mag	$-1.33267424e-01$	$8.47857406e-01$	$-8.88312926e-02$	$3.83044799e-03$	$-5.80866653e-05$
$BC_{HMKO} \text{ YNG}$	$6.0 \leq \text{SpT} \leq 28.0$	0.129 mag	$-5.08204516e-01$	$9.56683399e-01$	$-1.01434926e-01$	$4.42442275e-03$	$-6.78222163e-05$
$BC_{Ks} \text{ YNG}$	$6.0 \leq \text{SpT} \leq 28.0$	0.106 mag	$2.30496939e+00$	$1.15457026e-01$	$-1.02256113e-03$	$-1.12479204e-04$
$BC_{HMKO} \text{ YNG}$	$6.0 \leq \text{SpT} \leq 28.0$	0.106 mag	$3.23630807e+00$	$-1.84769176e-01$	$3.30808101e-02$	$-1.67472629e-03$	$2.44417318e-05$
$BC_{W1} \text{ YNG}$	$6.0 \leq \text{SpT} \leq 28.0$	0.212 mag	$6.86131158e+00$	$-1.26576300e+00$	$1.52614866e-01$	$-6.80445371e-03$	$9.95645299e-05$
$BC_{W2} \text{ YNG}$	$6.0 \leq \text{SpT} \leq 28.0$	0.241 mag	$7.50713316e+00$	$-1.44635248e+00$	$1.79292891e-01$	$-8.30663097e-03$	$1.30461556e-04$
$L_{\text{bol, FLD, ML}}^c$	$9.1 \leq M_J \leq 16.1$	0.057 dex	$5.533401206e-01$	$-3.511344336e-01$
$L_{\text{bol, FLD, ML}}^c$	$12.8 \leq M_J \leq 18.4$	0.101 dex	$8.80288566e-01$	$-3.93121219e-01$
$L_{\text{bol, FLD}}^c$	$8.5 \leq M_H \leq 18.1$	0.066 dex	$6.93323688e-01$	$-3.89636901e-01$
$L_{\text{bol, FLD}}^c$	$7.3 \leq M_{Ks} \leq 18.5$	0.083 dex	$-2.50181488e+01$	$8.16617507e+00$	$-1.04402978e+00$	$5.48196484e-02$	$-1.04209064e-03$
$L_{\text{bol, FLD, ML}}^c$	$9.0 \leq M_{JMKO} \leq 16.0$	0.055 dex	$6.003434959e-01$	$-3.57204309e-01$
$L_{\text{bol, FLD, T}}^c$	$12.6 \leq M_{JMKO} \leq 18.4$	0.108 dex	$9.54337740e-01$	$-4.04863108e-01$
$L_{\text{bol, FLD}}^c$	$8.5 \leq M_{HMKO} \leq 18.8$	0.053 dex	$6.17668495e-01$	$-3.89097000e-01$
$L_{\text{bol, FLD}}^c$	$8.1 \leq M_{KKMO} \leq 19.0$	0.064 dex	$-8.68942422e+00$	$3.1747734e+00$	$-4.83389959e-01$	$2.73739037e-02$	$-5.47040525e-04$
$L_{\text{bol, FLD}}^c$	$11.0 \leq M_z \leq 22.7$	0.083 dex	$8.78235147e-01$	$-3.06670163e-01$
$L_{\text{bol, FLD, ML}}^c$	$10.5 \leq M_y \leq 18.5$	0.074 dex	$5.55740568e-01$	$-3.03933139e-01$
$L_{\text{bol, FLD, T}}^c$	$15.0 \leq M_y \leq 21.0$	0.066 dex	$1.37035364e+00$	$-3.66205917e-01$

Table 5 *continued*

Table 5 (continued)

$P(x)^a$	x^b	rms	c_0	c_1	c_2	c_3	c_4	c_5	c_6
$L_{\text{bol FLD}}$	$7.6 \leq M_{W1} \leq 17.1$	0.103 dex	-5.22934625e+01	1.85121627e+01	-2.47203555e+00	1.3959009e-01	-2.87497133e-03
$L_{\text{bol FLD}}$	$7.3 \leq M_{W2} \leq 14.1$	0.125 dex	1.75395276e+00	-5.42818335e-01
$L_{\text{bol YNG ML}}^c$	$8.2 \leq M_J \leq 15.8$	0.081 dex	4.08756088e-01	-3.34689569e-01
$L_{\text{bol YNG T}}^c$	$14.1 \leq M_J \leq 16.7$	0.108 dex	9.53221827e-01	-3.9259421e-01
$L_{\text{bol YNG}}$	$7.7 \leq M_H \leq 17.0$	0.072 dex	6.58328628e-01	-3.84611365e-01
$L_{\text{bol YNG ML}}^c$	$7.3 \leq M_{Ks} \leq 16.8$	0.057 dex	-1.68245519e+01	5.94124964e+00	-8.33426219e-01	4.68755666e-02	-9.51087115e-04
$L_{\text{bol YNG ML}}^c$	$8.2 \leq M_{JMKO} \leq 15.8$	0.080 dex	4.06864509e-01	-3.36361777e-01
$L_{\text{bol YNG T}}^c$	$14.0 \leq M_{JMKO} \leq 16.7$	0.097 dex	8.31005313e-01	-3.94047446e-01
$L_{\text{bol YNG}}$	$7.7 \leq M_{HMKO} \leq 17.0$	0.057 dex	7.25956089e-01	-3.88884874e-01
$L_{\text{bol YNG}}$	$7.3 \leq MKMKO \leq 16.7$	0.057 dex	-2.06743904e+01	7.40114284e+00	-1.03611814e+00	5.90347236e-02	-1.21640941e-03
$L_{\text{bol YNG}}$	$11.0 \leq M_z \leq 19.3$	0.121 dex	6.92111297e-01	-2.88226403e-01
$L_{\text{bol YNG ML}}^c$	$10.3 \leq M_y \leq 17.8$	0.104 dex	3.28920351e-01	-2.80644117e-01
$L_{\text{bol YNG T}}^c$	$16.5 \leq M_y \leq 19.5$	0.075 dex	7.09044657e-01	-3.25773704e-01
$L_{\text{bol YNG}}$	$6.6 \leq M_{W1} \leq 16.1$	0.116 dex	-3.70291470e+01	1.38286472e+01	-1.95883111e+00	1.15867819e-01	-2.48769429e-03
$L_{\text{bol YNG}}$	$6.1 \leq M_{W2} \leq 13.6$	0.158 dex	1.05360011e+00	-4.84834949e-01

NOTE—Caution should be exercised in using the 2MASS and MKO J band young object relations at the L/T transition as discussed in §8.1. Since we exclude objects in star-forming regions from our sample, the YNG relations (calculated for YMG members and low gravity sources) are not appropriate for objects with ages ≤ 10 Myr.

$$a P(x) = \sum_{i=0}^n c_i x^i$$

b Polynomials expressed as a function of spectral type (SpT) accept inputs in the range 6–29 corresponding to spectral types M6–T9.

c The subscripts ML and T designate distinct polynomial relations for objects with numerical spectral types [6, 19] and [20, 29] respectively.

Table 6. Objects with $>2\sigma$ Disagreement between This Work's and Filippazzo et al. (2015)'s Evolutionary Model-derived Parameters

UCS Name	F+15 Name	UCS Age ^a	F+15 Age	Mass	Mass (F+15)	Radius	Radius (F+15)	T_{eff}	T_{eff} (F+15)	$\log g$	$\log g$ (F+15)
		(Gyr)	(Gyr)	(M_{Jup})	(M_{Jup})	(R_{Jup})	(R_{Jup})	(K)	(K)	(dex)	(dex)
2MASS J00332386-1521309*	0033-1521	Truncated DL17	0.010-0.150	11.93 ± 9.98	29.05 ± 18.53	1.35 ± 0.11	1.43 ± 0.22	1401.0 ± 56.0	1887.0 ± 1175.0	4.31 ± 0.25	4.47 ± 0.42
2MASS J03185403-3421292	0318-3421	Truncated DL17	0.500-1.000	8.59 ± 7.57	48.98 ± 24.02	1.32 ± 0.08	0.97 ± 0.12	1097.0 ± 37.0	1344.0 ± 107.0	4.11 ± 0.26	5.05 ± 0.36
2MASS J03264225-2102057	0326-2102	0.130-0.200 Gyr	0.050-0.120	30.03 ± 2.30	18.4 ± 6.46	1.16 ± 0.02	1.3 ± 0.07	1534.0 ± 22.0	1381.0 ± 42.0	4.76 ± 0.05	4.39 ± 0.21
2MASS J05002110+0330501	0500+0330	Truncated DL17	0.500-10.000	13.14 ± 10.51	63.68 ± 14.44	1.50 ± 0.13	1.0 ± 0.08	1462.0 ± 62.0	1793.0 ± 72.0	4.18 ± 0.26	5.2 ± 0.19
2MASS J06244595-4521548	0624-4521	0.040-0.050 Gyr	0.500-10.000	10.78 ± 0.27	56.04 ± 18.52	1.34 ± 0.01	0.99 ± 0.1	1279.0 ± 6.0	1501.0 ± 85.0	4.18 ± 0.01	5.14 ± 0.27
2MASS J13595510-4034582	1359-4034	0.020-0.250 Gyr	0.500-10.000	24.86 ± 10.22	63.44 ± 15.48	1.30 ± 0.12	1.0 ± 0.08	1826.0 ± 88.0	1799.0 ± 106.0	4.58 ± 0.25	5.19 ± 0.2
2MASS J21481628+4003593	2148+4003	Truncated DL17	0.500-10.000	11.26 ± 9.54	55.03 ± 18.55	1.39 ± 0.10	0.99 ± 0.1	1292.0 ± 48.0	1446.0 ± 72.0	4.33 ± 0.25	5.13 ± 0.28
2MASS J10439010-235508	0439-2355	Truncated DL17	0.500-10.000	10.50 ± 9.03	48.01 ± 23.41	1.31 ± 0.09	0.97 ± 0.12	1287.0 ± 44.0	1290.0 ± 82.0	4.33 ± 0.23	5.04 ± 0.37
2MASS J10445538-304820	0445-3048	Truncated DL17	0.500-10.000	15.71 ± 11.56	63.8 ± 15.0	1.44 ± 0.14	1.0 ± 0.08	1713.0 ± 83.0	1809.0 ± 90.0	4.29 ± 0.28	5.19 ± 0.2
2MASS J10451009-340214	0451-3402	0.040-0.050 Gyr	0.500-10.000	19.95 ± 1.87	72.38 ± 12.0	1.47 ± 0.03	1.04 ± 0.06	1865.0 ± 23.0	2155.0 ± 72.0	4.43 ± 0.06	5.22 ± 0.13
2MASS J10835425-081923	0835-0819	Truncated DL17	0.500-10.000	11.75 ± 9.45	62.47 ± 15.86	1.33 ± 0.10	1.0 ± 0.08	1374.0 ± 52.0	1754.0 ± 112.0	4.32 ± 0.24	5.19 ± 0.21
2MASS J10847237-153237	0847-1532	Truncated DL17	0.500-10.000	17.12 ± 11.29	63.55 ± 14.79	1.42 ± 0.14	1.0 ± 0.08	1768.0 ± 85.0	1794.0 ± 81.0	4.34 ± 0.27	5.19 ± 0.2
2MASS J10859254-194926	0859-1949	Truncated DL17	0.500-10.000	8.73 ± 7.71	50.29 ± 23.1	1.32 ± 0.08	0.98 ± 0.11	1117.0 ± 41.0	1374.0 ± 100.0	4.11 ± 0.26	5.06 ± 0.35
2MASS J1010104-040649	1010-0406	0.150-0.250 Gyr	0.500-10.000	18.14 ± 3.23	51.16 ± 23.06	1.21 ± 0.03	0.98 ± 0.11	1257.0 ± 24.0	1416.0 ± 123.0	4.51 ± 0.09	5.07 ± 0.34
2MASS J11526140+204341	1526+2043	Truncated DL17	0.500-10.000	10.62 ± 9.57	54.39 ± 21.4	1.31 ± 0.09	0.98 ± 0.1	1295.0 ± 45.0	1518.0 ± 157.0	4.33 ± 0.23	5.1 ± 0.31
2MASS J12057540-025330	2057-0252	0.020-0.250 Gyr	0.500-10.000	25.86 ± 10.41	69.56 ± 13.04	1.30 ± 0.12	1.02 ± 0.07	1877.0 ± 89.0	2044.0 ± 87.0	4.60 ± 0.25	5.22 ± 0.15
2MASS J12104149-103736	2104-1037	Truncated DL17	0.500-10.000	13.91 ± 11.24	68.59 ± 12.82	1.43 ± 0.14	1.02 ± 0.07	1605.0 ± 79.0	1994.0 ± 73.0	4.19 ± 0.29	5.21 ± 0.16
2MASSW J0030300-145033	0030-1450	0.040-0.050 Gyr	0.500-10.000	10.14 ± 1.06	53.55 ± 21.14	1.35 ± 0.04	0.98 ± 0.1	1235.0 ± 39.0	1466.0 ± 117.0	4.16 ± 0.03	5.1 ± 0.31
2MASSW J1036530-344138	1036-3441	Truncated DL17	0.500-10.000	8.18 ± 6.88	49.24 ± 24.45	1.32 ± 0.08	0.97 ± 0.12	1074.0 ± 34.0	1368.0 ± 131.0	4.08 ± 0.25	5.04 ± 0.37
2MASSW J14392844-192915	1439+1929	Truncated DL17	0.500-10.000	18.28 ± 12.01	71.64 ± 11.6	1.41 ± 0.14	1.03 ± 0.06	1812.0 ± 90.0	2121.0 ± 61.0	4.38 ± 0.28	5.22 ± 0.13
2MASSW J1448256+103159	1448+1031	Truncated DL17	0.500-10.000	11.58 ± 9.27	59.43 ± 16.66	1.41 ± 0.09	0.99 ± 0.09	1315.0 ± 43.0	1623.0 ± 91.0	4.18 ± 0.25	5.17 ± 0.23
2MASSW J15065444+132106	1506+1321	Truncated DL17	0.500-10.000	13.55 ± 10.82	68.77 ± 12.85	1.41 ± 0.13	1.02 ± 0.07	1519.0 ± 70.0	2004.0 ± 75.0	4.20 ± 0.27	5.21 ± 0.15
2MASSW J1507476-162738	1507-1627	Truncated DL17	0.500-10.000	11.68 ± 9.56	59.66 ± 15.62	1.42 ± 0.10	0.99 ± 0.09	1325.0 ± 46.0	1607.0 ± 70.0	4.32 ± 0.25	5.18 ± 0.23
2MASSW J1515008+484742	1515+4847	Truncated DL17	0.500-10.000	9.45 ± 9.12	56.83 ± 17.52	1.34 ± 0.09	0.99 ± 0.1	1199.0 ± 40.0	1505.0 ± 74.0	4.13 ± 0.26	5.15 ± 0.26
2MASSW J2208136+292121*	2208+2921	0.010-0.150 Gyr	0.010-0.150	13.15 ± 7.39	26.71 ± 15.54	1.52 ± 0.12	1.41 ± 0.2	1532.0 ± 64.0	1804.0 ± 132.0	4.16 ± 0.24	4.44 ± 0.41
2MASSW J2244316+204343	2244+2043	0.130-0.200 Gyr	0.050-0.120	15.58 ± 1.60	11.91 ± 2.79	1.22 ± 0.02	1.29 ± 0.03	1211.0 ± 19.0	1209.0 ± 17.0	4.43 ± 0.05	4.21 ± 0.11
DENIS-P J0652197-253450	0652-2534	0.020-0.250 Gyr	0.500-10.000	26.85 ± 11.67	74.67 ± 11.18	1.33 ± 0.13	1.05 ± 0.05	1998.0 ± 97.0	2231.0 ± 60.0	4.60 ± 0.26	5.22 ± 0.12
LHS 132	1058-1548	0.040-0.050 Gyr	0.500-10.000	14.52 ± 0.34	64.24 ± 14.01	1.42 ± 0.01	1.0 ± 0.07	1570.0 ± 11.0	1809.0 ± 68.0	4.27 ± 0.01	5.2 ± 0.19
LHS 2924	1428+3310	Truncated DL17	0.500-10.000	19.21 ± 12.72	75.98 ± 10.89	1.44 ± 0.14	1.06 ± 0.05	1915.0 ± 94.0	2275.0 ± 58.0	4.38 ± 0.28	5.22 ± 0.11
LHS 3003	1456-2809	0.130-0.200 Gyr	0.500-10.000	61.46 ± 3.74	84.02 ± 9.72	1.29 ± 0.02	1.12 ± 0.05	2535.0 ± 24.0	2511.0 ± 65.0	4.98 ± 0.04	5.22 ± 0.08
Tee garden's Star	0253+1652	0.020-0.250 Gyr	0.500-10.000	45.48 ± 18.35	93.64 ± 14.47	1.46 ± 0.15	1.2 ± 0.09	2500.0 ± 126.0	2688.0 ± 212.0	4.74 ± 0.27	5.22 ± 0.07
UGPS J072227.51-054031.2	0722-0540	DL17	0.500-10.000	8.34 ± 7.68	26.11 ± 18.14	1.12 ± 0.10	0.98 ± 0.16	437.0 ± 20.0	569.0 ± 45.0	4.23 ± 0.38	4.68 ± 0.53
WISEPA J164715.59+563208.2	1647+5632	DL17	0.500-10.000	30.98 ± 23.35	41.07 ± 28.95	1.07 ± 0.17	0.94 ± 0.16	1275.0 ± 102.0	875.0 ± 132.0	4.85 ± 0.49	4.89 ± 0.57
Wolf 359	1056+0700	Truncated DL17	0.500-10.000	41.34 ± 22.09	100.7 ± 7.22	1.65 ± 0.20	1.56 ± 0.1	2562.0 ± 156.0	2517.0 ± 81.0	4.60 ± 0.33	5.19 ± 0.05
[HB88] M19	2127+4215	Truncated DL17	0.500-10.000	33.91 ± 18.97	93.91 ± 18.63	1.51 ± 0.19	1.21 ± 0.13	2391.0 ± 152.0	2676.0 ± 320.0	4.59 ± 0.34	5.22 ± 0.08
vB 8	1655-0823	Truncated DL17	0.500-10.000	28.94 ± 17.95	90.47 ± 8.0	1.52 ± 0.19	1.17 ± 0.03	2324.0 ± 147.0	2639.0 ± 40.0	4.51 ± 0.34	5.21 ± 0.06

Table 6 continued

Table 6 (*continued*)

UCS Name	F+15 Name	UCS Age ^a	F+15 Age	Mass	Mass (F+15)	Radius	Radius (F+15)	T_{eff}	T_{eff} (F+15)	$\log g$	$\log g$ (F+15)
		(Gyr)	(Gyr)	($M_{J_{\text{up}}}$)	($M_{J_{\text{up}}}$)	($R_{J_{\text{up}}}$)	($R_{J_{\text{up}}}$)	(K)	(K)	(dex)	(dex)

NOTE—For objects marked with an asterisk (*), the difference in bolometric luminosity measurements is responsible for the discrepancies in fundamental parameters. For the remaining objects, revisions to their ages are responsible for the discrepancies in fundamental parameters. See § 7.3 for more details.

^a According to Dupuy & Liu (2017, DL17) age distribution, the ages are uniformly distributed in the following age bins, where each bin contains a fraction of the total population as follows: 8.1% for 0.01–0.15 Gyr, 20.0% for 0.15–1 Gyr, 16.1% for 1–2 Gyr, 11.9% for 2–3 Gyr, 16.6% for 3–5 Gyr, 12.9% for 5–7 Gyr, and 14.4% for 7–10 Gyr. The Truncated DL17 distribution is identical to the above distribution but with an elevated lower bound of 500 Myr.

APPENDIX

A. NIR AND MIR YOUNG OBJECT ABSOLUTE MAGNITUDE-SPECTRAL TYPE RELATIONS

Polynomial relations for absolute magnitude as a function of spectral type are routinely used in literature to compute photometric distances to objects in the absence of a parallax measurement (e.g. Faherty et al. 2013; Schneider et al. 2016b, 2017; Salama et al. 2021; Zhang et al. 2022). Such relations are well-determined for field and young objects but based on fewer measurements in the latter case (Dupuy & Liu 2012; Filippazzo et al. 2015; Faherty et al. 2016; Liu et al. 2016). Here, we revisit the polynomial relations for young ultracool dwarfs (spectral type \geq M6) using the most-up-to-date information available from *The UltracoolSheet* (version 2.0.0, in preparation). Our analysis excludes unresolved multiples, subdwarfs, field objects, objects in active star-forming regions, accreting objects, objects with disks, and objects in moving groups with an age > 300 Myr (Hyades, Ursa Major, Rhea 468). Additionally, we excluded 2MASS J04221413+1530525 from the analysis due to its outlier NIR and MIR absolute magnitude. For remaining objects in *The UltracoolSheet*, we define three groups: intermediate surface gravity objects (classification of INT-G or β), low surface gravity objects (classification of VL-G, γ , or δ), and a combined group of the above spectroscopically young (low gravity classification) objects and young moving group members (as determined by BANYAN- Σ with a \geq 90% probability). A least-squares polynomial fit is performed for each of the above groups individually, for the absolute magnitudes in the 2MASS JHK_S , MKO JHK , and WISE $W1$ and $W2$ bands as a function of spectral type (photometry quoted without uncertainties, i.e., upper limits, are ignored in the fitting procedures). We could not use the F -test to determine the appropriate degree of the polynomial relation due to the low number of data points in several cases. In such a situation, a combination of visual inspection and changes in the rms of the fit was used to determine the degree of the best-fit polynomial relation. The coefficients of the best-fit polynomials are reported in Table A1 and the MKO and WISE absolute magnitude relations are plotted in Figures A1 and A2, respectively.

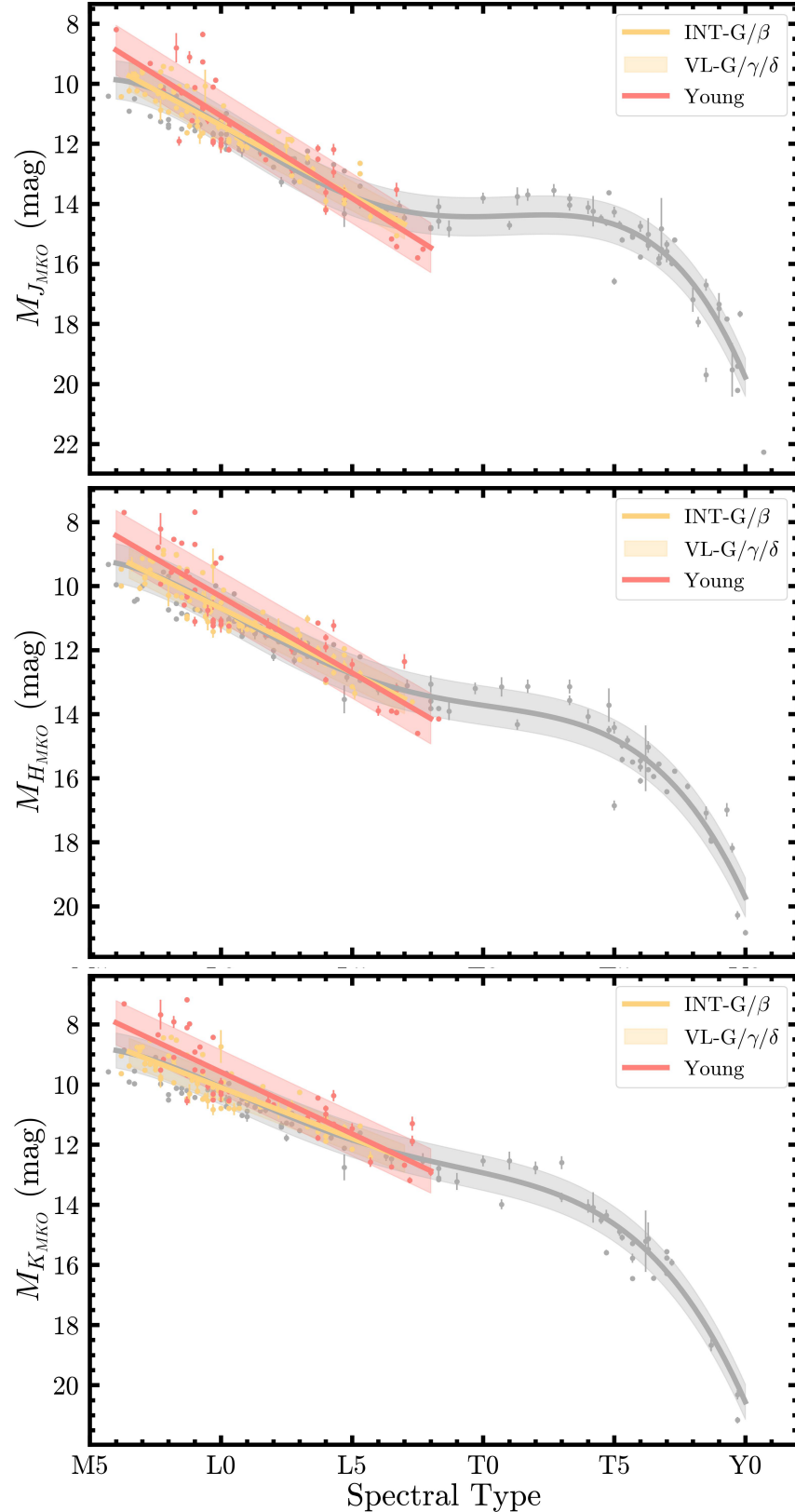


Figure A1. Absolute magnitude vs spectral type relations for intermediate gravity (yellow), low gravity (red), and young (gray) objects in the MKO JHK bands. Random scatter in the x direction with amplitude 0.3 SpT is applied to avoid overlapping points.

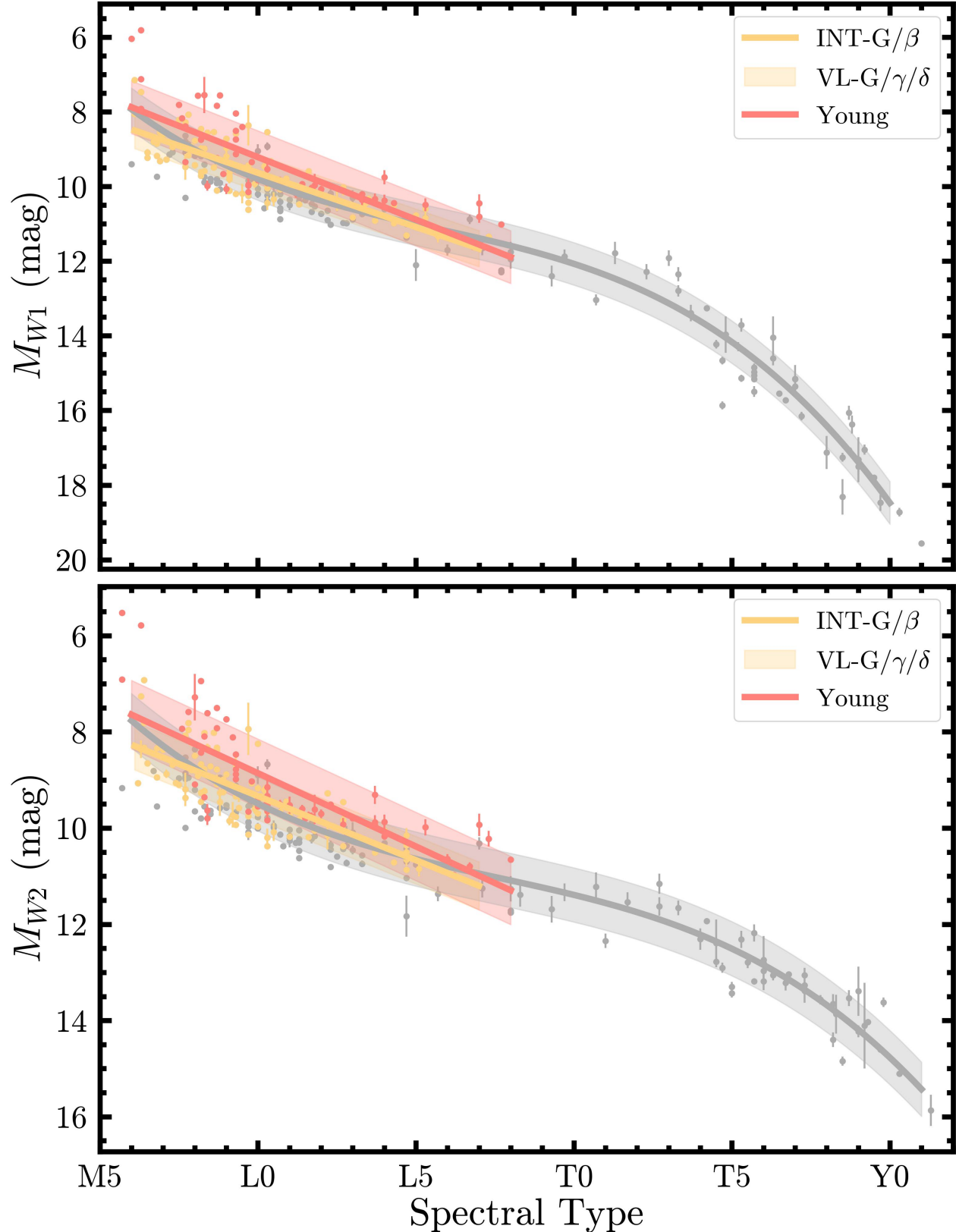


Figure A2. Same as Figure A1 for the WISE W_1 and W_2 bands.

Table A1. Absolute Magnitude-Spectral Type Polynomial Relations

$P(x)^a$	x^b	rms ^c	c_0	c_1	c_2	c_3	c_4
M_J INT-G	$6.0 \leq \text{SpT} \leq 17.0$	0.509	$6.49686469e+00$	$4.89593866e-01$
M_J VL-G	$6.0 \leq \text{SpT} \leq 18.0$	0.867	$5.30775821e+00$	$5.85807060e-01$
M_J YNG	$6.0 \leq \text{SpT} \leq 29.0$	0.639	$9.28655107e+00$	$-7.67241260e-01$	$1.79452020e-01$	$-9.69277254e-03$	$1.64408961e-04$
M_H INT-G	$6.0 \leq \text{SpT} \leq 17.0$	0.490	$6.44068903e+00$	$4.14482184e-01$
M_H VL-G	$6.0 \leq \text{SpT} \leq 18.0$	0.803	$5.18182206e+00$	$5.12068029e-01$
M_H YNG	$6.0 \leq \text{SpT} \leq 29.0$	0.604	$7.39739920e+00$	$-2.46457596e-01$	$1.12382175e-01$	$-6.67377104e-03$	$1.21697109e-04$
M_{Ks} INT-G	$6.0 \leq \text{SpT} \leq 17.0$	0.479	$6.45136804e+00$	$3.60752292e-01$
M_{Ks} VL-G	$6.0 \leq \text{SpT} \leq 18.0$	0.768	$5.23321049e+00$	$4.46473667e-01$
M_{Ks} YNG	$6.0 \leq \text{SpT} \leq 29.0$	0.597	$5.69859407e+00$	$2.48832335e-01$	$5.12670883e-02$	$-3.96997960e-03$	$8.40328391e-05$
M_J MKO,INT-G	$6.5 \leq \text{SpT} \leq 17.0$	0.492	$6.68728621e+00$	$4.70045485e-01$
M_J MKO,VL-G	$6.0 \leq \text{SpT} \leq 18.0$	0.829	$5.59034869e+00$	$5.48250755e-01$
M_J MKO,YNG	$6.0 \leq \text{SpT} \leq 30.0$	0.638	$1.59439463e+01$	$-2.59148613e+00$	$3.53603963e-01$	$-1.66425599e-02$	$2.62569032e-04$
M_H MKO,INT-G	$6.5 \leq \text{SpT} \leq 17.0$	0.469	$6.66895264e+00$	$4.02842646e-01$
M_H MKO,VL-G	$6.0 \leq \text{SpT} \leq 18.0$	0.789	$5.57417854e+00$	$4.75801078e-01$
M_H MKO,YNG	$6.0 \leq \text{SpT} \leq 30.0$	0.608	$1.25445838e+01$	$-1.57813057e+00$	$2.32989880e-01$	$-1.11747660e-02$	$1.80928732e-04$
M_K MKO,INT-G	$6.5 \leq \text{SpT} \leq 17.0$	0.455	$6.72066085e+00$	$3.37867787e-01$
M_K MKO,VL-G	$6.0 \leq \text{SpT} \leq 18.0$	0.736	$5.48128477e+00$	$4.10589460e-01$
M_K MKO,YNG	$6.0 \leq \text{SpT} \leq 30.0$	0.581	$1.13550558e+01$	$-1.25394819e+00$	$1.90091338e-01$	$-9.30942538e-03$	$1.56902337e-04$
M_{W1} INT-G	$6.0 \leq \text{SpT} \leq 17.0$	0.483	$6.73106434e+00$	$2.90360683e-01$
M_{W1} VL-G	$6.0 \leq \text{SpT} \leq 18.0$	0.707	$5.86952106e+00$	$3.34558077e-01$
M_{W1} YNG	$6.0 \leq \text{SpT} \leq 30.0$	0.569	$2.21271512e+00$	$1.33939334e+00$	$-7.38075759e-02$	$1.57439376e-03$...
M_{W2} INT-G	$6.0 \leq \text{SpT} \leq 17.0$	0.496	$6.66789839e+00$	$2.66624181e-01$
M_{W2} VL-G	$6.0 \leq \text{SpT} \leq 18.0$	0.711	$5.81406449e+00$	$3.04483215e-01$
M_{W2} YNG	$6.0 \leq \text{SpT} \leq 31.0$	0.563	$2.89919460e+00$	$1.10045304e+00$	$-5.44095936e-02$	$1.03057887e-03$...

NOTE—Since we exclude objects in star-forming regions from our sample, the YNG relations (calculated for YMG members and low gravity sources) are not appropriate for objects with ages < 10 Myr.

$$^a P(x) = \sum_{i=0}^n c_i x^i$$

^b Polynomials expressed as a function of spectral type (SpT) accept inputs in the range 6–29 corresponding to spectral types M6–T9.

^c Units are in magnitudes except where noted.

REFERENCES

- Albert, L., Artigau, É., Delorme, P., et al. 2011, *aj*, 141, 203, doi: [10.1088/0004-6256/141/6/203](https://doi.org/10.1088/0004-6256/141/6/203)
- Allard, F., Homeier, D., & Freytag, B. 2012, *Philosophical Transactions of the Royal Society of London Series A*, 370, 2765, doi: [10.1098/rsta.2011.0269](https://doi.org/10.1098/rsta.2011.0269)
- Aller, K. M. 2016, PhD thesis, University of Hawaii, Manoa
- Aller, K. M., Liu, M. C., Magnier, E. A., et al. 2016, *ApJ*, 821, 120, doi: [10.3847/0004-637X/821/2/120](https://doi.org/10.3847/0004-637X/821/2/120)
- Allers, K. N., & Liu, M. C. 2013, *ApJ*, 772, 79, doi: [10.1088/0004-637X/772/2/79](https://doi.org/10.1088/0004-637X/772/2/79)
- Allers, K. N., Liu, M. C., Dupuy, T. J., & Cushing, M. C. 2010, *apj*, 715, 561, doi: [10.1088/0004-637X/715/1/561](https://doi.org/10.1088/0004-637X/715/1/561)
- Artigau, É., Doyon, R., Lafreni`ere, D., et al. 2006, *apjl*, 651, L57, doi: [10.1086/509146](https://doi.org/10.1086/509146)
- Astropy Collaboration, Robitaille, T. P., Tollerud, E. J., et al. 2013, *A&A*, 558, A33, doi: [10.1051/0004-6361/201322068](https://doi.org/10.1051/0004-6361/201322068)
- Astropy Collaboration, Price-Whelan, A. M., Sipőcz, B. M., et al. 2018, *AJ*, 156, 123, doi: [10.3847/1538-3881/aabc4f](https://doi.org/10.3847/1538-3881/aabc4f)
- Baraffe, I., Homeier, D., Allard, F., & Chabrier, G. 2015, *A&A*, 577, A42, doi: [10.1051/0004-6361/201425481](https://doi.org/10.1051/0004-6361/201425481)
- Bardalez Gagliuffi, D. C., Burgasser, A. J., Gelino, C. R., et al. 2014, *apj*, 794, 143, doi: [10.1088/0004-637X/794/2/143](https://doi.org/10.1088/0004-637X/794/2/143)
- Bardalez Gagliuffi, D. C., Burgasser, A. J., Schmidt, S. J., et al. 2019, *apj*, 883, 205, doi: [10.3847/1538-4357/ab253d](https://doi.org/10.3847/1538-4357/ab253d)
- Barman, T. S., Macintosh, B., Konopacky, Q. M., & Marois, C. 2011, *apj*, 733, 65, doi: [10.1088/0004-637X/733/1/65](https://doi.org/10.1088/0004-637X/733/1/65)
- Baron, F., Lafreni`ere, D., Artigau, É., et al. 2015, *apj*, 802, 37, doi: [10.1088/0004-637X/802/1/37](https://doi.org/10.1088/0004-637X/802/1/37)
- Basri, G. 1998, in *Astronomical Society of the Pacific Conference Series*, Vol. 134, Brown Dwarfs and Extrasolar Planets, ed. R. Rebolo, E. L. Martin, & M. R. Zapatero Osorio, 394
- Basri, G., Mohanty, S., Allard, F., et al. 2000, *apj*, 538, 363, doi: [10.1086/309095](https://doi.org/10.1086/309095)
- Becklin, E. E., & Zuckerman, B. 1988, *at*, 336, 656, doi: [10.1038/336656a0](https://doi.org/10.1038/336656a0)
- Beichman, C., Gelino, C. R., Kirkpatrick, J. D., et al. 2014, *apj*, 783, 68, doi: [10.1088/0004-637X/783/2/68](https://doi.org/10.1088/0004-637X/783/2/68)
- Bell, C. P. M., Mamajek, E. E., & Naylor, T. 2015, *MNRAS*, 454, 593, doi: [10.1093/mnras/stv1981](https://doi.org/10.1093/mnras/stv1981)
- Bessell, M. S. 1991, *aj*, 101, 662, doi: [10.1086/115714](https://doi.org/10.1086/115714)
- Best, W. M. J., Liu, M. C., Magnier, E. A., & Dupuy, T. J. 2020, *AJ*, 159, 257, doi: [10.3847/1538-3881/ab84f4](https://doi.org/10.3847/1538-3881/ab84f4)
- . 2021, *AJ*, 161, 42, doi: [10.3847/1538-3881/abc893](https://doi.org/10.3847/1538-3881/abc893)
- Best, W. M. J., Liu, M. C., Magnier, E. A., et al. 2013, *apj*, 777, 84, doi: [10.1088/0004-637X/777/2/84](https://doi.org/10.1088/0004-637X/777/2/84)
- . 2015, *apj*, 814, 118, doi: [10.1088/0004-637X/814/2/118](https://doi.org/10.1088/0004-637X/814/2/118)
- . 2017, *apj*, 837, 95, doi: [10.3847/1538-4357/aa5df0](https://doi.org/10.3847/1538-4357/aa5df0)
- Best, W. M. J., Magnier, E. A., Liu, M. C., et al. 2018, *ApJS*, 234, 1, doi: [10.3847/1538-4365/aa9982](https://doi.org/10.3847/1538-4365/aa9982)
- Bihain, G., Scholz, R. D., Storm, J., & Schnurr, O. 2013, *aap*, 557, A43, doi: [10.1051/0004-6361/201322141](https://doi.org/10.1051/0004-6361/201322141)
- Binks, A. S., & Jeffries, R. D. 2016, *MNRAS*, 455, 3345, doi: [10.1093/mnras/stv2431](https://doi.org/10.1093/mnras/stv2431)
- Boeshaar, P. C. 1976, PhD thesis, The Ohio State University
- Booth, R. S., Poppenhaeger, K., Watson, C. A., Silva Aguirre, V., & Wolk, S. J. 2017, *MNRAS*, 471, 1012, doi: [10.1093/mnras/stx1630](https://doi.org/10.1093/mnras/stx1630)
- Bouvier, J., Kendall, T., Meeus, G., et al. 2008, *A&A*, 481, 661, doi: [10.1051/0004-6361:20079303](https://doi.org/10.1051/0004-6361:20079303)
- Bouy, H., Brandner, W., Martín, E. L., et al. 2003, *aj*, 126, 1526, doi: [10.1086/377343](https://doi.org/10.1086/377343)
- Bowler, B. P., Liu, M. C., Dupuy, T. J., & Cushing, M. C. 2010, *ApJ*, 723, 850, doi: [10.1088/0004-637X/723/1/850](https://doi.org/10.1088/0004-637X/723/1/850)
- Bowler, B. P., Liu, M. C., Shkolnik, E. L., & Dupuy, T. J. 2013, *apj*, 774, 55, doi: [10.1088/0004-637X/774/1/55](https://doi.org/10.1088/0004-637X/774/1/55)
- Bowler, B. P., Liu, M. C., Shkolnik, E. L., et al. 2012, *apj*, 753, 142, doi: [10.1088/0004-637X/753/2/142](https://doi.org/10.1088/0004-637X/753/2/142)
- Bowler, B. P., Liu, M. C., Shkolnik, E. L., & Tamura, M. 2015, *apjs*, 216, 7, doi: [10.1088/0067-0049/216/1/7](https://doi.org/10.1088/0067-0049/216/1/7)
- Burgasser, A. J. 2004, *apjl*, 614, L73, doi: [10.1086/425418](https://doi.org/10.1086/425418)
- . 2007a, *apj*, 658, 617, doi: [10.1086/511176](https://doi.org/10.1086/511176)
- . 2007b, *apj*, 659, 655, doi: [10.1086/511027](https://doi.org/10.1086/511027)
- Burgasser, A. J. 2014, in *Astronomical Society of India Conference Series*, Vol. 11, *Astronomical Society of India Conference Series*, 7–16. <https://arxiv.org/abs/1406.4887>
- Burgasser, A. J., Burrows, A., & Kirkpatrick, J. D. 2006a, *apj*, 639, 1095, doi: [10.1086/499344](https://doi.org/10.1086/499344)
- Burgasser, A. J., Cruz, K. L., Cushing, M., et al. 2010a, *apj*, 710, 1142, doi: [10.1088/0004-637X/710/2/1142](https://doi.org/10.1088/0004-637X/710/2/1142)
- Burgasser, A. J., Geballe, T. R., Leggett, S. K., Kirkpatrick, J. D., & Goliowski, D. A. 2006b, *apj*, 637, 1067, doi: [10.1086/498563](https://doi.org/10.1086/498563)
- Burgasser, A. J., Kirkpatrick, J. D., Liebert, J., & Burrows, A. 2003a, *apj*, 594, 510, doi: [10.1086/376756](https://doi.org/10.1086/376756)
- Burgasser, A. J., Kirkpatrick, J. D., McElwain, M. W., et al. 2003b, *aj*, 125, 850, doi: [10.1086/345975](https://doi.org/10.1086/345975)
- Burgasser, A. J., Liu, M. C., Ireland, M. J., Cruz, K. L., & Dupuy, T. J. 2008a, *apj*, 681, 579, doi: [10.1086/588379](https://doi.org/10.1086/588379)
- Burgasser, A. J., Looper, D. L., Kirkpatrick, J. D., Cruz, K. L., & Swift, B. J. 2008b, *apj*, 674, 451, doi: [10.1086/524726](https://doi.org/10.1086/524726)
- Burgasser, A. J., Looper, D. L., Kirkpatrick, J. D., & Liu, M. C. 2007, *apj*, 658, 557, doi: [10.1086/511518](https://doi.org/10.1086/511518)
- Burgasser, A. J., & McElwain, M. W. 2006, *aj*, 131, 1007, doi: [10.1086/499042](https://doi.org/10.1086/499042)
- Burgasser, A. J., McElwain, M. W., & Kirkpatrick, J. D. 2003c, *aj*, 126, 2487, doi: [10.1086/378608](https://doi.org/10.1086/378608)
- Burgasser, A. J., McElwain, M. W., Kirkpatrick, J. D., et al. 2004, *aj*, 127, 2856, doi: [10.1086/383549](https://doi.org/10.1086/383549)

- Burgasser, A. J., & Splat Development Team. 2017, in Astronomical Society of India Conference Series, Vol. 14, Astronomical Society of India Conference Series, 7–12, doi: [10.48550/arXiv.1707.00062](https://doi.org/10.48550/arXiv.1707.00062)
- Burgasser, A. J., Tinney, C. G., Cushing, M. C., et al. 2008c, *apjl*, 689, L53, doi: [10.1086/595747](https://doi.org/10.1086/595747)
- Burgasser, A. J., Kirkpatrick, J. D., Brown, M. E., et al. 1999, *apjl*, 522, L65, doi: [10.1086/312221](https://doi.org/10.1086/312221)
- Burgasser, A. J., Kirkpatrick, J. D., Cutri, R. M., et al. 2000a, *apjl*, 531, L57, doi: [10.1086/312522](https://doi.org/10.1086/312522)
- Burgasser, A. J., Wilson, J. C., Kirkpatrick, J. D., et al. 2000b, *aj*, 120, 1100, doi: [10.1086/301475](https://doi.org/10.1086/301475)
- Burgasser, A. J., Kirkpatrick, J. D., Brown, M. E., et al. 2002, *apj*, 564, 421, doi: [10.1086/324033](https://doi.org/10.1086/324033)
- Burgasser, A. J., Simcoe, R. A., Bochanski, J. J., et al. 2010b, *apj*, 725, 1405, doi: [10.1088/0004-637X/725/2/1405](https://doi.org/10.1088/0004-637X/725/2/1405)
- Burgasser, A. J., Lopez, M. A., Mamajek, E. E., et al. 2016, *apj*, 820, 32, doi: [10.3847/0004-637X/820/1/32](https://doi.org/10.3847/0004-637X/820/1/32)
- Burningham, B., Pinfield, D. J., Lucas, P. W., et al. 2010, *mnras*, 406, 1885, doi: [10.1111/j.1365-2966.2010.16800.x](https://doi.org/10.1111/j.1365-2966.2010.16800.x)
- Burningham, B., Lucas, P. W., Leggett, S. K., et al. 2011, *mnras*, 414, L90, doi: [10.1111/j.1745-3933.2011.01062.x](https://doi.org/10.1111/j.1745-3933.2011.01062.x)
- Burningham, B., Cardoso, C. V., Smith, L., et al. 2013, *mnras*, 433, 457, doi: [10.1093/mnras/stt740](https://doi.org/10.1093/mnras/stt740)
- Burrows, A., Marley, M., Hubbard, W. B., et al. 1997, *ApJ*, 491, 856, doi: [10.1086/305002](https://doi.org/10.1086/305002)
- Caffau, E., Ludwig, H. G., Steffen, M., Freytag, B., & Bonifacio, P. 2011, *SoPh*, 268, 255, doi: [10.1007/s11207-010-9541-4](https://doi.org/10.1007/s11207-010-9541-4)
- Cardoso, C. V., Burningham, B., Smart, R. L., et al. 2015, *mnras*, 450, 2486, doi: [10.1093/mnras/stv380](https://doi.org/10.1093/mnras/stv380)
- Carter, A. L., Hinkley, S., Kammerer, J., et al. 2022, arXiv e-prints, arXiv:2208.14990. <https://arxiv.org/abs/2208.14990>
- Casagrande, L., Schönrich, R., Asplund, M., et al. 2011, *A&A*, 530, A138, doi: [10.1051/0004-6361/201016276](https://doi.org/10.1051/0004-6361/201016276)
- Casali, M., Adamson, A., Alves de Oliveira, C., et al. 2007, *A&A*, 467, 777, doi: [10.1051/0004-6361:20066514](https://doi.org/10.1051/0004-6361:20066514)
- Castro, P. J., & Gizis, J. E. 2012, *apj*, 746, 3, doi: [10.1088/0004-637X/746/1/3](https://doi.org/10.1088/0004-637X/746/1/3)
- Castro, P. J., Gizis, J. E., Harris, H. C., et al. 2013, *apj*, 776, 126, doi: [10.1088/0004-637X/776/2/126](https://doi.org/10.1088/0004-637X/776/2/126)
- Chabrier, G., Baraffe, I., Allard, F., & Hauschildt, P. 2000, *ApJ*, 542, 464, doi: [10.1086/309513](https://doi.org/10.1086/309513)
- Chabrier, G., Mazevert, S., & Soubiran, F. 2019, *ApJ*, 872, 51, doi: [10.3847/1538-4357/aaf99f](https://doi.org/10.3847/1538-4357/aaf99f)
- Chambers, K. C., Magnier, E. A., Metcalfe, N., et al. 2016, arXiv e-prints, arXiv:1612.05560. <https://arxiv.org/abs/1612.05560>
- Chiu, K., Fan, X., Leggett, S. K., et al. 2006, *aj*, 131, 2722, doi: [10.1086/501431](https://doi.org/10.1086/501431)
- Crifo, F., Phan-Bao, N., Delfosse, X., et al. 2005, *aap*, 441, 653, doi: [10.1051/0004-6361:20052998](https://doi.org/10.1051/0004-6361:20052998)
- Cruz, K. L., Kirkpatrick, J. D., & Burgasser, A. J. 2009, *aj*, 137, 3345, doi: [10.1088/0004-6256/137/2/3345](https://doi.org/10.1088/0004-6256/137/2/3345)
- Cruz, K. L., Núñez, A., Burgasser, A. J., et al. 2018, *AJ*, 155, 34, doi: [10.3847/1538-3881/aa9d8a](https://doi.org/10.3847/1538-3881/aa9d8a)
- Cruz, K. L., Reid, I. N., Liebert, J., Kirkpatrick, J. D., & Lowrance, P. J. 2003, *aj*, 126, 2421, doi: [10.1086/378607](https://doi.org/10.1086/378607)
- Cruz, K. L., Reid, I. N., Kirkpatrick, J. D., et al. 2007, *aj*, 133, 439, doi: [10.1086/510132](https://doi.org/10.1086/510132)
- Cushing, M. C., Kirkpatrick, J. D., Gelino, C. R., et al. 2014, *aj*, 147, 113, doi: [10.1088/0004-6256/147/5/113](https://doi.org/10.1088/0004-6256/147/5/113)
- Cushing, M. C., Vacca, W. D., & Rayner, J. T. 2004, *PASP*, 116, 362, doi: [10.1086/382907](https://doi.org/10.1086/382907)
- Cushing, M. C., Marley, M. S., Saumon, D., et al. 2008, *ApJ*, 678, 1372, doi: [10.1086/526489](https://doi.org/10.1086/526489)
- Cushing, M. C., Kirkpatrick, J. D., Gelino, C. R., et al. 2011, *apj*, 743, 50, doi: [10.1088/0004-637X/743/1/50](https://doi.org/10.1088/0004-637X/743/1/50)
- Cutri, R. M., Skrutskie, M. F., van Dyk, S., et al. 2003, 2MASS All Sky Catalog of point sources.
- Cutri, R. M., Wright, E. L., Conrow, T., et al. 2021, VizieR Online Data Catalog, II/328
- Dahn, C. C., Harris, H. C., Vrba, F. J., et al. 2002, *AJ*, 124, 1170, doi: [10.1086/341646](https://doi.org/10.1086/341646)
- Dahn, C. C., Harris, H. C., Subasavage, J. P., et al. 2017, *aj*, 154, 147, doi: [10.3847/1538-3881/aa880b](https://doi.org/10.3847/1538-3881/aa880b)
- Deacon, N. R., & Hambley, N. C. 2007, *aap*, 468, 163, doi: [10.1051/0004-6361:20066844](https://doi.org/10.1051/0004-6361:20066844)
- Deacon, N. R., Hambley, N. C., & Cooke, J. A. 2005, *aap*, 435, 363, doi: [10.1051/0004-6361:20042002](https://doi.org/10.1051/0004-6361:20042002)
- Deacon, N. R., Liu, M. C., Magnier, E. A., et al. 2011, *aj*, 142, 77, doi: [10.1088/0004-6256/142/3/77](https://doi.org/10.1088/0004-6256/142/3/77)
- . 2012a, *apj*, 757, 100, doi: [10.1088/0004-637X/757/1/100](https://doi.org/10.1088/0004-637X/757/1/100)
- . 2012b, *apj*, 755, 94, doi: [10.1088/0004-637X/755/2/94](https://doi.org/10.1088/0004-637X/755/2/94)
- . 2014, *apj*, 792, 119, doi: [10.1088/0004-637X/792/2/119](https://doi.org/10.1088/0004-637X/792/2/119)
- Deacon, N. R., Magnier, E. A., Liu, M. C., et al. 2017, *mnras*, 467, 1126, doi: [10.1093/mnras/stx065](https://doi.org/10.1093/mnras/stx065)
- Delfosse, X., Tinney, C. G., Forveille, T., et al. 1999, *aaps*, 135, 41, doi: [10.1051/aas:1999158](https://doi.org/10.1051/aas:1999158)
- . 1997, *aap*, 327, L25
- Dobbie, P. D., Kenyon, F., Jameson, R. F., et al. 2002, *mnras*, 329, 543, doi: [10.1046/j.1365-8711.2002.05002.x](https://doi.org/10.1046/j.1365-8711.2002.05002.x)
- Dupuy, T. J., & Kraus, A. L. 2013, *Science*, 341, 1492, doi: [10.1126/science.1241917](https://doi.org/10.1126/science.1241917)
- Dupuy, T. J., & Liu, M. C. 2012, *apjs*, 201, 19, doi: [10.1088/0067-0049/201/2/19](https://doi.org/10.1088/0067-0049/201/2/19)
- . 2017, *ApJS*, 231, 15, doi: [10.3847/1538-4365/aa5e4c](https://doi.org/10.3847/1538-4365/aa5e4c)
- Dupuy, T. J., Liu, M. C., Bowler, B. P., et al. 2010, *apj*, 721, 1725, doi: [10.1088/0004-637X/721/2/1725](https://doi.org/10.1088/0004-637X/721/2/1725)
- Dupuy, T. J., Liu, M. C., Evans, E. L., et al. 2023, *MNRAS*, 519, 1688, doi: [10.1093/mnras/stac3557](https://doi.org/10.1093/mnras/stac3557)

- Dupuy, T. J., Liu, M. C., & Ireland, M. J. 2009, *apj*, 692, 729, doi: [10.1088/0004-637X/692/1/729](https://doi.org/10.1088/0004-637X/692/1/729)
- Dupuy, T. J., Liu, M. C., Leggett, S. K., et al. 2015, *apj*, 805, 56, doi: [10.1088/0004-637X/805/1/56](https://doi.org/10.1088/0004-637X/805/1/56)
- Dupuy, T. J., Liu, M. C., Allers, K. N., et al. 2018, *aj*, 156, 57, doi: [10.3847/1538-3881/aacbc2](https://doi.org/10.3847/1538-3881/aacbc2)
- Dye, S., Lawrence, A., Read, M. A., et al. 2018, *MNRAS*, 473, 5113, doi: [10.1093/mnras/stx2622](https://doi.org/10.1093/mnras/stx2622)
- Edge, A., Sutherland, W., & Viking Team. 2016, VizieR Online Data Catalog, II/343
- Eisenhardt, P. R. M., Marocco, F., Fowler, J. W., et al. 2020, *ApJS*, 247, 69, doi: [10.3847/1538-4365/ab7f2a](https://doi.org/10.3847/1538-4365/ab7f2a)
- Ellis, S. C., Tinney, C. G., Burgasser, A. J., Kirkpatrick, J. D., & McElwain, M. W. 2005, *aj*, 130, 2347, doi: [10.1086/491790](https://doi.org/10.1086/491790)
- EROS Collaboration, Goldman, B., Delfosse, X., et al. 1999, *aap*, 351, L5. <https://arxiv.org/abs/astro-ph/9905162>
- Faherty, J. K., Burgasser, A. J., Cruz, K. L., et al. 2009, *aj*, 137, 1, doi: [10.1088/0004-6256/137/1/1](https://doi.org/10.1088/0004-6256/137/1/1)
- Faherty, J. K., Burgasser, A. J., West, A. A., et al. 2010, *aj*, 139, 176, doi: [10.1088/0004-6256/139/1/176](https://doi.org/10.1088/0004-6256/139/1/176)
- Faherty, J. K., Rice, E. L., Cruz, K. L., Mamajek, E. E., & Núñez, A. 2013, *aj*, 145, 2, doi: [10.1088/0004-6256/145/1/2](https://doi.org/10.1088/0004-6256/145/1/2)
- Faherty, J. K., Burgasser, A. J., Walter, F. M., et al. 2012, *apj*, 752, 56, doi: [10.1088/0004-637X/752/1/56](https://doi.org/10.1088/0004-637X/752/1/56)
- Faherty, J. K., Riedel, A. R., Cruz, K. L., et al. 2016, *ApJS*, 225, 10, doi: [10.3847/0067-0049/225/1/10](https://doi.org/10.3847/0067-0049/225/1/10)
- Fan, X., Knapp, G. R., Strauss, M. A., et al. 2000, *aj*, 119, 928, doi: [10.1086/301224](https://doi.org/10.1086/301224)
- Fazio, G. G., Hora, J. L., Allen, L. E., et al. 2004, *ApJS*, 154, 10, doi: [10.1086/422843](https://doi.org/10.1086/422843)
- Feeeser, S. J., Best, W. M. J., Sanghi, A., & Liu, M. C. 2022, Research Notes of the American Astronomical Society, 6, 265, doi: [10.3847/2515-5172/acaafb](https://doi.org/10.3847/2515-5172/acaafb)
- Filippazzo, J. C., Rice, E. L., Faherty, J., et al. 2015, *ApJ*, 810, 158, doi: [10.1088/0004-637X/810/2/158](https://doi.org/10.1088/0004-637X/810/2/158)
- Folkes, S. L., Pinfield, D. J., Kendall, T. R., & Jones, H. R. A. 2007, *mnras*, 378, 901, doi: [10.1111/j.1365-2966.2007.11789.x](https://doi.org/10.1111/j.1365-2966.2007.11789.x)
- Folkes, S. L., Pinfield, D. J., Jones, H. R. A., et al. 2012, *mnras*, 427, 3280, doi: [10.1111/j.1365-2966.2012.21132.x](https://doi.org/10.1111/j.1365-2966.2012.21132.x)
- Forveille, T., Ségransan, D., Delorme, P., et al. 2004, *A&A*, 427, L1, doi: [10.1051/0004-6361:200400069](https://doi.org/10.1051/0004-6361:200400069)
- Gagné, J., & Faherty, J. K. 2018, *apj*, 862, 138, doi: [10.3847/1538-4357/aaca2e](https://doi.org/10.3847/1538-4357/aaca2e)
- Gagné, J., Faherty, J. K., Cruz, K., et al. 2014a, *apjl*, 785, L14, doi: [10.1088/2041-8205/785/1/L14](https://doi.org/10.1088/2041-8205/785/1/L14)
- Gagné, J., Lafreni`ere, D., Doyon, R., et al. 2014b, *apjl*, 792, L17, doi: [10.1088/2041-8205/792/1/L17](https://doi.org/10.1088/2041-8205/792/1/L17)
- Gagné, J., Lafreni`ere, D., Doyon, R., Malo, L., & Artigau, É. 2014c, *apj*, 783, 121, doi: [10.1088/0004-637X/783/2/121](https://doi.org/10.1088/0004-637X/783/2/121)
- Gagné, J., Moranta, L., Faherty, J. K., et al. 2022, arXiv e-prints, arXiv:2208.00070. <https://arxiv.org/abs/2208.00070>
- Gagné, J., Faherty, J. K., Cruz, K. L., et al. 2015, *apjs*, 219, 33, doi: [10.1088/0067-0049/219/2/33](https://doi.org/10.1088/0067-0049/219/2/33)
- Gagné, J., Faherty, J. K., Mamajek, E. E., et al. 2017, *apjs*, 228, 18, doi: [10.3847/1538-4365/228/2/18](https://doi.org/10.3847/1538-4365/228/2/18)
- Gagné, J., Mamajek, E. E., Malo, L., et al. 2018, *apj*, 856, 23, doi: [10.3847/1538-4357/aaae09](https://doi.org/10.3847/1538-4357/aaae09)
- Gaia Collaboration, Vallenari, A., Brown, A. G. A., et al. 2023, *A&A*, 674, A1, doi: [10.1051/0004-6361/202243940](https://doi.org/10.1051/0004-6361/202243940)
- Gauza, B., Béjar, V. J. S., Pérez-Garrido, A., et al. 2019, *mnras*, 487, 1149, doi: [10.1093/mnras/stz1284](https://doi.org/10.1093/mnras/stz1284)
- Geballe, T. R., Saumon, D., Golimowski, D. A., et al. 2009, *ApJ*, 695, 844, doi: [10.1088/0004-637X/695/2/844](https://doi.org/10.1088/0004-637X/695/2/844)
- Geballe, T. R., Knapp, G. R., Leggett, S. K., et al. 2002, *apj*, 564, 466, doi: [10.1086/324078](https://doi.org/10.1086/324078)
- Geissler, K., Metchev, S., Kirkpatrick, J. D., Berriman, G. B., &Looper, D. 2011, *apj*, 732, 56, doi: [10.1088/0004-637X/732/1/56](https://doi.org/10.1088/0004-637X/732/1/56)
- Giampapa, M. S., & Liebert, J. 1986, *apj*, 305, 784, doi: [10.1086/164291](https://doi.org/10.1086/164291)
- Giclas, H. L., Burnham, R., & Thomas, N. G. 1971, Lowell proper motion survey Northern Hemisphere. The G numbered stars. 8991 stars fainter than magnitude 8 with motions ζ 0''.26/year
- Gillon, M., Jehin, E., Lederer, S. M., et al. 2016, *at*, 533, 221, doi: [10.1038/nature17448](https://doi.org/10.1038/nature17448)
- Gilmore, G., Reid, N., & Hewett, P. 1985, *mnras*, 213, 257, doi: [10.1093/mnras/213.2.257](https://doi.org/10.1093/mnras/213.2.257)
- Gizis, J. E. 2002, *apj*, 575, 484, doi: [10.1086/341259](https://doi.org/10.1086/341259)
- Gizis, J. E., Allers, K. N., Liu, M. C., et al. 2015a, *apj*, 799, 203, doi: [10.1088/0004-637X/799/2/203](https://doi.org/10.1088/0004-637X/799/2/203)
- Gizis, J. E., Burgasser, A. J., Berger, E., et al. 2013, *apj*, 779, 172, doi: [10.1088/0004-637X/779/2/172](https://doi.org/10.1088/0004-637X/779/2/172)
- Gizis, J. E., Burgasser, A. J., Faherty, J. K., Castro, P. J., & Shara, M. M. 2011a, *aj*, 142, 171, doi: [10.1088/0004-6256/142/5/171](https://doi.org/10.1088/0004-6256/142/5/171)
- Gizis, J. E., Burgasser, A. J., & Vrba, F. J. 2015b, *aj*, 150, 179, doi: [10.1088/0004-6256/150/6/179](https://doi.org/10.1088/0004-6256/150/6/179)
- Gizis, J. E., Kirkpatrick, J. D., & Wilson, J. C. 2001, *aj*, 121, 2185, doi: [10.1086/319937](https://doi.org/10.1086/319937)
- Gizis, J. E., Monet, D. G., Reid, I. N., et al. 2000, *aj*, 120, 1085, doi: [10.1086/301456](https://doi.org/10.1086/301456)
- Gizis, J. E., & Reid, I. N. 1997, *pasp*, 109, 849, doi: [10.1086/133955](https://doi.org/10.1086/133955)
- Gizis, J. E., Reid, I. N., Knapp, G. R., et al. 2003, *aj*, 125, 3302, doi: [10.1086/374991](https://doi.org/10.1086/374991)
- Gizis, J. E., Troup, N. W., & Burgasser, A. J. 2011b, *apjl*, 736, L34, doi: [10.1088/2041-8205/736/2/L34](https://doi.org/10.1088/2041-8205/736/2/L34)
- Gizis, J. E., Faherty, J. K., Liu, M. C., et al. 2012, *aj*, 144, 94, doi: [10.1088/0004-6256/144/4/94](https://doi.org/10.1088/0004-6256/144/4/94)

- Goldman, B., Marsat, S., Henning, T., Clemens, C., & Greiner, J. 2010, *mnras*, 405, 1140, doi: [10.1111/j.1365-2966.2010.16524.x](https://doi.org/10.1111/j.1365-2966.2010.16524.x)
- Golimowski, D. A., Henry, T. J., Krist, J. E., et al. 2004, *aj*, 128, 1733, doi: [10.1086/423911](https://doi.org/10.1086/423911)
- Gomes, J. I., Pinfield, D. J., Marocco, F., et al. 2013, *mnras*, 431, 2745, doi: [10.1093/mnras/stt371](https://doi.org/10.1093/mnras/stt371)
- Griffith, R. L., Kirkpatrick, J. D., Eisenhardt, P. R. M., et al. 2012, *aj*, 144, 148, doi: [10.1088/0004-6256/144/5/148](https://doi.org/10.1088/0004-6256/144/5/148)
- Hambly, N. C., Collins, R. S., Cross, N. J. G., et al. 2008, *MNRAS*, 384, 637, doi: [10.1111/j.1365-2966.2007.12700.x](https://doi.org/10.1111/j.1365-2966.2007.12700.x)
- Harris, C. R., Millman, K. J., van der Walt, S. J., et al. 2020, *Nature*, 585, 357, doi: [10.1038/s41586-020-2649-2](https://doi.org/10.1038/s41586-020-2649-2)
- Hawkins, M. R. S., & Bessell, M. S. 1988, *mnras*, 234, 177, doi: [10.1093/mnras/234.2.177](https://doi.org/10.1093/mnras/234.2.177)
- Hawley, S. L., Covey, K. R., Knapp, G. R., et al. 2002, *aj*, 123, 3409, doi: [10.1086/340697](https://doi.org/10.1086/340697)
- Henry, T. J., Jao, W.-C., Subasavage, J. P., et al. 2006, *aj*, 132, 2360, doi: [10.1086/508233](https://doi.org/10.1086/508233)
- Henry, T. J., & Kirkpatrick, J. D. 1990, *apjl*, 354, L29, doi: [10.1086/185715](https://doi.org/10.1086/185715)
- Henry, T. J., Subasavage, J. P., Brown, M. A., et al. 2004, *aj*, 128, 2460, doi: [10.1086/425052](https://doi.org/10.1086/425052)
- Herczeg, G. J., & Hillenbrand, L. A. 2015, *ApJ*, 808, 23, doi: [10.1088/0004-637X/808/1/23](https://doi.org/10.1088/0004-637X/808/1/23)
- Hewett, P. C., Warren, S. J., Leggett, S. K., & Hodgkin, S. T. 2006, *MNRAS*, 367, 454, doi: [10.1111/j.1365-2966.2005.09969.x](https://doi.org/10.1111/j.1365-2966.2005.09969.x)
- Hsu, C.-C., Burgasser, A. J., Theissen, C. A., et al. 2021, *apjs*, 257, 45, doi: [10.3847/1538-4365/ac1c7d](https://doi.org/10.3847/1538-4365/ac1c7d)
- Hunter, J. D. 2007, *Computing in Science and Engineering*, 9, 90, doi: [10.1109/MCSE.2007.55](https://doi.org/10.1109/MCSE.2007.55)
- Irwin, M., McMahon, R. G., & Reid, N. 1991, *mnras*, 252, 61P, doi: [10.1093/mnras/252.1.61P](https://doi.org/10.1093/mnras/252.1.61P)
- Irwin, M. J. 2008, in 2007 ESO Instrument Calibration Workshop, ed. A. Kaufer & F. Kerber, 541, doi: [10.1007/978-3-540-76963-7_74](https://doi.org/10.1007/978-3-540-76963-7_74)
- Jackson, A. P., Davis, T. A., & Wheatley, P. J. 2012, *MNRAS*, 422, 2024, doi: [10.1111/j.1365-2966.2012.20657.x](https://doi.org/10.1111/j.1365-2966.2012.20657.x)
- Kellogg, K., Metchev, S., Geissler, K., et al. 2015, *aj*, 150, 182, doi: [10.1088/0004-6256/150/6/182](https://doi.org/10.1088/0004-6256/150/6/182)
- Kellogg, K., Metchev, S., Miles-Páez, P. A., & Tannock, M. E. 2017, *aj*, 154, 112, doi: [10.3847/1538-3881/aa83b0](https://doi.org/10.3847/1538-3881/aa83b0)
- Kendall, T. R., Delfosse, X., Martín, E. L., & Forveille, T. 2004, *aap*, 416, L17, doi: [10.1051/0004-6361:20040046](https://doi.org/10.1051/0004-6361:20040046)
- Kendall, T. R., Jones, H. R. A., Pinfield, D. J., et al. 2007, *mnras*, 374, 445, doi: [10.1111/j.1365-2966.2006.11026.x](https://doi.org/10.1111/j.1365-2966.2006.11026.x)
- Kendall, T. R., Mauron, N., Azzopardi, M., & Gigoyan, K. 2003, *aap*, 403, 929, doi: [10.1051/0004-6361:20030218](https://doi.org/10.1051/0004-6361:20030218)
- Kiman, R., Faherty, J. K., Cruz, K. L., et al. 2021, *AJ*, 161, 277, doi: [10.3847/1538-3881/abf561](https://doi.org/10.3847/1538-3881/abf561)
- Kirkpatrick, J. D. 2005, *ARA&A*, 43, 195, doi: [10.1146/annurev.astro.42.053102.134017](https://doi.org/10.1146/annurev.astro.42.053102.134017)
- Kirkpatrick, J. D., Barman, T. S., Burgasser, A. J., et al. 2006, *apj*, 639, 1120, doi: [10.1086/499622](https://doi.org/10.1086/499622)
- Kirkpatrick, J. D., Beichman, C. A., & Skrutskie, M. F. 1997a, *apj*, 476, 311, doi: [10.1086/303613](https://doi.org/10.1086/303613)
- Kirkpatrick, J. D., Dahn, C. C., Monet, D. G., et al. 2001, *aj*, 121, 3235, doi: [10.1086/321085](https://doi.org/10.1086/321085)
- Kirkpatrick, J. D., Henry, T. J., & Irwin, M. J. 1997b, *aj*, 113, 1421, doi: [10.1086/118357](https://doi.org/10.1086/118357)
- Kirkpatrick, J. D., Henry, T. J., & McCarthy, Donald W., J. 1991, *apjs*, 77, 417, doi: [10.1086/191611](https://doi.org/10.1086/191611)
- Kirkpatrick, J. D., Henry, T. J., & Simons, D. A. 1995, *aj*, 109, 797, doi: [10.1086/117323](https://doi.org/10.1086/117323)
- Kirkpatrick, J. D., McGraw, J. T., Hess, T. R., Liebert, J., & McCarthy, Donald W., J. 1994, *apjs*, 94, 749, doi: [10.1086/192089](https://doi.org/10.1086/192089)
- Kirkpatrick, J. D., Reid, I. N., Liebert, J., et al. 1999, *apj*, 519, 802, doi: [10.1086/307414](https://doi.org/10.1086/307414)
- . 2000, *aj*, 120, 447, doi: [10.1086/301427](https://doi.org/10.1086/301427)
- Kirkpatrick, J. D., Cruz, K. L., Barman, T. S., et al. 2008, *apj*, 689, 1295, doi: [10.1086/592768](https://doi.org/10.1086/592768)
- Kirkpatrick, J. D.,Looper, D. L.,Burgasser, A. J.,et al. 2010, *apjs*, 190, 100, doi: [10.1088/0067-0049/190/1/100](https://doi.org/10.1088/0067-0049/190/1/100)
- Kirkpatrick, J. D., Cushing, M. C., Gelino, C. R., et al. 2011, *apjs*, 197, 19, doi: [10.1088/0067-0049/197/2/19](https://doi.org/10.1088/0067-0049/197/2/19)
- Kirkpatrick, J. D., Gelino, C. R., Cushing, M. C., et al. 2012, *apj*, 753, 156, doi: [10.1088/0004-637X/753/2/156](https://doi.org/10.1088/0004-637X/753/2/156)
- Kirkpatrick, J. D., Schneider, A., Fajardo-Acosta, S., et al. 2014, *apj*, 783, 122, doi: [10.1088/0004-637X/783/2/122](https://doi.org/10.1088/0004-637X/783/2/122)
- Kirkpatrick, J. D., Kellogg, K., Schneider, A. C., et al. 2016, *apjs*, 224, 36, doi: [10.3847/0067-0049/224/2/36](https://doi.org/10.3847/0067-0049/224/2/36)
- Kirkpatrick, J. D., Martin, E. C., Smart, R. L., et al. 2019, *ApJS*, 240, 19, doi: [10.3847/1538-4365/aaf6af](https://doi.org/10.3847/1538-4365/aaf6af)
- Kirkpatrick, J. D., Gelino, C. R., Faherty, J. K., et al. 2021, *ApJS*, 253, 7, doi: [10.3847/1538-4365/abd107](https://doi.org/10.3847/1538-4365/abd107)
- Knapp, G. R., Leggett, S. K., Fan, X., et al. 2004, *aj*, 127, 3553, doi: [10.1086/420707](https://doi.org/10.1086/420707)
- Koen, C., Miszalski, B., V”ais”anen, P., & Koen, T. 2017, *mnras*, 465, 4723, doi: [10.1093/mnras/stw3106](https://doi.org/10.1093/mnras/stw3106)
- Lawrence, A., Warren, S. J., Almaini, O., et al. 2007, *mnras*, 379, 1599, doi: [10.1111/j.1365-2966.2007.12040.x](https://doi.org/10.1111/j.1365-2966.2007.12040.x)
- . 2012, VizieR Online Data Catalog, II/314
- Leggett, S. K. 1992, *apjs*, 82, 351, doi: [10.1086/191720](https://doi.org/10.1086/191720)
- Leggett, S. K., Allard, F., & Hauschildt, P. H. 1998, *apj*, 509, 836, doi: [10.1086/306517](https://doi.org/10.1086/306517)
- Leggett, S. K., Morley, C. V., Marley, M. S., & Saumon, D. 2015, *ApJ*, 799, 37, doi: [10.1088/0004-637X/799/1/37](https://doi.org/10.1088/0004-637X/799/1/37)
- Leggett, S. K., Saumon, D., Marley, M. S., et al. 2007, *apj*, 655, 1079, doi: [10.1086/510014](https://doi.org/10.1086/510014)

- Leggett, S. K., Geballe, T. R., Fan, X., et al. 2000, *apjl*, 536, L35, doi: [10.1086/312728](https://doi.org/10.1086/312728)
- Leggett, S. K., Goliowski, D. A., Fan, X., et al. 2002, *apj*, 564, 452, doi: [10.1086/324037](https://doi.org/10.1086/324037)
- Leggett, S. K., Currie, M. J., Varricatt, W. P., et al. 2006, *mnras*, 373, 781, doi: [10.1111/j.1365-2966.2006.11069.x](https://doi.org/10.1111/j.1365-2966.2006.11069.x)
- Leggett, S. K., Cushing, M. C., Saumon, D., et al. 2009, *apj*, 695, 1517, doi: [10.1088/0004-637X/695/2/1517](https://doi.org/10.1088/0004-637X/695/2/1517)
- Leggett, S. K., Birmingham, B., Saumon, D., et al. 2010, *apj*, 710, 1627, doi: [10.1088/0004-637X/710/2/1627](https://doi.org/10.1088/0004-637X/710/2/1627)
- Leggett, S. K., Saumon, D., Marley, M. S., et al. 2012, *apj*, 748, 74, doi: [10.1088/0004-637X/748/2/74](https://doi.org/10.1088/0004-637X/748/2/74)
- Lépine, S., & Shara, M. M. 2005, *aj*, 129, 1483, doi: [10.1086/427854](https://doi.org/10.1086/427854)
- Lépine, S., Thorstensen, J. R., Shara, M. M., & Rich, R. M. 2009, *aj*, 137, 4109, doi: [10.1088/0004-6256/137/5/4109](https://doi.org/10.1088/0004-6256/137/5/4109)
- Liebert, J., & Burgasser, A. J. 2007, *ApJ*, 655, 522, doi: [10.1086/509882](https://doi.org/10.1086/509882)
- Liebert, J., Dahn, C. C., Gresham, M., & Strittmatter, P. A. 1979, *apj*, 233, 226, doi: [10.1086/157384](https://doi.org/10.1086/157384)
- Liebert, J., & Gizis, J. E. 2006, *pasp*, 118, 659, doi: [10.1086/503333](https://doi.org/10.1086/503333)
- Liebert, J., Kirkpatrick, J. D., Cruz, K. L., et al. 2003, *aj*, 125, 343, doi: [10.1086/345514](https://doi.org/10.1086/345514)
- Liu, M. C., Dupuy, T. J., & Allers, K. N. 2016, *ApJ*, 833, 96, doi: [10.3847/1538-4357/833/1/96](https://doi.org/10.3847/1538-4357/833/1/96)
- Liu, M. C., Dupuy, T. J., & Ireland, M. J. 2008, *apj*, 689, 436, doi: [10.1086/591837](https://doi.org/10.1086/591837)
- Liu, M. C., Dupuy, T. J., & Leggett, S. K. 2010, *apj*, 722, 311, doi: [10.1088/0004-637X/722/1/311](https://doi.org/10.1088/0004-637X/722/1/311)
- Liu, M. C., Deacon, N. R., Magnier, E. A., et al. 2011, *apjl*, 740, L32, doi: [10.1088/2041-8205/740/2/L32](https://doi.org/10.1088/2041-8205/740/2/L32)
- Liu, M. C., Magnier, E. A., Deacon, N. R., et al. 2013, *apjl*, 777, L20, doi: [10.1088/2041-8205/777/2/L20](https://doi.org/10.1088/2041-8205/777/2/L20)
- Lodieu, N. 2013, *mnras*, 431, 3222, doi: [10.1093/mnras/stt402](https://doi.org/10.1093/mnras/stt402)
- Lodieu, N., Boudreault, S., & Béjar, V. J. S. 2014, *mnras*, 445, 3908, doi: [10.1093/mnras/stu2059](https://doi.org/10.1093/mnras/stu2059)
- Lodieu, N., Scholz, R. D., & McCaughrean, M. J. 2002, *aap*, 389, L20, doi: [10.1051/0004-6361:20020698](https://doi.org/10.1051/0004-6361:20020698)
- Lodieu, N., Scholz, R. D., McCaughrean, M. J., et al. 2005, *aap*, 440, 1061, doi: [10.1051/0004-6361:20042456](https://doi.org/10.1051/0004-6361:20042456)
- Lodieu, N., Birmingham, B., Day-Jones, A., et al. 2012, *aap*, 548, A53, doi: [10.1051/0004-6361/201220182](https://doi.org/10.1051/0004-6361/201220182)
- Looper, D. L., Burgasser, A. J., Kirkpatrick, J. D., & Swift, B. J. 2007a, *apjl*, 669, L97, doi: [10.1086/523812](https://doi.org/10.1086/523812)
- Looper, D. L., Kirkpatrick, J. D., & Burgasser, A. J. 2007b, *aj*, 134, 1162, doi: [10.1086/520645](https://doi.org/10.1086/520645)
- Looper, D. L., Kirkpatrick, J. D., Cutri, R. M., et al. 2008, *apj*, 686, 528, doi: [10.1086/591025](https://doi.org/10.1086/591025)
- Lucas, P. W., Tinney, C. G., Birmingham, B., et al. 2010, *mnras*, 408, L56, doi: [10.1111/j.1745-3933.2010.00927.x](https://doi.org/10.1111/j.1745-3933.2010.00927.x)
- Lueber, A., Kitzmann, D., Fisher, C. E., et al. 2023, *ApJ*, 954, 22, doi: [10.3847/1538-4357/ace530](https://doi.org/10.3847/1538-4357/ace530)
- Luhman, K. L. 2006, *apj*, 645, 676, doi: [10.1086/504073](https://doi.org/10.1086/504073)
- . 2014, *apj*, 781, 4, doi: [10.1088/0004-637X/781/1/4](https://doi.org/10.1088/0004-637X/781/1/4)
- Luhman, K. L., Mamajek, E. E., Allen, P. R., & Cruz, K. L. 2009, *apj*, 703, 399, doi: [10.1088/0004-637X/703/1/399](https://doi.org/10.1088/0004-637X/703/1/399)
- Luhman, K. L., & Sheppard, S. S. 2014, *apj*, 787, 126, doi: [10.1088/0004-637X/787/2/126](https://doi.org/10.1088/0004-637X/787/2/126)
- Luhman, K. L., Patten, B. M., Marengo, M., et al. 2007, *apj*, 654, 570, doi: [10.1086/509073](https://doi.org/10.1086/509073)
- Luhman, K. L., Loutrel, N. P., McCurdy, N. S., et al. 2012, *apj*, 760, 152, doi: [10.1088/0004-637X/760/2/152](https://doi.org/10.1088/0004-637X/760/2/152)
- Mace, G. N., Kirkpatrick, J. D., Cushing, M. C., et al. 2013, *apjs*, 205, 6, doi: [10.1088/0067-0049/205/1/6](https://doi.org/10.1088/0067-0049/205/1/6)
- Magnier, E. A., Schlafly, E. F., Finkbeiner, D. P., et al. 2020, *ApJS*, 251, 6, doi: [10.3847/1538-4365/abb82a](https://doi.org/10.3847/1538-4365/abb82a)
- Malo, L., Doyon, R., Lafrenière, D., et al. 2013, *apj*, 762, 88, doi: [10.1088/0004-637X/762/2/88](https://doi.org/10.1088/0004-637X/762/2/88)
- Mamajek, E. E., Prsa, A., Torres, G., et al. 2015, arXiv e-prints, arXiv:1510.07674. <https://arxiv.org/abs/1510.07674>
- Manjavacas, E., Goldman, B., Reffert, S., & Henning, T. 2013, *A&A*, 560, A52, doi: [10.1051/0004-6361/201321720](https://doi.org/10.1051/0004-6361/201321720)
- Marley, M. S., Saumon, D., Cushing, M., et al. 2012, *ApJ*, 754, 135, doi: [10.1088/0004-637X/754/2/135](https://doi.org/10.1088/0004-637X/754/2/135)
- Marocco, F., Smart, R. L., Jones, H. R. A., et al. 2010, *aap*, 524, A38, doi: [10.1051/0004-6361/201015394](https://doi.org/10.1051/0004-6361/201015394)
- Marocco, F., Andrei, A. H., Smart, R. L., et al. 2013, *aj*, 146, 161, doi: [10.1088/0004-6256/146/6/161](https://doi.org/10.1088/0004-6256/146/6/161)
- Marocco, F., Jones, H. R. A., Day-Jones, A. C., et al. 2015, *mnras*, 449, 3651, doi: [10.1093/mnras/stv530](https://doi.org/10.1093/mnras/stv530)
- Marocco, F., Eisenhardt, P. R. M., Fowler, J. W., et al. 2021, *ApJS*, 253, 8, doi: [10.3847/1538-4365/abd805](https://doi.org/10.3847/1538-4365/abd805)
- Martin, E. C., Kirkpatrick, J. D., Beichman, C. A., et al. 2018, *ApJ*, 867, 109, doi: [10.3847/1538-4357/aae1af](https://doi.org/10.3847/1538-4357/aae1af)
- Martín, E. L., Basri, G., Zapatero-Osorio, M. R., Rebolo, R., & López, R. J. G. 1998, *apjl*, 507, L41, doi: [10.1086/311675](https://doi.org/10.1086/311675)
- Martín, E. L., Delfosse, X., Basri, G., et al. 1999, *aj*, 118, 2466, doi: [10.1086/301107](https://doi.org/10.1086/301107)
- Martín, E. L., Rebolo, R., & Magazzù, A. 1994, *apj*, 436, 262, doi: [10.1086/174900](https://doi.org/10.1086/174900)
- Martín, E. L., Phan-Bao, N., Bessell, M., et al. 2010, *aap*, 517, A53, doi: [10.1051/0004-6361/201014202](https://doi.org/10.1051/0004-6361/201014202)
- McElwain, M. W., & Burgasser, A. J. 2006, *aj*, 132, 2074, doi: [10.1086/508199](https://doi.org/10.1086/508199)
- McMahon, R. G., Banerji, M., Gonzalez, E., et al. 2013, *The Messenger*, 154, 35
- . 2021, *VizieR Online Data Catalog*, II/367

- Metchev, S. A., & Hillenbrand, L. A. 2006, *apj*, 651, 1166, doi: [10.1086/507836](https://doi.org/10.1086/507836)
- Metchev, S. A., Kirkpatrick, J. D., Berrian, G. B., &Looper, D. 2008, *apj*, 676, 1281, doi: [10.1086/524721](https://doi.org/10.1086/524721)
- Metchev, S. A., Heinze, A., Apai, D., et al. 2015, *apj*, 799, 154, doi: [10.1088/0004-637X/799/2/154](https://doi.org/10.1088/0004-637X/799/2/154)
- Metodieva, Y., Antonova, A., Golev, V., et al. 2015, *mnras*, 446, 3878, doi: [10.1093/mnras/stu2370](https://doi.org/10.1093/mnras/stu2370)
- Miles-Páez, P. A., Metchev, S., Luhman, K. L., Marengo, M., & Hulsebus, A. 2017, *aj*, 154, 262, doi: [10.3847/1538-3881/aa9711](https://doi.org/10.3847/1538-3881/aa9711)
- Mugrauer, M., Seifahrt, A., Neuh”auser, R., & Mazeh, T. 2006, *mnras*, 373, L31, doi: [10.1111/j.1745-3933.2006.00237.x](https://doi.org/10.1111/j.1745-3933.2006.00237.x)
- Muvzić, K., Radigan, J., Jayawardhana, R., et al. 2012, *aj*, 144, 180, doi: [10.1088/0004-6256/144/6/180](https://doi.org/10.1088/0004-6256/144/6/180)
- Noll, K. S., Geballe, T. R., & Marley, M. S. 1997, *ApJL*, 489, L87, doi: [10.1086/310954](https://doi.org/10.1086/310954)
- Patten, B. M., Stauffer, J. R., Burrows, A., et al. 2006, *apj*, 651, 502, doi: [10.1086/507264](https://doi.org/10.1086/507264)
- Peña Ramírez, K., Zapatero Osorio, M. R., & Béjar, V. J. S. 2015, *A&A*, 574, A118, doi: [10.1051/0004-6361/201424816](https://doi.org/10.1051/0004-6361/201424816)
- Phan-Bao, N., Guibert, J., Crifo, F., et al. 2001, *aap*, 380, 590, doi: [10.1051/0004-6361:20011461](https://doi.org/10.1051/0004-6361:20011461)
- Phan-Bao, N., Bessell, M. S., Martín, E. L., et al. 2006, *mnras*, 366, L40, doi: [10.1111/j.1745-3933.2005.00128.x](https://doi.org/10.1111/j.1745-3933.2005.00128.x)
- . 2008, *mnras*, 383, 831, doi: [10.1111/j.1365-2966.2007.12564.x](https://doi.org/10.1111/j.1365-2966.2007.12564.x)
- Phillips, M. W., Tremblin, P., Baraffe, I., et al. 2020, *A&A*, 637, A38, doi: [10.1051/0004-6361/201937381](https://doi.org/10.1051/0004-6361/201937381)
- Pineda, J. S., Hallinan, G., Kirkpatrick, J. D., et al. 2016, *apj*, 826, 73, doi: [10.3847/0004-637X/826/1/73](https://doi.org/10.3847/0004-637X/826/1/73)
- Pinfield, D. J., Birmingham, B., Lodieu, N., et al. 2012, *mnras*, 422, 1922, doi: [10.1111/j.1365-2966.2012.20549.x](https://doi.org/10.1111/j.1365-2966.2012.20549.x)
- Probst, R. G., & Liebert, J. 1983, *apj*, 274, 245, doi: [10.1086/161442](https://doi.org/10.1086/161442)
- Puget, P., Stadler, E., Doyon, R., et al. 2004, in Society of Photo-Optical Instrumentation Engineers (SPIE) Conference Series, Vol. 5492, Ground-based Instrumentation for Astronomy, ed. A. F. M. Moorwood & M. Iye, 978–987, doi: [10.1117/12.551097](https://doi.org/10.1117/12.551097)
- Radigan, J., Lafreni’re, D., Jayawardhana, R., & Doyon, R. 2008, *apj*, 689, 471, doi: [10.1086/592379](https://doi.org/10.1086/592379)
- Rayner, J. T., Toomey, D. W., Onaka, P. M., et al. 2003, *PASP*, 115, 362, doi: [10.1086/367745](https://doi.org/10.1086/367745)
- Reback, J., jbrockmendel, McKinney, W., et al. 2022, *pandas-dev/pandas*: Pandas 1.4.4, v1.4.4, Zenodo, doi: [10.5281/zenodo.7037953](https://doi.org/10.5281/zenodo.7037953)
- Rebolo, R., Zapatero Osorio, M. R., Madruga, S., et al. 1998, *Science*, 282, 1309, doi: [10.1126/science.282.5392.1309](https://doi.org/10.1126/science.282.5392.1309)
- Reid, I. N., Cruz, K. L., Kirkpatrick, J. D., et al. 2008, *aj*, 136, 1290, doi: [10.1088/0004-6256/136/3/1290](https://doi.org/10.1088/0004-6256/136/3/1290)
- Reid, I. N., & Gilmore, G. 1981, *mnras*, 196, 15P, doi: [10.1093/mnras/196.1.15P](https://doi.org/10.1093/mnras/196.1.15P)
- Reid, I. N., & Gizis, J. E. 2005, *pasp*, 117, 676, doi: [10.1086/430462](https://doi.org/10.1086/430462)
- Reid, I. N., Hawley, S. L., & Gizis, J. E. 1995, *aj*, 110, 1838, doi: [10.1086/117655](https://doi.org/10.1086/117655)
- Reid, I. N., Kirkpatrick, J. D., Gizis, J. E., et al. 2000, *aj*, 119, 369, doi: [10.1086/301177](https://doi.org/10.1086/301177)
- Reid, I. N., Lewitus, E., Allen, P. R., Cruz, K. L., & Burgasser, A. J. 2006a, *aj*, 132, 891, doi: [10.1086/505626](https://doi.org/10.1086/505626)
- Reid, I. N., Lewitus, E., Burgasser, A. J., & Cruz, K. L. 2006b, *apj*, 639, 1114, doi: [10.1086/499484](https://doi.org/10.1086/499484)
- Reid, I. N., & Walkowicz, L. M. 2006, *pasp*, 118, 671, doi: [10.1086/503446](https://doi.org/10.1086/503446)
- Reid, I. N., Cruz, K. L., Allen, P., et al. 2004, *aj*, 128, 463, doi: [10.1086/421374](https://doi.org/10.1086/421374)
- Reylé, C. 2018, *aap*, 619, L8, doi: [10.1051/0004-6361/201834082](https://doi.org/10.1051/0004-6361/201834082)
- Reylé, C., & Robin, A. C. 2004, *aap*, 421, 643, doi: [10.1051/0004-6361:20034553](https://doi.org/10.1051/0004-6361:20034553)
- Reylé, C., Scholz, R. D., Schultheis, M., Robin, A. C., & Irwin, M. 2006, *mnras*, 373, 705, doi: [10.1111/j.1365-2966.2006.11051.x](https://doi.org/10.1111/j.1365-2966.2006.11051.x)
- Rice, E. L., Faherty, J. K., & Cruz, K. L. 2010, *apjl*, 715, L165, doi: [10.1088/2041-8205/715/2/L165](https://doi.org/10.1088/2041-8205/715/2/L165)
- Robert, J., Gagné, J., Artigau, É., et al. 2016, *apj*, 830, 144, doi: [10.3847/0004-637X/830/2/144](https://doi.org/10.3847/0004-637X/830/2/144)
- Robin, A. C., Reylé, C., Derrière, S., & Picaud, S. 2003, *A&A*, 409, 523, doi: [10.1051/0004-6361:20031117](https://doi.org/10.1051/0004-6361:20031117)
- Rodriguez, D. R., Zuckerman, B., Kastner, J. H., et al. 2013, *apj*, 774, 101, doi: [10.1088/0004-637X/774/2/101](https://doi.org/10.1088/0004-637X/774/2/101)
- Ruiz, M. T., Takamiya, M. Y., & Roth, M. 1991, *apjl*, 367, L59, doi: [10.1086/185931](https://doi.org/10.1086/185931)
- Salama, M., Ou, J., Baranec, C., et al. 2021, *AJ*, 162, 102, doi: [10.3847/1538-3881/ac0445](https://doi.org/10.3847/1538-3881/ac0445)
- Salim, S., Lépine, S., Rich, R. M., & Shara, M. M. 2003, *apjl*, 586, L149, doi: [10.1086/374794](https://doi.org/10.1086/374794)
- Saumon, D., Geballe, T. R., Leggett, S. K., et al. 2000, *ApJ*, 541, 374, doi: [10.1086/309410](https://doi.org/10.1086/309410)
- Saumon, D., Hubbard, W. B., Burrows, A., et al. 1996, *ApJ*, 460, 993, doi: [10.1086/177027](https://doi.org/10.1086/177027)
- Saumon, D., & Marley, M. S. 2008, *ApJ*, 689, 1327, doi: [10.1086/592734](https://doi.org/10.1086/592734)
- Schilbach, E., R’oser, S., & Scholz, R. D. 2009, *aap*, 493, L27, doi: [10.1051/0004-6361:200811281](https://doi.org/10.1051/0004-6361:200811281)
- Schmidt, S. J., Hawley, S. L., West, A. A., et al. 2015, *aj*, 149, 158, doi: [10.1088/0004-6256/149/5/158](https://doi.org/10.1088/0004-6256/149/5/158)
- Schmidt, S. J., West, A. A., Hawley, S. L., & Pineda, J. S. 2010, *aj*, 139, 1808, doi: [10.1088/0004-6256/139/5/1808](https://doi.org/10.1088/0004-6256/139/5/1808)
- Schneider, A. C., Cushing, M. C., Kirkpatrick, J. D., et al. 2014, *aj*, 147, 34, doi: [10.1088/0004-6256/147/2/34](https://doi.org/10.1088/0004-6256/147/2/34)

- Schneider, A. C., Greco, J., Cushing, M. C., et al. 2016a, *apj*, 817, 112, doi: [10.3847/0004-637X/817/2/112](https://doi.org/10.3847/0004-637X/817/2/112)
- Schneider, A. C., Munn, J. A., Vrba, F. J., et al. 2023, *AJ*, 166, 103, doi: [10.3847/1538-3881/ace9bf](https://doi.org/10.3847/1538-3881/ace9bf)
- Schneider, A. C., Windsor, J., Cushing, M. C., Kirkpatrick, J. D., & Shkolnik, E. L. 2017, *aj*, 153, 196, doi: [10.3847/1538-3881/aa6624](https://doi.org/10.3847/1538-3881/aa6624)
- Schneider, A. C., Windsor, J., Cushing, M. C., Kirkpatrick, J. D., & Wright, E. L. 2016b, *apjl*, 822, L1, doi: [10.3847/2041-8205/822/1/L1](https://doi.org/10.3847/2041-8205/822/1/L1)
- Schneider, D. P., Greenstein, J. L., Schmidt, M., & Gunn, J. E. 1991, *aj*, 102, 1180, doi: [10.1086/115945](https://doi.org/10.1086/115945)
- Schneider, D. P., Knapp, G. R., Hawley, S. L., et al. 2002, *aj*, 123, 458, doi: [10.1086/338095](https://doi.org/10.1086/338095)
- Scholz, R. D. 2010, *aap*, 515, A92, doi: [10.1051/0004-6361/201014264](https://doi.org/10.1051/0004-6361/201014264)
- Scholz, R. D., Bihain, G., Schnurr, O., & Storm, J. 2011, *aap*, 532, L5, doi: [10.1051/0004-6361/201117297](https://doi.org/10.1051/0004-6361/201117297)
- Scholz, R. D., Irwin, M., Ibata, R., Jahreiss, H., & Malkov, O. Y. 2000, *aap*, 353, 958
- Scholz, R. D., Lehmann, I., Matute, I., & Zinnecker, H. 2004, *aap*, 425, 519, doi: [10.1051/0004-6361:20041059](https://doi.org/10.1051/0004-6361:20041059)
- Scholz, R. D., McCaughrean, M. J., Zinnecker, H., & Lodieu, N. 2005, *aap*, 430, L49, doi: [10.1051/0004-6361:200400121](https://doi.org/10.1051/0004-6361:200400121)
- Scholz, R. D., & Meusinger, H. 2002, *mnras*, 336, L49, doi: [10.1046/j.1365-8711.2002.05998.x](https://doi.org/10.1046/j.1365-8711.2002.05998.x)
- Scholz, R. D., Meusinger, H., & Jahreiss, H. 2001, *aap*, 374, L12, doi: [10.1051/0004-6361:20010811](https://doi.org/10.1051/0004-6361:20010811)
- Scholz, R. D., Storm, J., Knapp, G. R., & Zinnecker, H. 2009, *aap*, 494, 949, doi: [10.1051/0004-6361:200811053](https://doi.org/10.1051/0004-6361:200811053)
- Seifahrt, A., Mugrauer, M., Wiese, M., Neuh”auser, R., & Guenther, E. W. 2005, *Astronomische Nachrichten*, 326, 974, doi: [10.1002/asna.200510456](https://doi.org/10.1002/asna.200510456)
- Sheppard, S. S., & Cushing, M. C. 2009, *aj*, 137, 304, doi: [10.1088/0004-6256/137/1/304](https://doi.org/10.1088/0004-6256/137/1/304)
- Shkolnik, E. L., Allers, K. N., Kraus, A. L., Liu, M. C., & Flagg, L. 2017, *aj*, 154, 69, doi: [10.3847/1538-3881/aa77fa](https://doi.org/10.3847/1538-3881/aa77fa)
- Shkolnik, E. L., Liu, M. C., Reid, I. N., Dupuy, T., & Weinberger, A. J. 2011, *apj*, 727, 6, doi: [10.1088/0004-637X/727/1/6](https://doi.org/10.1088/0004-637X/727/1/6)
- Siegler, N., Close, L. M., Burgasser, A. J., et al. 2007, *aj*, 133, 2320, doi: [10.1086/513273](https://doi.org/10.1086/513273)
- Skrutskie, M. F., Cutri, R. M., Stiening, R., et al. 2006, *AJ*, 131, 1163, doi: [10.1086/498708](https://doi.org/10.1086/498708)
- Skrzypek, N., Warren, S. J., & Faherty, J. K. 2016, *aap*, 589, A49, doi: [10.1051/0004-6361/201527359](https://doi.org/10.1051/0004-6361/201527359)
- Smart, R. L., Tinney, C. G., Bucciarelli, B., et al. 2013, *mnras*, 433, 2054, doi: [10.1093/mnras/stt876](https://doi.org/10.1093/mnras/stt876)
- Smart, R. L., Bucciarelli, B., Jones, H. R. A., et al. 2018, *mnras*, 481, 3548, doi: [10.1093/mnras/sty2520](https://doi.org/10.1093/mnras/sty2520)
- Smith, L., Lucas, P. W., Bunce, R., et al. 2014, *mnras*, 443, 2327, doi: [10.1093/mnras/stu1295](https://doi.org/10.1093/mnras/stu1295)
- Spiegel, D. S., Burrows, A., & Milsom, J. A. 2011, *ApJ*, 727, 57, doi: [10.1088/0004-637X/727/1/57](https://doi.org/10.1088/0004-637X/727/1/57)
- Stephens, D. C., Leggett, S. K., Cushing, M. C., et al. 2009, *ApJ*, 702, 154, doi: [10.1088/0004-637X/702/1/154](https://doi.org/10.1088/0004-637X/702/1/154)
- Strauss, M. A., Fan, X., Gunn, J. E., et al. 1999, *apjl*, 522, L61, doi: [10.1086/312218](https://doi.org/10.1086/312218)
- Tamburo, P., Muirhead, P. S., McCarthy, A. M., et al. 2022, *AJ*, 164, 252, doi: [10.3847/1538-3881/ac9a52](https://doi.org/10.3847/1538-3881/ac9a52)
- Teegarden, B. J., Pravdo, S. H., Hicks, M., et al. 2003, *apjl*, 589, L51, doi: [10.1086/375803](https://doi.org/10.1086/375803)
- Tennyson, J., & Yurchenko, S. 2018, *Atoms*, 6, 26, doi: [10.3390/atoms6020026](https://doi.org/10.3390/atoms6020026)
- Thackrah, A., Jones, H., & Hawkins, M. 1997, *mnras*, 284, 507, doi: [10.1093/mnras/284.2.507](https://doi.org/10.1093/mnras/284.2.507)
- The Astropy Collaboration, Price-Whelan, A. M., Lian Lim, P., et al. 2022, *arXiv e-prints*, arXiv:2206.14220. <https://arxiv.org/abs/2206.14220>
- Thompson, M. A., Kirkpatrick, J. D., Mace, G. N., et al. 2013, *pasp*, 125, 809, doi: [10.1086/671426](https://doi.org/10.1086/671426)
- Tinney, C. G. 1993a, *apj*, 414, 279, doi: [10.1086/173075](https://doi.org/10.1086/173075)
- . 1993b, *aj*, 105, 1169, doi: [10.1086/116501](https://doi.org/10.1086/116501)
- . 1996, *mnras*, 281, 644, doi: [10.1093/mnras/281.2.644](https://doi.org/10.1093/mnras/281.2.644)
- Tinney, C. G., Burgasser, A. J., & Kirkpatrick, J. D. 2003, *AJ*, 126, 975, doi: [10.1086/376481](https://doi.org/10.1086/376481)
- Tinney, C. G., Burgasser, A. J., Kirkpatrick, J. D., & McElwain, M. W. 2005, *aj*, 130, 2326, doi: [10.1086/491734](https://doi.org/10.1086/491734)
- Tinney, C. G., Delfosse, X., Forveille, T., & Allard, F. 1998, *aap*, 338, 1066. <https://arxiv.org/abs/astro-ph/9805311>
- Tinney, C. G., Faherty, J. K., Kirkpatrick, J. D., et al. 2014, *ApJ*, 796, 39, doi: [10.1088/0004-637X/796/1/39](https://doi.org/10.1088/0004-637X/796/1/39)
- Tinney, C. G., Mould, J. R., & Reid, I. N. 1993, *aj*, 105, 1045, doi: [10.1086/116492](https://doi.org/10.1086/116492)
- Tinney, C. G., Kirkpatrick, J. D., Faherty, J. K., et al. 2018, *apjs*, 236, 28, doi: [10.3847/1538-4365/aabad3](https://doi.org/10.3847/1538-4365/aabad3)
- Tsai, S.-M., Kitzmann, D., Lyons, J. R., et al. 2018, *ApJ*, 862, 31, doi: [10.3847/1538-4357/aac834](https://doi.org/10.3847/1538-4357/aac834)
- Tsvetanov, Z. I., Goliowski, D. A., Zheng, W., et al. 2000, *apjl*, 531, L61, doi: [10.1086/312515](https://doi.org/10.1086/312515)
- UKIDSS Consortium. 2012, *VizieR Online Data Catalog*, II/316
- Vacca, W. D., Cushing, M. C., & Rayner, J. T. 2003, *PASP*, 115, 389, doi: [10.1086/346193](https://doi.org/10.1086/346193)
- Valenti, J. A., & Fischer, D. A. 2005, *ApJS*, 159, 141, doi: [10.1086/430500](https://doi.org/10.1086/430500)
- van Biesbroeck, G. 1961, *aj*, 66, 528, doi: [10.1086/108457](https://doi.org/10.1086/108457)
- van Leeuwen, F. 2007, *aap*, 474, 653, doi: [10.1051/0004-6361:20078357](https://doi.org/10.1051/0004-6361:20078357)

- Virtanen, P., Gommers, R., Oliphant, T. E., et al. 2020, *Nature Methods*, 17, 261, doi: <https://doi.org/10.1038/s41592-019-0686-2>
- Vrba, F. J., Henden, A. A., Luginbuhl, C. B., et al. 2004, *AJ*, 127, 2948, doi: <10.1086/383554>
- Weinberger, A. J., Boss, A. P., Keiser, S. A., et al. 2016, *aj*, 152, 24, doi: <10.3847/0004-6256/152/1/24>
- West, A. A., Hawley, S. L., Bochanski, J. J., et al. 2008, *aj*, 135, 785, doi: <10.1088/0004-6256/135/3/785>
- Wilson, J. C., Kirkpatrick, J. D., Gizis, J. E., et al. 2001, *aj*, 122, 1989, doi: <10.1086/323134>
- Wilson, J. C., Miller, N. A., Gizis, J. E., et al. 2003, in *Brown Dwarfs*, ed. E. Martín, Vol. 211, 197
- Zapatero Osorio, M. R., Rebolo, R., Bihain, G., et al. 2010, *apj*, 715, 1408, doi: <10.1088/0004-637X/715/2/1408>
- Zhang, Z., Liu, M. C., Best, W. M. J., Dupuy, T. J., & Siverd, R. J. 2021a, *apj*, 911, 7, doi: <10.3847/1538-4357/abe3fa>
- Zhang, Z., Liu, M. C., Marley, M. S., Line, M. R., & Best, W. M. J. 2021b, *ApJ*, 921, 95, doi: <10.3847/1538-4357/ac0af7>
- . 2021c, *apj*, 916, 53, doi: <10.3847/1538-4357/abf8b2>
- Zhang, Z., Liu, M. C., Morley, C. V., et al. 2022, *ApJ*, 935, 15, doi: <10.3847/1538-4357/ac7ce9>
- Zhang, Z., Liu, M. C., Best, W. M. J., et al. 2018, *apj*, 858, 41, doi: <10.3847/1538-4357/aab269>
- Zhang, Z., Liu, M. C., Hermes, J. J., et al. 2020, *ApJ*, 891, 171, doi: <10.3847/1538-4357/ab765c>
- Zhang, Z. H., Pokorný, R. S., Jones, H. R. A., et al. 2009, *aap*, 497, 619, doi: <10.1051/0004-6361/200810314>
- Zuckerman, B., & Song, I. 2004, *ARA&A*, 42, 685, doi: <10.1146/annurev.astro.42.053102.134111>